THE DEFORMATION AND PROPERTIES OF COHESIVE SOIL IN RELATION TO SOIL-MACHINE SYSTEMS.

BY

JOO ICK KIM

B.Sc., Seoul National University, 1960

M.Sc., Israel Institute of Technology, 1967

A THESIS SUBMITTED IN PARTIAL FULFILMENT OF THE REQUIREMENTS FOR THE DEGREE OF DOCTOR OF PHILOSOPHY

in the Department

of

Mechanical Engineering

We accept this thesis as conforming to the required standard

THE UNIVERSITY OF BRITISH COLUMBIA
September, 1970

In presenting this thesis in partial fulfilment of the requirements for an advanced degree at the University of British Columbia, I agree that the Library shall make it freely available for reference and study. I further agree that permission for extensive copying of this thesis for scholarly purposes may be granted by the Head of my Department or by his representatives. It is understood that copying or publication of this thesis for financial gain shall not be allowed without my written permission.

JOO ICK KIM

Department of Mechanical Engineering,

The University of British Columbia
Vancouver 8, Canada

Date Oct 9, 1970

ABSTRACT

Methods of determining the deformation characteristics, physical properties and dynamic response of cohesive soils were evaluated in order to obtain design parameters for soil-machine systems. The study was limited to simple scaled soil-machine systems on Haney clay and on mixed Haney clay and Ottawa sand in the semi-solid to plastic range.

A special moire method was successfully developed to study large deformation and translation paths of soil as a function of tool shape and position.

Compression, direct shear, stress wave and forced vibration methods were used to measure mechanical properties of soils. Advantages and disadvantages of each method were evaluated.

Quasi-static stress-strain relationships were established from improved unconfined compression tests to produce unixial compression. Yield stress and strain hardening effects could be observed from these tests.

Rate dependency of cohesive soil was verified by observing stress wave propagation in soil. It was observed that stress wave propagation velocity was more sensitive to soil particle size than to soil strength.

Forced vibration methods were used to evaluate elastic constants such as Young's modulus and shear modulus which are useful in determining the contribution of elastic strains to the total force required to deform a soil.

The theory of plasticity was successfully used in conjunction with experimental observations to establish stress-strain relationships in the soil on the assumption that strain hardening was linear and elastic strains were negligible. The maximum difference between theoretical forces deduced on the above basis and measured forces was less than twenty percent.

The use of gelatin as a simulated soil was investigated to determine whether its use could provide a useful qualitative aid to design of soil-machine systems. It was found that the gelatin study gave stress trajectories and slip lines which resembled the results observed by the moire method in actual soil. Results obtained from the application of soil-machine systems on simulated soil and prototype soil were compared.

ACKNOWLEDGEMENTS

I wish to express my sincere thanks and gratitude to my research supervisor Professor L. M. Staley for his constant advice and encouragement. Special appreciation is also expressed to Dr. J. P. Duncan whose continuous consultation and assistance accelerated the research program, as well as several faculty members and technicians of the Mechanical Engineering Department. Thanks are extended to Mr. W. Gleave, Senior Technician in the Department of Agricultural Engineering for assisting in the design and construction of special apparatus used in these studies.

This research was financed by the National Research Council, Grant No. 1915.

THE DEFORMATION AND PROPERTIES OF COHESIVE SOIL IN RELATION TO SOIL-MACHINE SYSTEMS

TABLE OF CONTENTS

LIST OF ILLUSTRATIONS

PAGE

PAGE

PAGE

PAGE

PAGE

LIST OF TABLES

1. INTRODUCTION

Proper design of soil machine systems is economically important in terms of its influence on the cost of crop production, construction and transportation. In North America alone, 500 billion tons of soil are annually subjected to primary tillage on 600 million acres of cropland. Similarly, large quantities of soil are manipulated for construction purposes and many types of traction devices are utilized to accomplish these jobs. It is, therefore, important to provide the most economical soil machines for these operations. This can be achieved by improving existing tools or by designing new machines.

There are three possible approaches to the design and development of a soil machine. Design may be based on trial and error, on theoretical analysis or on similitude studies. The design of a soil machine is still considered more of an art than a science, because of the lack of sufficient basic quantitative knowledge of the reaction of soil to the intrusion of a soil machine. This is due to difficulty in accurately measuring the stress and strain as well as the mechanical properties of soil. For this reason researchers have used similitude techniques with distorted model conditions. This is still mostly a trial and error method as the identification of suitable

physical variables is not possible due to a lack of understanding of the physical behavior and mechanical properties of soil. Many investigators using similitude techniques have found that a model test did not predict the performance of the prototype, particularly in cohesive soils where physical variables are of a complex nature. It is therefore essential to determine stress and strain relationships and other pertinent soil properties necessary for logical design of soil machine systems.

Physical and mechanical properties of soils are so complex and variable that no single general theory can be applied. Researchers have treated soil as an elastic, viscoelastic or plastic material. The theoretical approach used depends on the type of soil, its physical state and the loading conditions. Elasticity theory may be applied for very small strain levels with incremental loading conditions while viscoelastic theory may be used for dynamic or static loading at low strain levels in both cohesive and cohesionless soils. Plasticity theory is suitable for cohesive soils subject to large deformation. Mechanical properties of a soil and the stress-strain relationship depend upon the physical condition of soil while soil response varies according to the conditions of the applied load.

2. CRITIQUE OF CURRENT APPROACHES

In the past many similitude studies of soil machine systems have been conducted. Since Bockhop* (6) used true model theory to predict the performance of a prototype disk from a scaled model, many researchers (3, 6, 47, 48, 56, 57 and 68) have attempted to develop model design techniques for soil machine systems based on both true model and distorted model theory. The accuracy of prediction has been poor although some studies using simple tools in specific soil conditions have been quite satisfactory. Results have been reasonably accurate in cohesionless soils while the prediction accuracy generally decreased with increased clay content.

Inaccurate prediction has been due to insufficient identification of suitable physical variables and lack of basic qualitative and quantitative knowledge of soil-machine interactions. It is still difficult to determine to what degree each factor influences the accuracy of prediction. Individual factors require thorough investigation under separately controlled conditions. Investigations such as the variation in shearing resistance with variation of shearing strain rate are required since the model and prototype must each function in a different speed range. Also

---

* Numbers in parentheses refer to the appended bibliography.

needed is an investigation to ascertain the reliability of empirically determined distortion correction factors. The prediction is not only the function of distorted factors but also of other undistorted "Pi" terms. Particularly in cohesive soils there is doubt as to whether the model will work under the same geometrical condition after loading even though the model and prototype were geometrically similar before loading. If this is true, the stress-strain behavior in the soil is different for the model and the prototype, resulting in disproportionate draft forces leading to inaccurate prediction.

It is also unknown whether different shapes of geometrically similar tools (for example, a different apex angle in a chisel or a different proportion between disk diameter and curvature) change the accuracy of prediction as the basic stress-strain behavior of soil is not understood. Unless basic qualitative and quantitative design parameters are to be studied, the similitude technique is little different from the trial and error design methods used in the past. For these reasons, the dynamic behavior of soil, its stress-strain relationships and its mechanical properties require full investigation.

3. PURPOSE OF THIS RESEARCH

This research is intended as a development of techniques for the model design of soil-machine systems in cohesive soils. It is directed toward this ultimate objective by emphasizing a description of the mechanical properties of soils and the dynamic and static soil responses to controlled soil-machine systems.

The purpose of the study may be summarized as follows:

1) To provide quantitative and qualitative information on the dynamic and static response of soil to the intrusion of controlled soil-machine systems. The soil response is examined from the measurements of deformation and translation within the soil mass, using the moire technique that provides much hitherto unavailable information.

2) To establish accurate stress and strain relationships of soils for the investigation of yield phenomena, strain hardening effects and plastic stress-strain relationships. The stress and strain relationships are studied by using an improved unconfined compression test.

3) To evaluate appropriate moduli as a means of understanding mechanical properties under the different physical conditions. Elasticity constants have to

be evaluated to consider the significance of elastic strains on the total force that is experienced during elastic deformation prior to entering the plastic range.

4) To investigate the rate dependency of soil strength to determine the importance of machine speed when used as a design parameter.

5) To investigate the possibility of using photo-elastic gelatin as a simulated soil to provide some qualitative design parameters for soil-machine systems.

4. REVIEW OF LITERATURE

4.1 Soil Deformation Measurement

The accurate measurement of soil deformation is an important step in the design of soil-machine systems. Although many techniques have been used for soil deformation measurement, most results have been qualitative and not directly applicable to soil-machine design.

Gill (21) studied soil deformation by tracing the movement of embedded pins in a soil mass. Total displacement of each pin was determined by marking its initial location on a transparent sheet of acetate paper which was placed over the surface of the soil and measuring its final location. He attempted to analyze shear strain by measuring the difference between the initial magnitude of the corner angle and final corner angle. Average shear strain was then assumed to be

$$\gamma_{avg} = \tan^{-1} \frac{D_o \, e^{m\,(X_1 - X_2)} \cos \bar{\beta}}{X_2 - X_1 + D_o \, e^{m(X_2 - X_1)} \cos \bar{\beta}}$$

where γ_{avg} = average shear strain

D_o = actual soil displacement at tool surface

m = rate of attenuation of displacement at remote locations

X_1, X_2 = lateral distances to edges of soil element prior to displacement

$\bar{\beta}$ = average angular movement of soil element

The basis of these calculations was the assumption that the pins moved with the soil and that measurement of the pin movement was a reliable measurement of soil movement.

Khamidov (31) and Chancellor and Schmidt (10) used lead shots, detected by X-ray methods, to measure strain in soils. Roscoe et al. (52) and Boyd (7) used a cine flash X-ray technique to measure the translation and velocity of particles within a soil mass. They also assumed that movement of the lead shots was an accurate indicator of soil movement. Their experiments were restricted to dry sand as it is possible to accurately position the lead shots in this soil.

Nichols and Reed (41) used markers to trace the movement of different portions of a soil mass adjacent to a tool. Toms (64) used a method of colouring layers of soil which were photographed after deformation. Other investigators have used soft tissue paper placed between soil layers to observe displacement. Olson and Weber (43) used a high-speed movie camera to study the movements of a soil surface during deformation by a tool. Siemens et al. (55) also used high-speed movie cameras and a square grid method to investigate failure planes resulting from the movement of a vertical blade. Thomas and Anderson (63) applied a method used in foundry moulding practices. Sand grains were coated with a thin layer of sodium silicate and this coated sand was then used to prepare

moulds in the usual way and after deformation the mix was set by passing CO_2 gas through it. It was possible to obtain patterns of deformation by using dyed soil layers of different colours in preparation of the mould. By sectioning the blocks after deformation, three dimensional chemical deformation patterns could be obtained. Due to the setting strength of the soil, the clay fraction should not exceed two percent. Nichols et al. (42) studied the soil movement from a plow by viewing it through the glass side of the model test bin. The glass was covered with levigated aluminum permitting the movement of soil particles to trace paths on the glass surface. This method provided visual shear surfaces and soil flow lines.

Most of the methods described above are useful for qualitative analysis only and are often limited to non-cohesive soils. A quantitative description of soil deformations, particularly in cohesive soils, has not been obtained.

4.2 Soil Stress Measurement

The magnitude of stress in a soil medium has been measured by many investigators by using a sensing device that can detect stress. Many types of stress transducers have been designed for this use. Cooper et al. (13) used strain gauge cells to measure soil pressure. Plantema (45)

developed a soil pressure cell with suitable calibration equipment. Numerous transducers of similar types have been described by Redshaw (49) and Durelli and Riley (17). Most transducers are insensitive to shear stress, responding only to the normal component of the stress vector. The sensing surface of a transducer represents a plane and a stress vector acts on this plane.

The main problem in designing stress transducers has been to overcome arching phenomena. As noted by Gill and Vanden Berg (22), if a transducer is more rigid than the surrounding soil, a higher value will be observed than if the transducer has the same rigidity as the soil. Settlement of soil immediately adjacent to the transducer results in an arching action that transfers some of the applied load to the transducer. Conversely, if the transducer is less rigid than the soil, a lower value will be obtained since the load will be transferred from the transducer to the surrounding soil. Thus, the size, shape and resiliency that the transducer presents to the soil mass affects the response of the transducer. Another problem in using stress transducers is to determine their orientation, particularly if soil deformation is large.

A soil stress gauge, recently developed by Selig and Wetzel (54) for laboratory measurements, uses a piezoelectric ceramic disk (lead titanate zirconate)

positioned within an aluminum case. The gauge is capable of both static and dynamic response in the range of micro-seconds to minutes. It is, however, reported by Hampton (24) that the sensitivity of the gauge is approximately ± 20 percent of the nominal value.

4.3 Dynamic Behavior and Mechanical Properties of Soils

4.3.1. Dynamic response of soil

The velocity of stress wave propagation in a soil may be used to determine its dynamic mechanical properties. Nacci and Taylor (40) and other investigators showed a general agreement among shear strength, porosity, confining pressure and stress wave propagation. Soils are however different from elastic solids and stress wave propagation may be a function of many more factors such as moisture content, applied stress intensity and strain level. Many other researchers have used stress wave propagation as a means of evaluating soil parameters and understanding the response of soil under dynamic loading conditions.

Gupta and Pandya (23) used stress wave propagation velocity to compute compressive and shear stresses induced in soil by tillage implements. They claim that it provides accurate stress values.

Hampton and Wetzel (24) attempted to derive a suitable theory for predicting wave propagation

phenomena in soils but had little success. Vey and Strauss (65), observing stress wave propagation under different confining pressures, concluded that velocity increased with an increase in the confining pressure. Attempts were made by Baker and Triandafilidis (2), Constantino et al. (12) and Wilson and Dietrich (66) to evaluate the elastic modulus from the equation $C = \sqrt{E/\rho}$, assuming that soil is an elastic medium. Comparison between moduli measured by stress and strain relationships and those computed from the stress wave propagation, showed that values obtained from stress wave techniques were generally an order of magnitude greater. In most of these studies it is difficult to determine whether the modulus measured from stress and strain relationships was the elastic or plastic tangential modulus since yield stress in the soil was usually not defined or evaluated. Results of stress wave propagation studies in soils indicates that particularly in cohesive soils many seemingly divergent findings can be made. Kondner (33) summarized this as follows:

> "Often for similar soils, or even the same soil, propagation velocities obtained in different studies may agree in some cases and may differ widely in others; they may be affected both strongly and negligibly by variations in the time characteristics of the applied excitation; strain level may

> have little effect on propagation velocity in some situations and large effects in others; in some cases velocity increases with strain rate while other test results indicate a decrease...."

Vey and Strauss (65) investigated the dynamic behavior of soils by simultaneously observing strain and stress waves at a number of positions on relatively long specimens. Although their experimental apparatus proved to be very useful for investigation of stress wave propagations in long specimens, the first stress and strain gauges were inserted so near the load end of the specimens that the quantitative values of stress and strain measured near the load end are questionable.

Durelli and Riley (17) found that for accurate response and simulation of infinitely long specimens the first gauge should be inserted at a distance of at least four times the specimen diameter from the impact end. Vey and Strauss inserted nine gauges in the specimen. Since gauge diameter was greater than one-third of the specimen diameter problems of continuity and homogeniety of the specimen may have occurred.

Many theoretical works have also been conducted in an attempt to solve the problem of stress waves in a soil medium. Shipley et al. (59) used numerical analysis and a finite element technique to simulate stress wave propagation in soil. A comparison was made between

finite element predictions and exact solutions to investigate the accuracy in analyzing wave propagation problems. Comparisons showed that for cases involving only a single wave, the finite element results were in excellent agreement with exact solutions. Even for the case of two plane waves, results compared well with theoretical calculations. Since no comparisons with experimental results from the actual soil tests were made, the usefulness of this approach is questionable.

Ishihara (29) investigated the propagation of compressional waves in a saturated soil. He established separate equations of motion for the solid and fluid phases of soil by assuming that a soil is represented by a water saturated porous elastic matrix. As a result of these analyses, he derived a revised form of the two compressional waves that were originally found by Biot (5). By examining the deformation modulus appearing in the frequency equation, with reference to specific test conditions, he postulated that the first compressive wave travels through the solid-water system without changing any pore volume, but that the second compressive wave progresses only when a volume change of the pore space takes place. This theory may be applicable for small impact loading conditions with

elastic strain for the first type wave and for large deformation with static loading conditions for a second type wave. For both cases the soil has to be saturated.

Further theoretical work has been conducted by many others such as Batdorf (4) on air induced ground shock and Ang and Chang (1) on the numerical calculation of the interaction between soil and inelastic plane structures.

4.3.2. Determination of moduli

The dynamic modulus of elasticity may be evaluated from the mechanical resonance frequency of soil specimens subject to forced vibration. This method has been extensively used in metallurgy, rock mechanics and concrete technology, but infrequent and limited application has been found in soils. Ishimoto and Irda (30) and Wilson and Dietrich (66) described tests to determine the modulus for cohesive soil specimens. The soil specimen was placed in a vertical position and longitudinal and torsional vibrations were produced by the moving diaphragm of a horn driver which was directly connected by a rod to a clamped rim on the diaphragm. The resonant frequencies were then used to compute appropriate moduli, such as the modulus of elasticity, the modulus of rigidity and Poisson's ratio.

Although Wilson and Dietrich improved the

existing experimental apparatus, they never considered the effect of size and shape of the test specimens. They also introduced inertia forces of the specimen and cap by mounting the specimen vertically on the vibrating plate, which could have affected the resonance frequency.

Extensive and detailed test procedures for general application of measuring elastic moduli from the mechanical resonance frequencies have been prepared by Spinner and Tefft (60). They discuss different techniques for exciting, detecting and measuring the mechanical resonance frequencies of the specimen. In addition, equations are given for computing the appropriate elastic moduli from these resonance frequencies.

5. NEW APPROACH TO SOIL-MACHINE SYSTEM DESIGN

The analysis and design procedure used in this study is a new approach to soil-machine design. The steps used in this procedure are outlined in Figure 1.

The study is carried out initially from three stages. In the first stage the qualitative soil behaviors were recognized to understand basic physical and mechanical properties prior to quantitative analysis. In the second stage quanitative physical and mechanical properties of soil are measured and analyzed to provide basic quanitative knowledge of soil reactions and identification of measurable physical variables. From the observed results soil behavior and stress-strain equations were established. The third stage is a practical application of these established relations and other pertinent criteria to the design of soil-machines. Application of the design procedure is limited to cohesive soils in the semi-solid to plastic range. This range has seldom been investigated due to the difficulty of manipulation and analysis techniques. Two types of soil-machines were applied as a practical application of plasticity theory and a photoelastic gelatin technique was used for comparison and qualitative analysis.

Figure 1. NEW APPROACH TO THE DESIGN OF SOIL-MACHINE SYSTEMS

I QUALITATIVE PHASE

ANALYSIS

RECOGNITION OF SOIL BEHAVIOR

METHOD USED

1) MOIRE METHOD
2) STRESS WAVE TECHNIQUE
3) PHOTOELASTIC GELATIN AS SIMULATED SOIL

II QUANTITATIVE PHASE

ANALYSIS

DEFORMATION MEASUREMENT

METHOD USED

MOIRE METHOD

ANALYSIS

DETERMINATION OF ELASTIC MODULI FOR ELASTIC STRAINS

METHOD USED

1) FORCED VIBRATION
2) STRESS WAVE TECHNIQUE

ANALYSIS

DETERMINATION OF YIELD STRESS AND STRAIN HARDENING EFFECT FOR PLASTIC STRAINS

METHOD USED

1) UNIAXIAL COMPRESSION TEST
2) MAXIMUM SHEAR STRESS THEORY
3) APPROXIMATION METHOD

ANALYSIS

STRESS-STRAIN RELATIONSHIPS

METHOD USED

1) IMPROVED UNCONFINED COMPRESSION TEST

ANALYSIS

ESTABLISHMENT OF STRESS-STRAIN EQUATIONS AND SOIL BEHAVIOR

METHOD USED

RESULTS OBTAINED FROM THE QUALITATIVE AND QUANTITATIVE PHASES

III APPLIED PHASE

ANALYSIS

DEVELOPMENT OF A MECHANICS

METHOD USED

OVERALL TEST RESULTS APPLIED TO PLASTICITY THEORY

6. NEW METHOD OF SOIL DEFORMATION MEASUREMENT

Deformation in soils may be measured from the corresponding moire effect. If two screens of slightly crossed equidistant lines are superimposed, interference patterns, called moire fringes, appear where the lines on the first screen (surface grid) intersect those of the second (master grid). The moire effect has been applied by engineers in the study of deformation of metals and plastics.

If one draws regularly spaced lines of equal width on an undeformed soil test specimen and also on a transparent screen and deforms the test specimen, moire fringes are formed when the transparent master grid is superimposed upon the deformed grid. These fringes provide the basis from which the amount of deformation may be calculated.

This technique has the advantage over some other methods in that regions of particular interest are clearly shown. The fringe measurements yield all the components of displacement of a two dimensional strain field, and photographic records of the fringes can be taken at any stage of soil deformation.

6.1 Moire Technique

In the actual experiment one array is placed on the

surface of the test specimen (called the surface grid) and a reference array (called the master grid) usually of the same pitch, is placed adjacent to, and aligned parallel with, the surface grid. As the test specimen is loaded, the surface grid will deform and follow the surface displacements induced in the specimen. The master grid, of course, does not change as the specimen is loaded and consequently a moire - interference pattern forms.

Moire fringe patterns can most easily be interpreted by relating them to the displacement field since the moire fringes give the displacement field in a simple and direct fashion. Once the surface u and v displacements have been established by using arrays parallel to the x and y axes of a model, the cartesian strain components can be computed from the derivatives of the displacements.

For the use of finite strain, the normal strain ε_x and ε_y are defined as the change in length of a line segment parallel to the x axis and y axis respectively divided by its original length (Lagrangian strain).

$$\varepsilon_x = \left[1 + 2\frac{\partial u}{\partial x} + \left(\frac{\partial u}{\partial x}\right)^2 + \left(\frac{\partial v}{\partial x}\right)^2\right]^{1/2} - 1 \qquad [1]$$

$$\varepsilon_y = \left[1 + 2\frac{\partial v}{\partial y} + \left(\frac{\partial v}{\partial y}\right)^2 + \left(\frac{\partial u}{\partial y}\right)^2\right]^{1/2} - 1 \qquad [2]$$

$$\gamma_{xy} = \sin^{-1} \frac{\frac{\partial u}{\partial y} + \frac{\partial v}{\partial x} + \frac{\partial u}{\partial x}\cdot\frac{\partial u}{\partial y} + \frac{\partial v}{\partial x}\cdot\frac{\partial v}{\partial y}}{(1 + \varepsilon_x)(1 + \varepsilon_y)} \qquad [3]$$

In those instances where products and powers of derivatives are sufficiently small that they can be neglected, the above equations reduce to those commonly employed in the classical linear theory of elasticity.

$$\varepsilon_x = \frac{\partial u}{\partial x} \qquad [4]$$

$$\varepsilon_y = \frac{\partial v}{\partial y} \qquad [5]$$

$$\gamma_{xy} = \frac{\partial u}{\partial y} + \frac{\partial v}{\partial x} \qquad [6]$$

After determining the three strain components ε_x, ε_y, and γ_{xy} for homogeneous plane strain, the principal strains ε_1 and ε_2 and their direction θ are then given by:

$$\varepsilon_1, \varepsilon_2 = 1/2 \quad (\varepsilon_x + \varepsilon_y) \pm \sqrt{(\varepsilon_x - \varepsilon_y)^2 + \gamma_{xy}^2} \qquad [7]$$

$$\tan 2\theta = \frac{\gamma_{xy}}{\varepsilon_x - \varepsilon_y} \qquad [8]$$

If the strain is not homogeneous, as may be the case in soils, these formulae give the average values of the strain component in a small area limited by the interference fringes.

6.2 Assumptions for Strain Analysis

The following assumptions must be made before strains in the soil mass may be calculated:

(1) The element of soil between the interference fringes strains uniformly.

(2) Friction between the master and surface grids

has a negligible effect on the calculated results.

(3) Soil conditions of each test sample batch are reproducible.

6.3 Fringe-Pattern Interpretation

The moire fringe phenomenon can be explained in terms of the resulting fringe patterns shown in Figure 2. The fringes were formed by overlapping the surface grid with the master grid with all lines parallel. Equal width of opaque line and transparent space is not essential, but it gives the best resolution. Figure 2 shows the resulting pattern for tension. In general, the distance between the centers of adjacent lines of maximum density (fringe lines) will be given by

$$D = \frac{P}{\varepsilon}(1 + \varepsilon) \qquad [9]$$

where D = fringe spacing

P = unstrained grid pitch

ε = strain perpendicular to the grid lines, + for tension and - for compression.

Normal strain in a direction perpendicular to the grid lines therefore can be determined if P is known and D is measured; thus

$$\varepsilon_t = \frac{P}{D - P} \qquad [10]$$

for tensile strains and

$$\varepsilon_c = \frac{P}{D + P} \qquad [11]$$

for compressive strains.

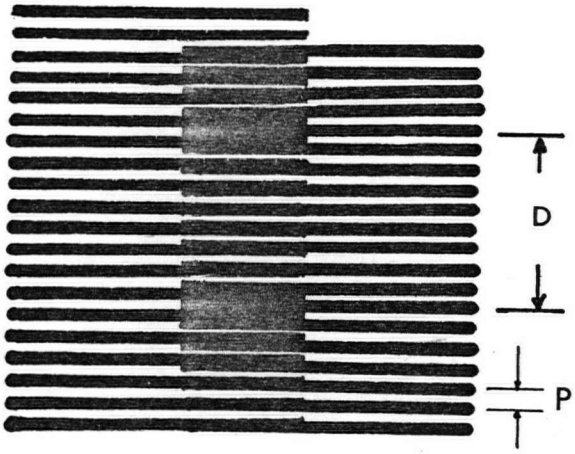

Figure 2. Moire fringe effect, tensile strain.

The moire fringe patterns resulting from relative rotation of two grids with an angle θ are are shown in Figure 3 Consideration of three triangles A, B and C determines the rotated angle θ.

Since triangles B and C are equal triangles,

$q = P.$

Then from triangle A:

$$a = \frac{q}{\tan\theta} = \frac{P}{\tan\theta} \text{ and } b = P \tan\frac{\theta}{2} \qquad [12]$$

The distance between the fringes, measured parallel to the master grid lines is given by

$$H_m = a + b \qquad [13]$$

and

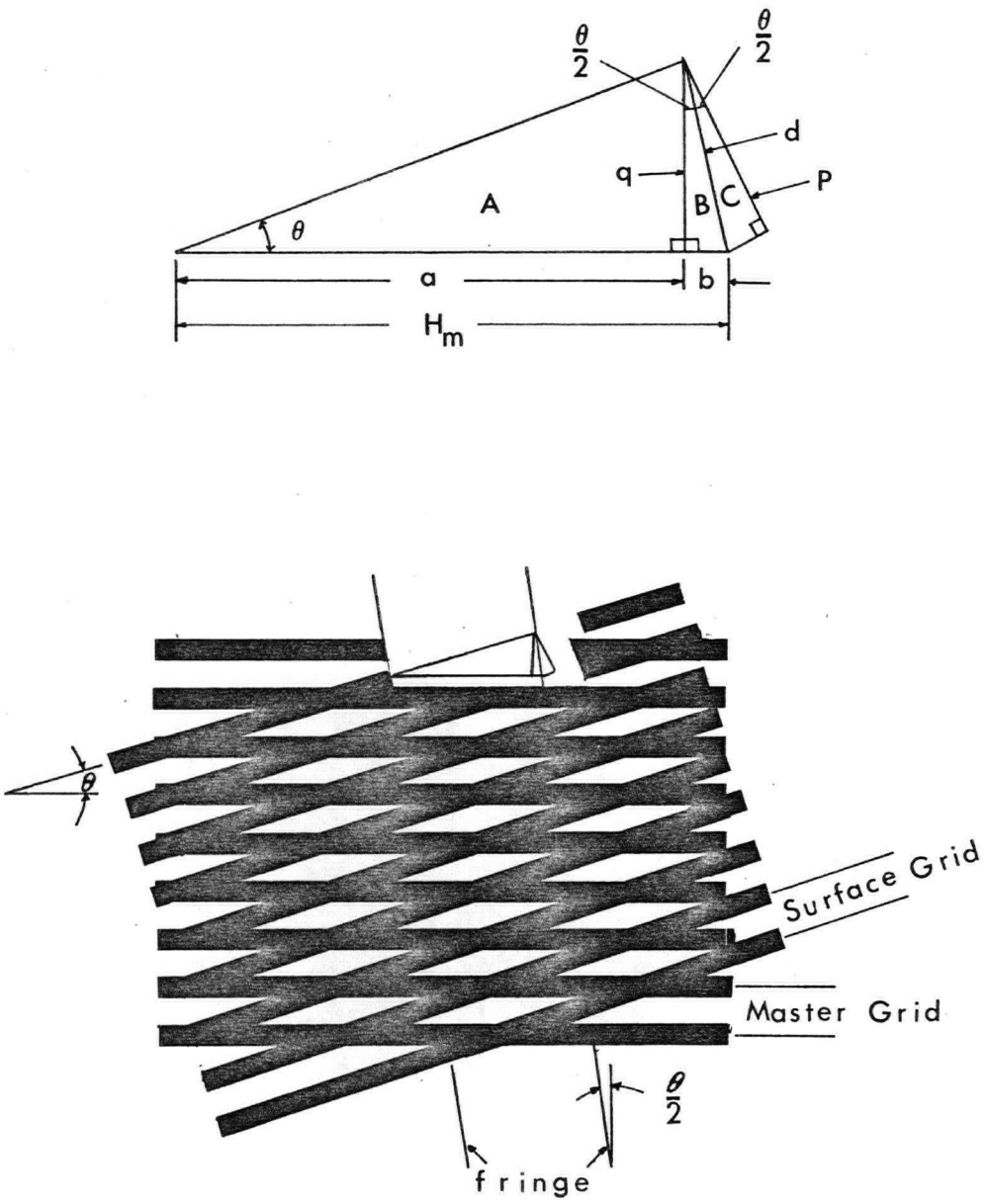

Figure 3. Moire fringe effect, rotation

$$H_m = \frac{P}{\tan\theta} + P \tan \frac{\theta}{2} \qquad [14]$$

By application of trigonometric relations, equation [14] reduces to

$$H_m = \frac{P}{\sin\theta} \qquad [15]$$

Hence

$$\theta = \sin^{-1} \frac{P}{H_m} \qquad [16]$$

Since shear strain γ results in rotation, moire fringes can now be related to shear strain. A surface element distorted by shear is shown in Figure 4b. By definition, $\gamma_{xy} = \tan^{-1} \alpha$. If grid lines were originally horizontal on both surface and master, the fringe pattern would be as shown in Figure 4c and the angle, $\theta_x = (\alpha/2)_x$, can be evaluated as

$$\theta_x = (\alpha/2)_x = + \left|\sin^{-1} \frac{P}{H_x}\right| \qquad [17]$$

The "plus" applies for fringes rotated counter clockwise from a coordinate perpendicular to the master grid. If the grid lines were originally vertical on both surface and master, the fringe pattern would be as shown in Figure 4d and the rotated angle θ_y can be evaluated as

$$\theta_y = (\alpha/2)_y = - \left|\sin^{-1} \frac{P}{H_y}\right| \qquad [18]$$

The "minus" applies for the fringes rotated clockwise from a coordinate perpendicular to the master grid.

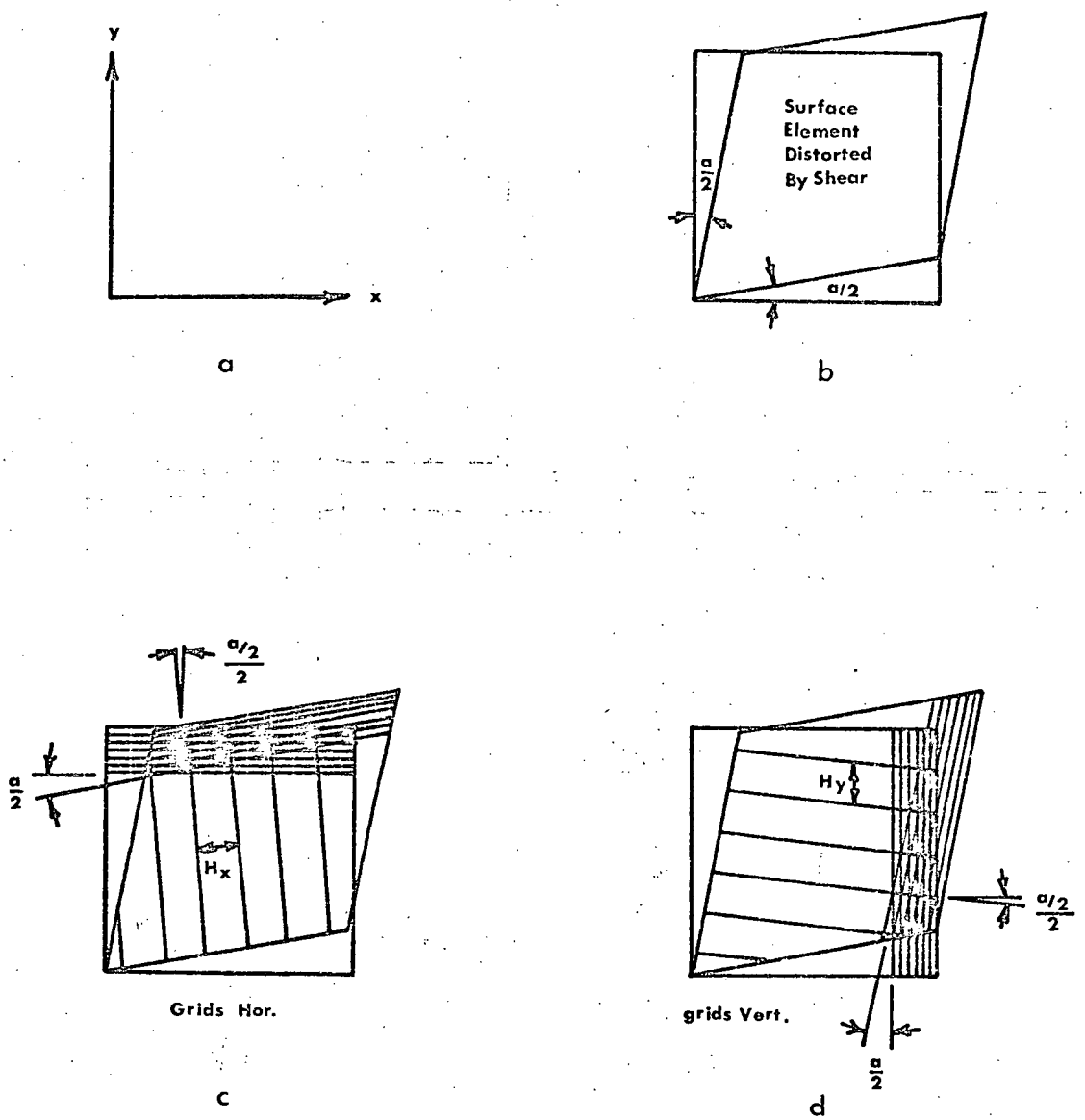

Figure 4. Moire fringe effect, shear strain

Hence the shear strain γ_{xy} is:

$$\gamma_{xy} = \tan^{-1} \alpha = \tan^{-1} [|(\alpha/2)_x| + |(\alpha/2)_y|] = \tan^{-1} (\theta_x - \theta_y) \quad [19]$$

in which θ_x and θ_y can be either plus or minus.

Moire fringe effect and combined normal and shear strain are shown in Figure 5. Using equations [2] and [3], the strain measurement in both tension and compression in a direction perpendicular to its screen lines, is determined by:

$$\varepsilon_x = \frac{P}{D_x \mp P} \quad [20]$$

and

$$\varepsilon_y = \frac{P}{D_y \mp P} \quad [21]$$

where ε_x = strain in x-direction

P = unstrained grid pitch

D_x = distance between two adjacent fringes in the x-direction on a vertical grid

D_y = distance between two adjacent fringes in the y-direction on a horizontal grid

then

$$\gamma_{xy} = \tan^{-1} [(\sin^{-1} \frac{P}{H_x}) - (\sin^{-1} \frac{P}{H_y})] \quad [22]$$

where H_x = distance between two adjacent fringes in the x-direction on a horizontal grid

H_y = distance between two adjacent fringes in the y-direction on a vertical grid.

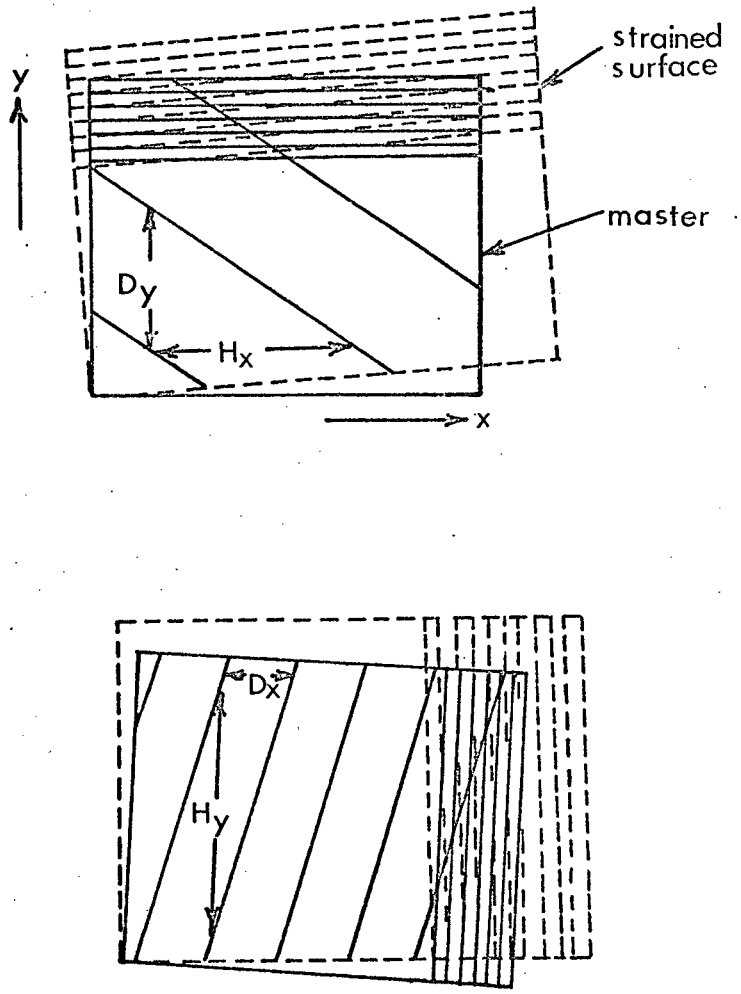

Figure 5. Moire fringe effect, combined normal and shear strain

In cases where D_x and D_y >> P (small strain) the normal strains become:

$$\varepsilon_x = \frac{P}{D_x} \qquad [23]$$

and

$$\varepsilon_y = \frac{P}{D_y} \qquad [24]$$

for either tension or compression.

In cases where H_x >> P and H_y >> P (small angle of rotation),

$$\theta_x = \frac{P}{H_x} \qquad [25]$$

$$\theta_y = \frac{P}{H_y} \qquad [26]$$

and

$$\gamma_{xy} = (\theta_x - \theta_y) \qquad [27]$$

since the sine and tangent functions of small angles are nearly equal to the value of the angle itself.

With θ_x, θ_y, and γ_{xy} known, the principal strains can be computed in the usual manner by equations [7] and [8].

6.4 Modified Strain Equations for Large Deformations

In the case of an infinitesimal deformation the higher-order terms in strain equations may be neglected and we can use the special equations [4] and [5] for normal strains.

However, in the case of a finite homogeneous plane strain which may occur in soft material such as clay soil, the second-order terms are no longer negligible.

We have, therefore, to evaluate real strain from other formulas or adjust from the apparent strain which has been calculated from the special equations. The following more accurate method was developed to calculate the real or Lagrangian strain from the apparent strain obtained from the special equations.

The apparent strains from the special equations, using the measured quantities D_x and D_y are given in equations [20] and [21]. These special equations give, however, the strains on the distorted plane:

$$\varepsilon_x = \frac{OC'' - OC}{OC} \qquad [28]$$

$$\varepsilon_y = \frac{OA'' - OA}{OA} \qquad [29]$$

as shown in Figure 6.

Whereas the Lagrangian strains are:

$$\varepsilon_{rx} = \frac{OC' - OC}{OC} \qquad [30]$$

and

$$\varepsilon_{ry} = \frac{OA' - OA}{OA} \qquad [31]$$

The Lagrangian strain ε_{rx} and ε_{ry} can possibly be calculated from the apparent strains ε_x and ε_y and the rotated angle between surface and master grids θ_x and θ_y which are given in equations [17] and [18].

From Figure 6:

$$OC'' = p + pC''$$

$$= \cos\theta_x \, OC' + \tan\theta_y \, C'p$$

$$= \cos\theta_x \, OC' + \tan\theta_y \, \sin\theta_x \, OC'$$

$$= OC' \, (\cos\theta_x + \tan\theta_y \, \sin\theta_x)$$

since:

$$\varepsilon_x = \frac{OC'' - OC}{OC}$$

and:

$$\varepsilon_{rx} = \frac{OC' - OC}{OC}$$

$$OC' = OC \, (\varepsilon_{rx} + 1)$$

$$OC'' = OC \, (\varepsilon_x + 1)$$

$$OC \, (\varepsilon_x + 1) = OC \, (\varepsilon_{rx} + 1) \, (\cos\theta_x + \tan\theta_y \, \sin\theta_x)$$

$$\varepsilon_{rx} = \frac{(\varepsilon_x + 1)}{(\cos\theta_x + \tan\theta_y \, \sin\theta_x)} - 1 \qquad [32]$$

Likewise we can derive:

$$\varepsilon_{ry} = \frac{(\varepsilon_y + 1)}{(\cos\theta_y + \tan\theta_x \, \sin\theta_y)} - 1 \qquad [33]$$

and

$$\gamma_{xy} = \tan^{-1} (\theta_x - \theta_y) \qquad [34]$$

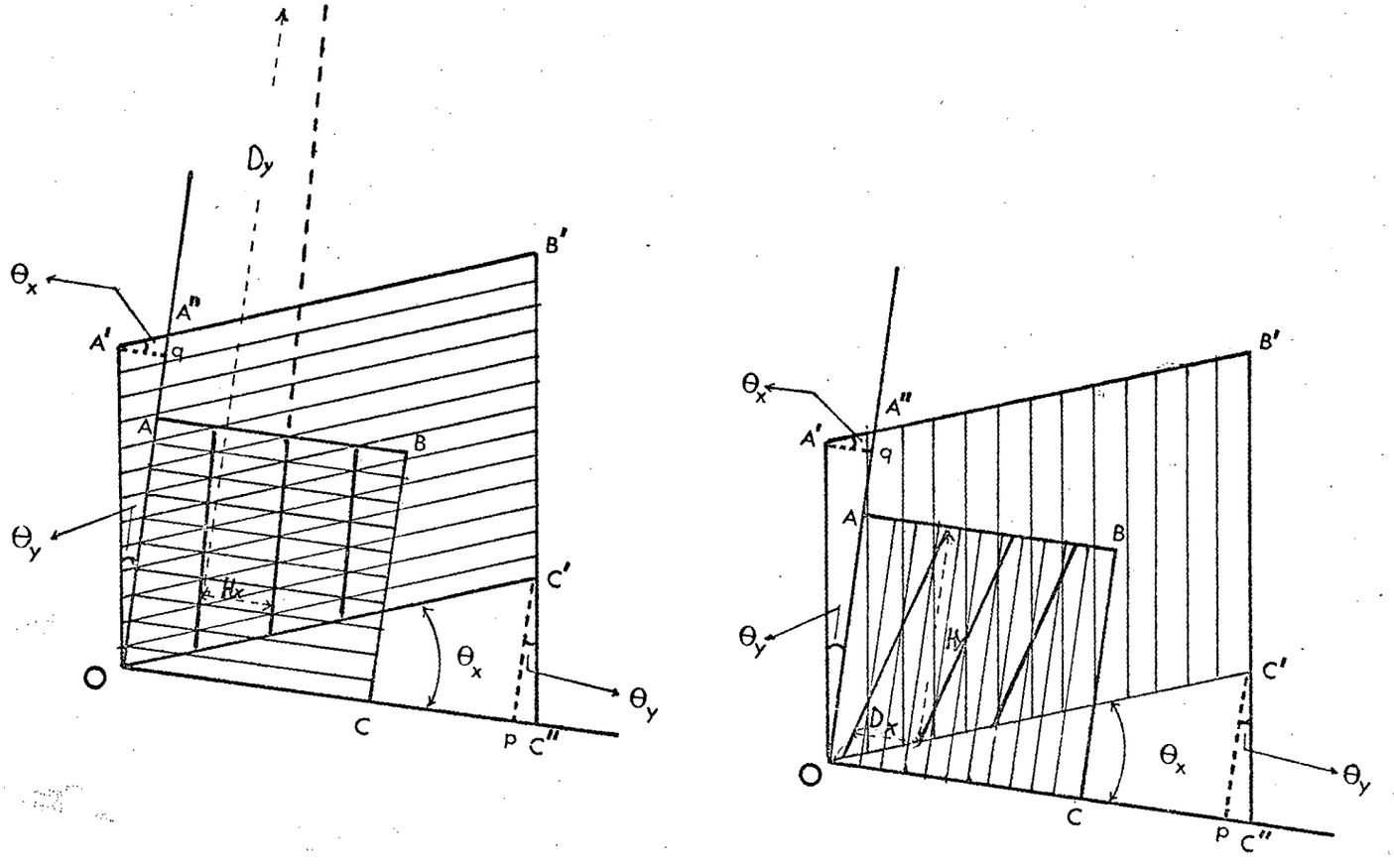

Figure 6. Moire fringe effect, due to large deformation

6.5 Procedure and Apparatus

Since the moire method was developed for the strain measurement of rigid material, such as metals and plastics, a different technique was required for strain measurement in soils.

6.5.1. Moire grids

Photographic methods, etching and thin film technology have been used to provide an array on rigid materials. These are clearly not suitable for soil profiles. Considerable difficulty was encountered in producing consistently good quality grids on different soil types. The following system eventually proved satisfactory. Slots 3.2 mm wide were milled 3.2 mm apart in a 38 cm square sheet of 6.35 mm thick plexiglas. The resulting stencil was placed in a metal frame under tension to remove warping caused by uneven stress distribution. An artists "air brush" was used to spray a mixture of powdered carbon and alcohol through the slots in the stencil on to the prepared soil profile in a plexiglas container. The master grids were supplied by a Decal company which provided a matching grid of 3.2 mm black lines on a mylar film. This provided a set of clean cut lines with a spacing error of $\pm$ 1.5 percent.

Better results were obtained using carbon powder mixed with alcohol than using black paint. Alcohol was

quickly evaporated as carbon powder was deposited on the soil surface. This method not only eliminated the cohesion properties of paint but also reduced the friction between master and surface grids. The friction was further reduced by coating the soil-soil box interface with a thin layer of fine glass beads before spraying on the surface grid. The surface of the master grid and tools were also cleaned with acetone before each test.

The fringes formed were recorded by camera as loading progressed. Fringe measurements were made from the photographs together with the scale factor to bring all measurements to an absolute value. Normal strains, shear strains, maximum and minimum principal strains and maximum shear strains were measured.

6.5.2. Soil preparation

Tests were carried out on remolded Haney clay and on mixtures of Haney clay and Ottawa sand (10-20 mesh). Upper and lower plastic limits of the clay were 47.9 and 19.8 percent, respectively.

To obtain uniform mixtures, dry clay and sand were placed in a sealed container and tumbled to a uniform mix. The soil mix was cooled below freezing before mixing with powdered snow and then warmed to achieve a uniform moisture content. The same mixing

method was used for all soil preparation required for experiments reported in this total study.

The conditioned soil was placed in a box and compacted with flat plates which were mounted in an Instron Testing Machine and loaded to eliminate air pockets and obtain uniform mechanical conditions.

Two different types of soil were used:

	Clay	Silt	Sand
Type I	45%	37%	18%
Type II	33%	28%	39%

Soil Type II compacted to a bulk density* of 2.19 grams/cm^3 and 13 $\pm$ .5 percent moisture content was used for square plate tests, which are described in the next section. The remaining tests were conducted on soil Type I with a bulk density of 1.9 grams/cm^3 and moisture content of 12.5 $\pm$ .5 percent. All moisture contents were determined on a dry weight basis by gravimetric methods with oven drying. Density was measured by a clod method and modified core method. The modified core method consisted of taking a known weight and volume by pressing a cylindrical can into the soil specimen and trimming the top of the filled cylinder. The sample was then dried to 105°C and weighed. Bulk density was obtained by dividing the wet soil weight by the filled sample volume.

---

* Density values given in this study are calculated on wet basis.

6.5.3. The test soil-machines

Three scaled soil-machines were studied; wedges, flat blades and a square plate. Wedge apex angles of 35° and 50° were cast from liquid plastic in a mould and machined to the desired size after curing. Flat blades and the square plate were made of .6 cm thick plexiglas. The bottom of the blade was sharpened to avoid a blunt edge. The wedges and square plate were mounted on an inverted compressive load cell of an Instron tester. Instron loading equipment is shown in Figure 7. The flat blade was mounted on a rigid frame as shown in Figure 21 and was pulled by the Instron through a pulley system.

6.5.4. Soil bin and test box

The conditioned soil was placed in a box 35 cm wide, 27 cm tall and 15 cm deep made of 1.5 cm thick plexiglas. The soil was compacted to eliminate pockets of air and to reproduce reasonably consistent mechanical conditions. A square plate was mounted in an Instron testing machine to investigate the force required to deform the soil to a fixed depth. This test was used as a check on the reproducibility of the soil's mechanical condition. This soil box was also used for the wedge tests.

As shown in Figure 21, the small soil bin 60 cm

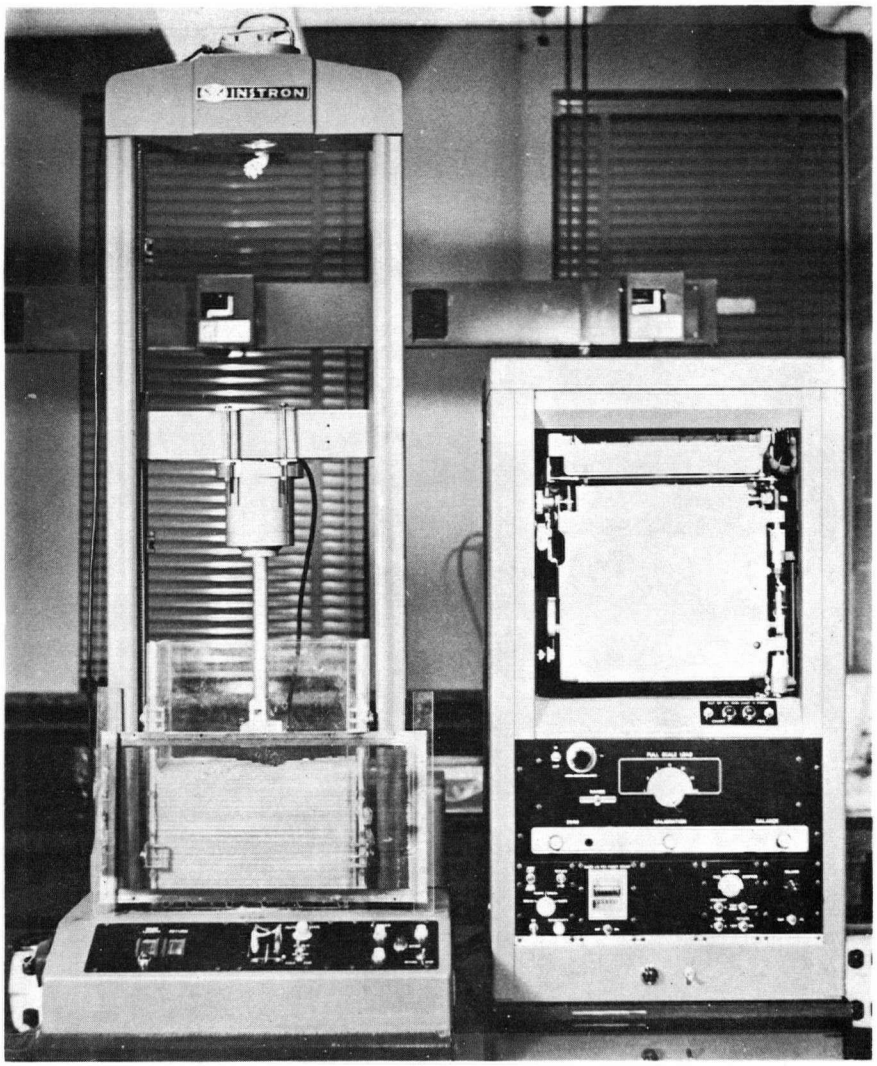

Figure 7. Instron loading equipment and soil box

long, 30 cm wide and 22 cm tall, made of thick plexiglas, was prepared for the blade tests. Rubber guide wheels were used to minimize vibration during the tests. The tension load cell was used to measure the pull required to move the flat blade through the soil. The soil bin was pulled by the Instron while the load cell was connected to the draw-bar through a pulley system.

6.6 Results and Discussion

The following results were obtained from strain curves which were derived from the spacings between the interference fringes along lines at 5 mm intervals drawn on the photographs in both the horizontal and vertical direction.

These results provided valuable information on soil behavior to the intrusion of soil-machine systems. Surface hardening effects after bulldozing, soil in response to a geometrical change of a tool and other essential deformation patterns for design parameters were observed. Due to the lack of information on soil deformation measurement by others limited practical comparison of test results was possible.

6.6.1. Wedge-shaped tools

Cast plastic wedges 10 cm long with apex angles of 35° and 50° were used to apply compressive loads at the rate of 2 cm/min. to the soil. Moire patterns were

photographed with a 35 mm camera to obtain x and y displacements up to 7 cm of tool penetration.

Composite moire patterns yielding x - y displacements are shown in Figures 8 and 9 for 50° and 35° wedges respectively. The strain analyses for the same is shown in Figures 12 and 13 for 50° wedge and in Figures 10 and 11 for 35° wedge.

Large compressive displacements and a clear indication of compressive to tensile transition surfaces are shown on the horizontal grids (y-displacements). Maximum shear strain analysis for the 35° and 50° wedges are shown in Figures 14 and 15 respectively.

The strain analysis of y-displacements shown in Figure 10 and 12 differ only in magnitude between 35° and 50° wedges. However, the x-strains are different in both magnitude and pattern. More uniform strain gradients were found under the 35° wedge. It should be noted that non-uniform strains in the x-direction occurred for both 35° and 50° wedges near their tops (in this case at the soil surface) and also in the middle portion of the 50° wedge. It is assumed that this non-uniformity is induced by the y-displacements.

The upper 30 percent of penetration on the 35°

wedge showed a large tensile strain gradient. The 50° wedge showed a uniform strain field throughout. This difference is due to apex angle effect. The plane of transition or plane of maximum shear strain is clearly evident in both tests. Progressive moire fringe patterns under the 50° wedge are shown in Figure 24.

6.6.2. Strains under the rectangular plate

Plexiglas models of footings 5.5 cm by 10 cm were loaded at the rate of 5 cm/min. until 3 cm of displacement occurred. Figure 16 is a composite of moire fringe patterns. Analyses of x and y-strains are shown in Figure 18 and Figure 19.

Figure 17 shows progressive y-displacement patterns. Similar to the results for wedge-shaped tools transition planes are clearly shown on the horizontal grids. Large compressive strains are shown directly below the footing and tensile strains on both sides. Approximately half of the center portion of the footing is free of x-displacements. Determination of displacement in high clay content soils under a flat plate was never fully investigated [67] and has been a problem in the construction industry.

The rectangular plate loaded to 1,5 Kg/cm^2 showed a very high compressive strain gradient in the y-direction under the entire footing. Uniform but flatter tensile gradients occurred at the sides of the footing but to

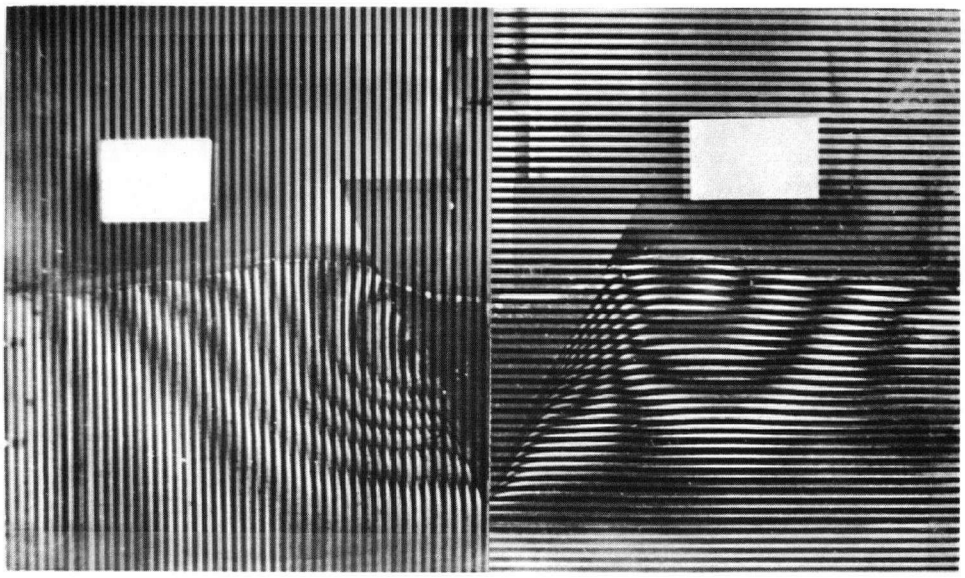

Figure 8. Overall view (X and Y displacements) of Moire fringe patterns induced by a 50° wedge.

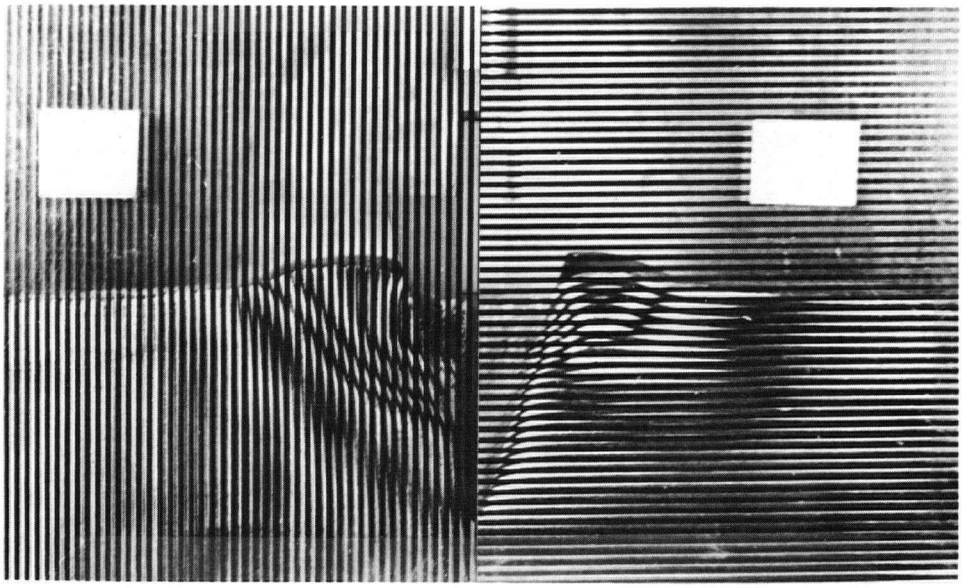

Figure 9. Overall view (X and Y displacements) of Moire fringe patterns induced by a 35° wedge.

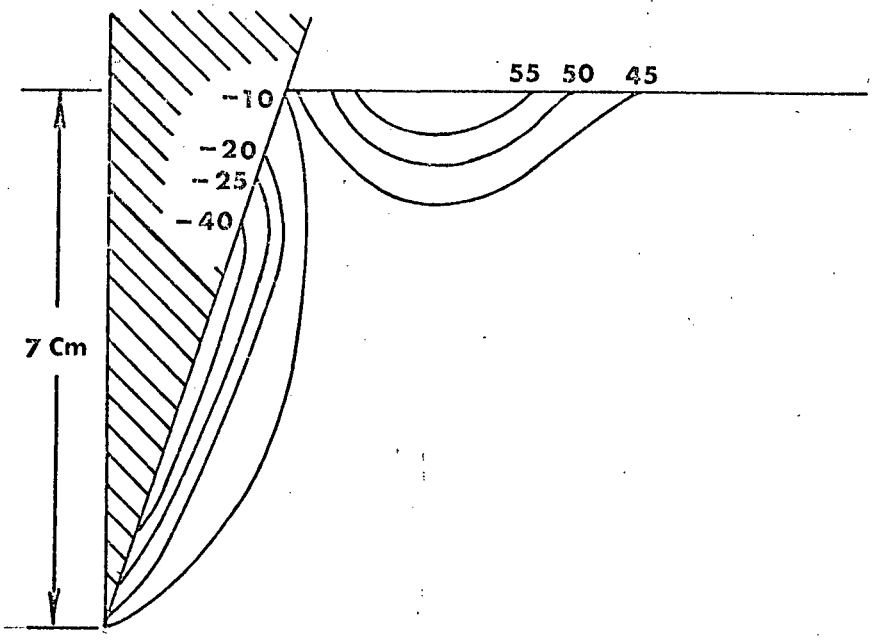

FIGURE 10. Percent strain in y-direction induced by 35° wedge after 7 cm penetration. Rate of loading = 2 cm/min. Applied load = 49.3 Kg.

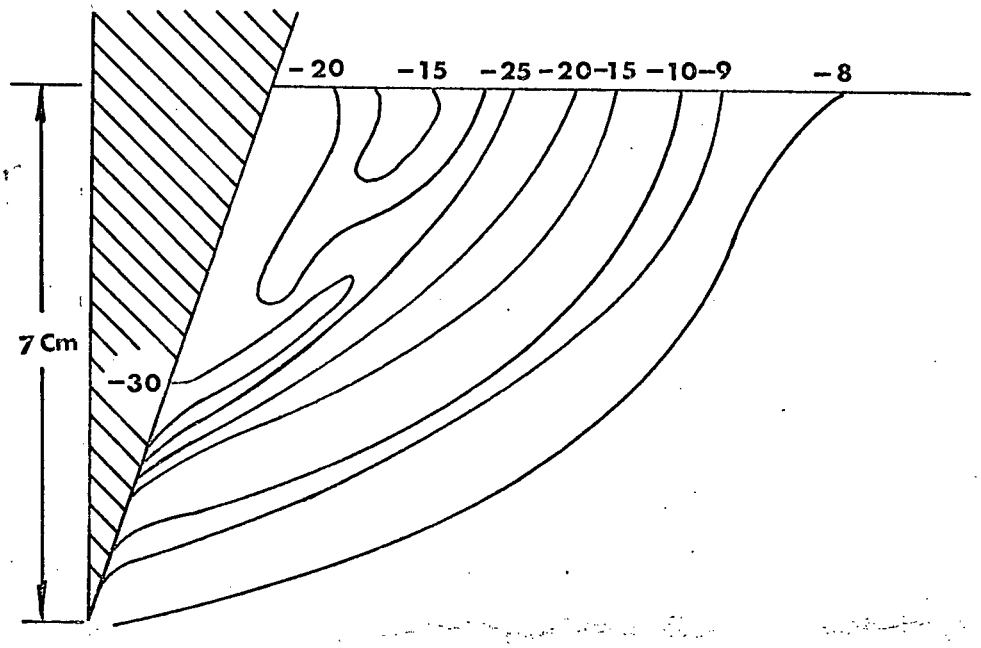

FIGURE 11. Percent strain in x-direction induced by 35° wedge after 7 cm penetration. Rate of loading = 2 cm/min. Applied load = 49.3 Kg.

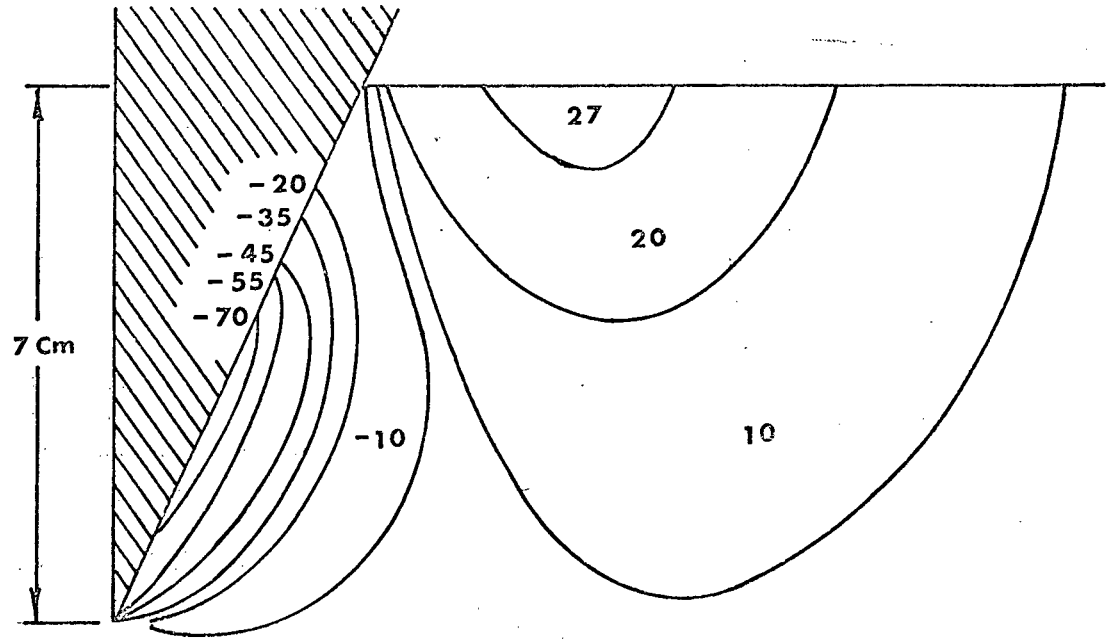

FIGURE 12. Percent strain in y-direction induced by 50° wedge after 7 cm penetration. Rate of loading = 2 cm/min. Applied load = 69.8 Kg.

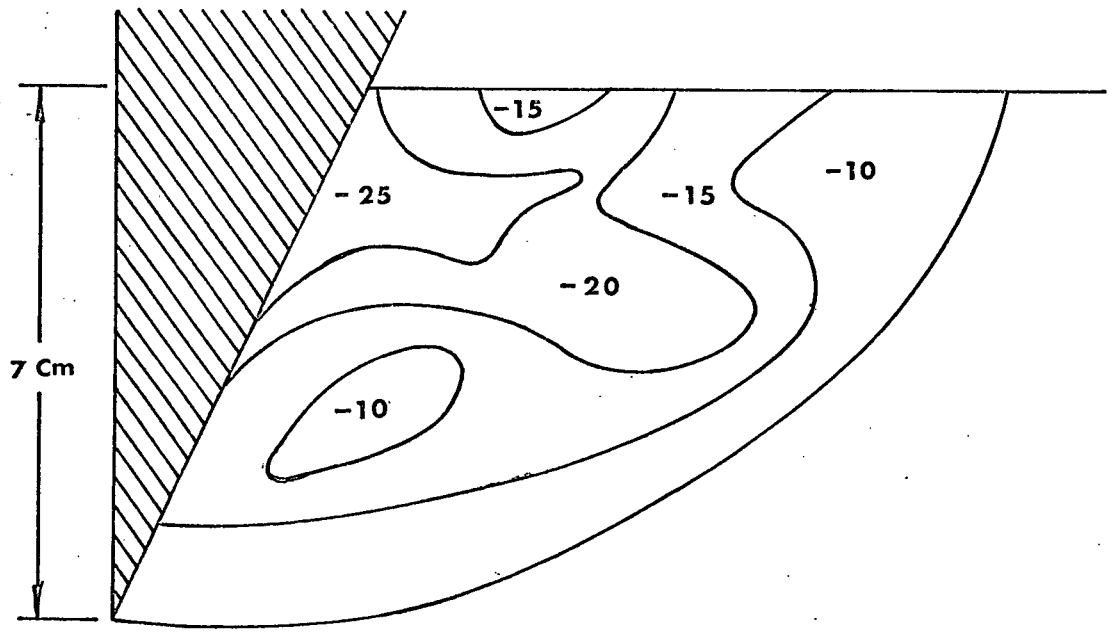

FIGURE 13. Percent strain in x-direction induced by 50° wedge after 7 cm penetration. Rate of loading = 2 cm/min. Applied load = 69.8 Kg.

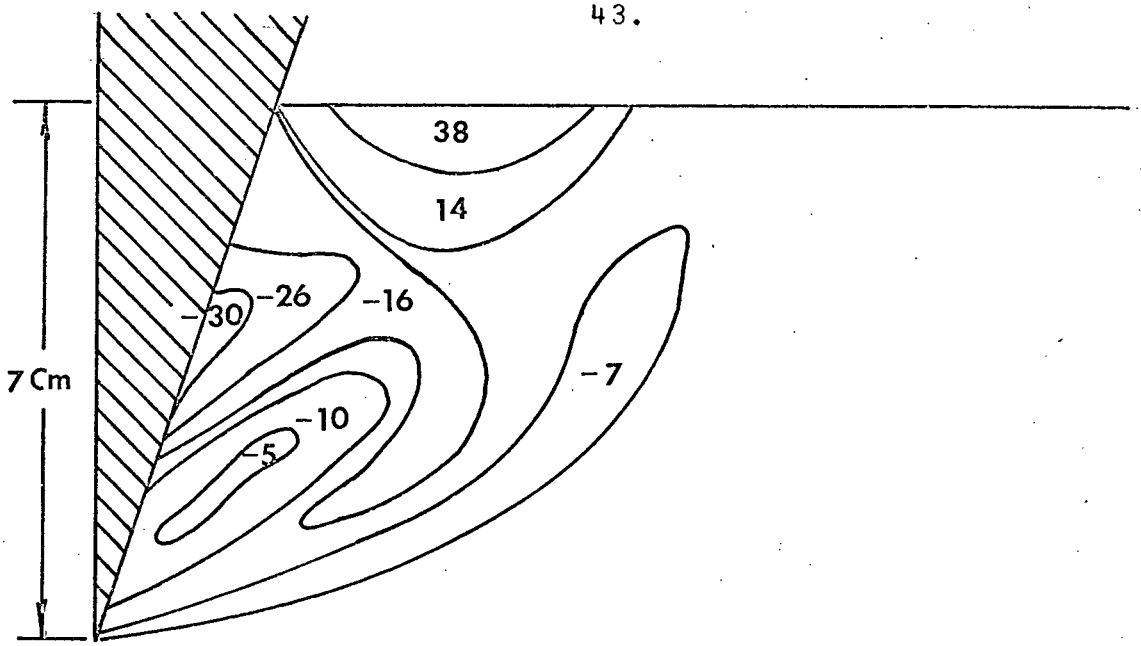

FIGURE 14. Maximum shear strain in percent induced by 35° wedge after 7 cm penetration. Rate of loading = 2 cm/min. Applied load = 49.3 Kg.

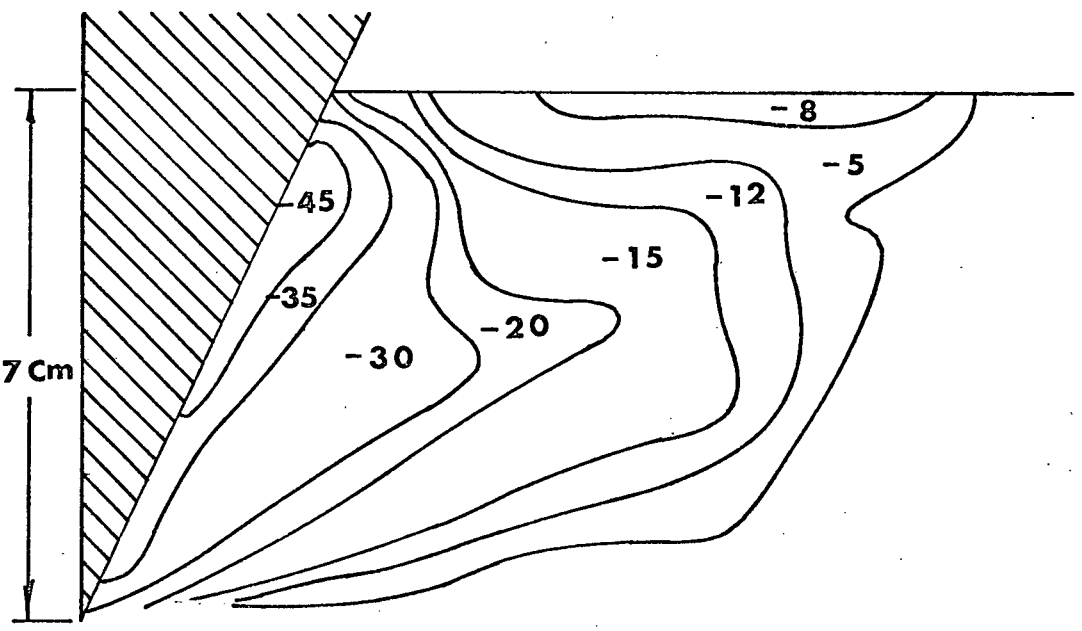

FIGURE 15. Maximum shear strain in percent induced by 50° wedge after 7 cm penetration. Rate of loading = 2 cm/min. Applied load = 69.8 Kg.

depths considerably below the compressive strains. More than 60 percent of the strain change, immediately under the footing, occurred within one half of the total penetration.

In contrast to y-displacements the x-displacements occurred well away from the footing center line. Strain intensity was of the order of 11 percent. Since measured x-displacements were very small, it can be assumed that a uniaxial stress condition was applied. Hence stress-strain relationships may be constructed for a low stress field when large volume strains do not occur. A more abrupt transition plane occurred under the footing than for the wedges. This sharp change is due to the edge effect of the footing and to soil texture. Maximum shear strain patterns under the rectangular plate are given in Figure 20.

6.6.3. Vertical and inclined blades

Plexiglas models of chisel tools mounted at 90° and at 45° to the direction of travel were used to compare soil displacements. Loading rates of 2 cm/min. for both vertical and 45° tools were used. Figures 27 and 28 compare x and y-displacements for the 45° mounted tool and Figures 29 and 30 show the same for the 90° mounted tool. Progressive displacement patterns for both tools are shown in Figures 22

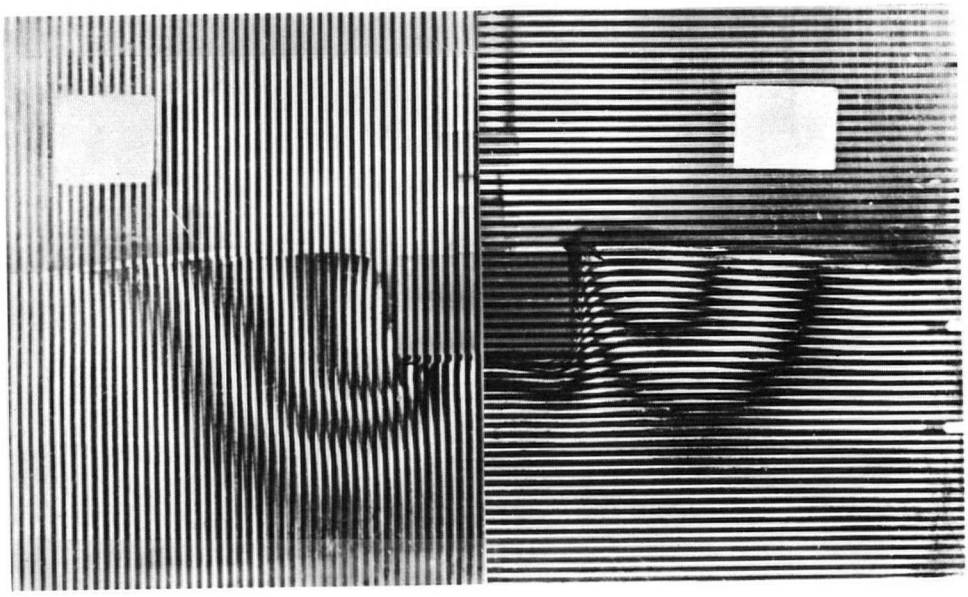

Figure 16. Overall view (X and Y displacements) of Moire fringe patterns under a model footing.

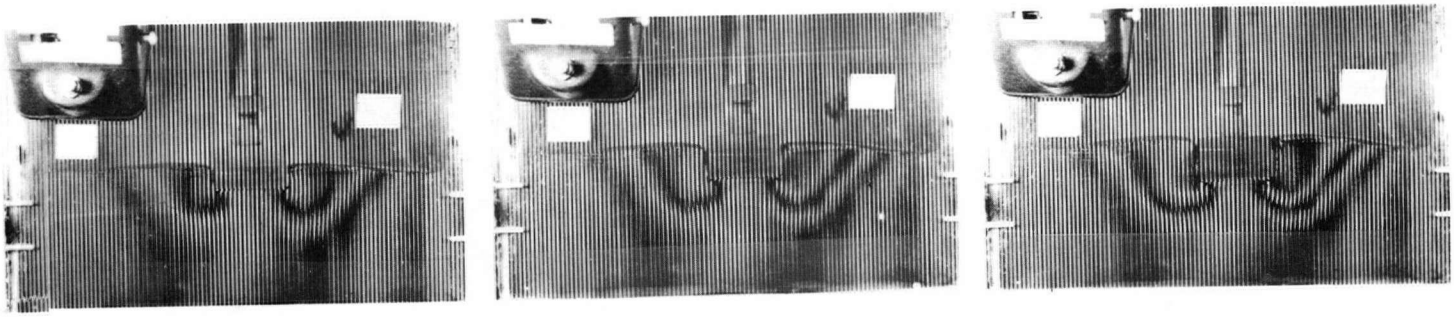

(a) (b) (c)

Figure 17. Moire fringe patterns under progressive loading: (a) after 17 sec. elapsed; (b) after 23 sec. elapsed; (c) after 31 sec. elapsed from initial load. Rate of loading = 5 cm/min.

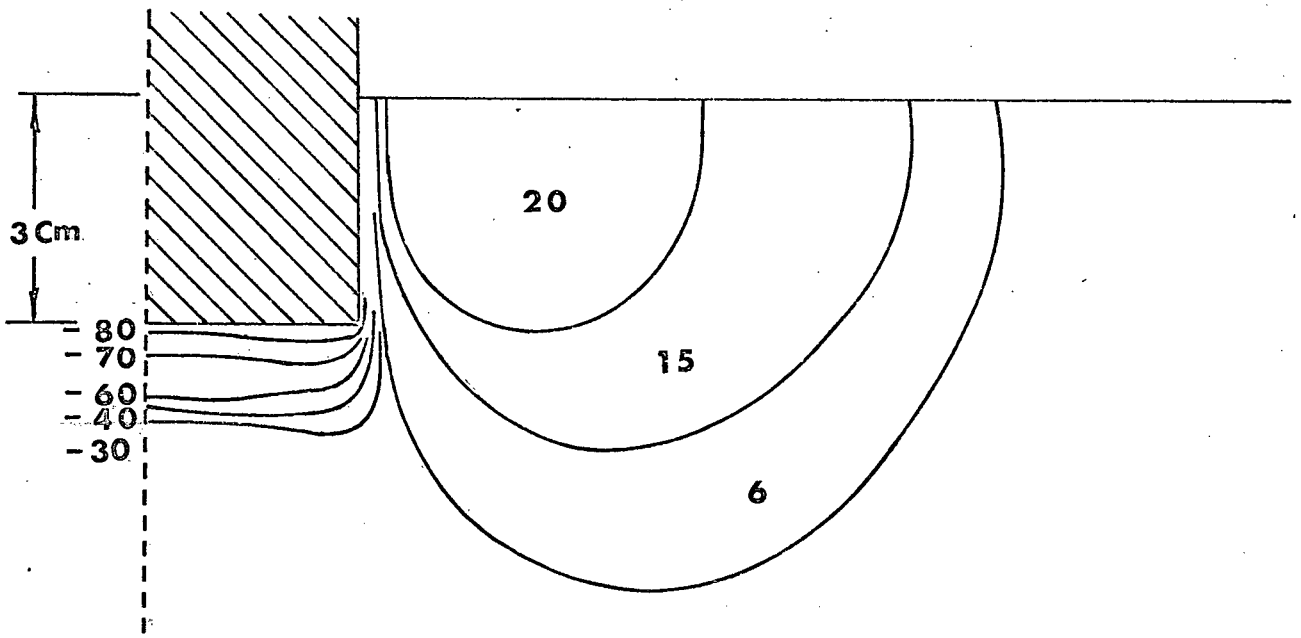

FIGURE 18. Percent strain in y-direction under a model footing after 3 cm settlement. Rate of settlement = 5 cm/min. Applied load = 82.5 Kg.

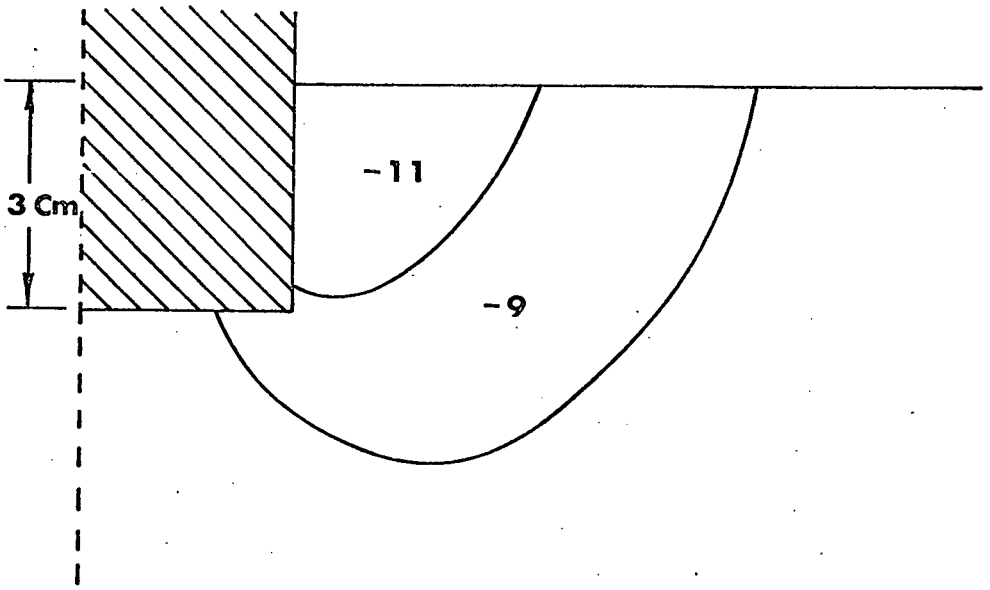

FIGURE 19. Percent strain in x-direction under a model footing after 3 cm settlement. Rate of settlement = 5 cm/min. Applied load = 82.5 Kg.

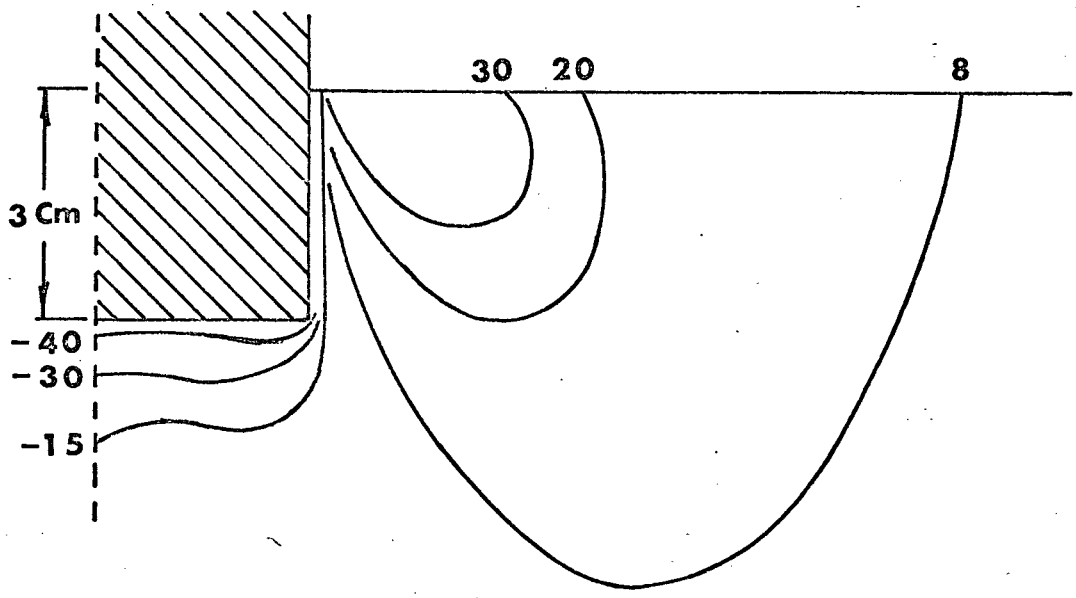

FIGURE 20. Maximum shear strain in percent under a model footing after 3 cm settlement. Rate of settlement = 5 cm/min. Applied load = 82.5 Kg.

and 23. Strain analyses of both tests are shown in Figures 25 and 26 for the inclined blade and Figures 31 and 32 for the vertical blade. Large tensile y-strains immediately in front of the 90° mounted blade are evident but the 45° mounted blade produces more uniform soil displacements.

As shown in Figures 25 and 26 the x - y strains induced by the movement of a 45° tilted blade shows relatively uniform and similar strain patterns in both x and y-directions except for larger strains in the direction of tool movement. Similar strain patterns were to be expected because of tool symmetry with the x and y axes.

Vertical blades have a substantially different strain field from sloped blades as shown in Figures 31 and 32. A build up of soil was noticed at the sharp edged tip of the blade which forced soil to move downward causing compaction. However the compacted area was very thin. High strain gradients occur in both the x and y-direction in the region near the tool tip. The strain field expands forward and upward to the soil surface.

Kostritsyn (34) studied a vertical cutter and noted that near the surface, soil would rupture or move upward, but at greater depths the movement was

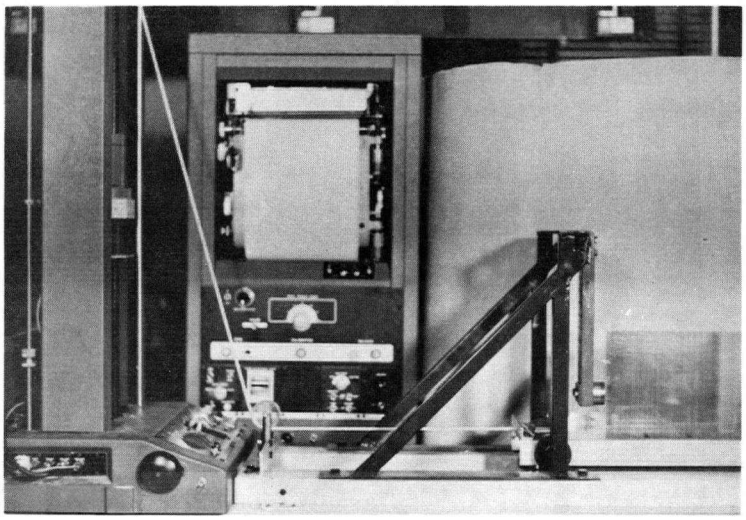

Figure 21. Instron instrumentation as a pull source for blade tests

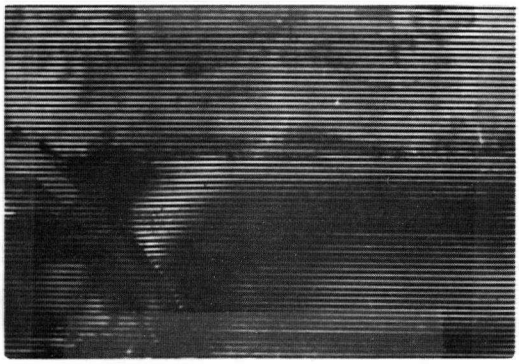

(a)

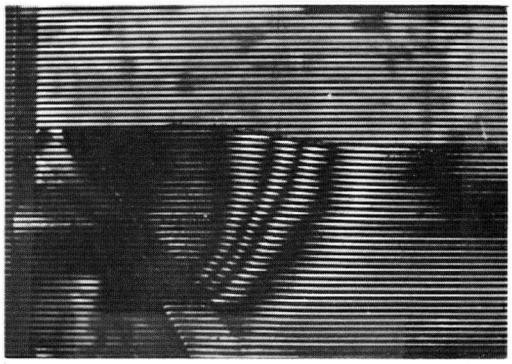

(b)

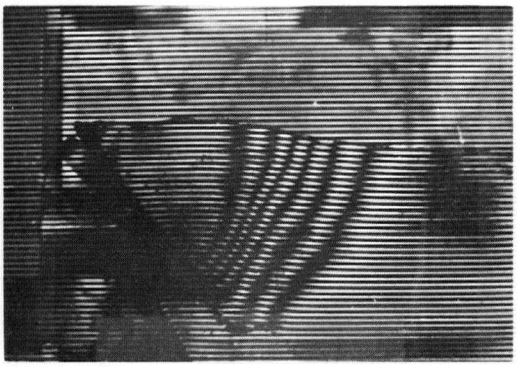

(c)

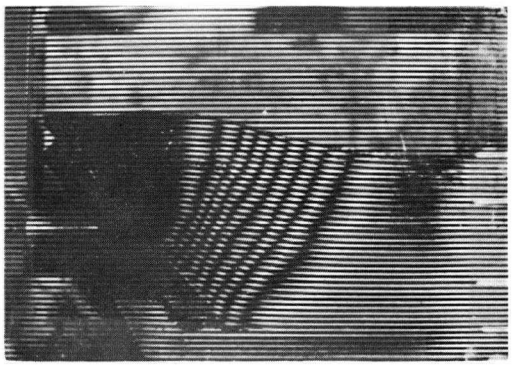

(d)

Figure 22. Moire fringe patterns under progressive blade movement. Blade angle 45°. Y - displacement.

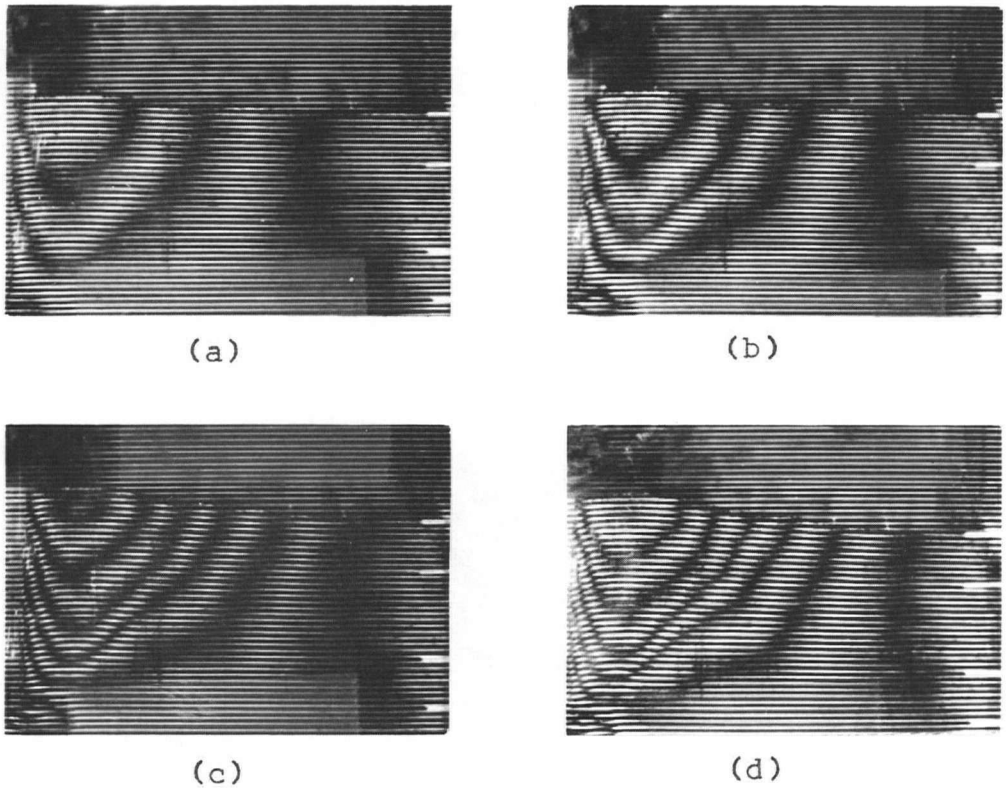

(a) (b)

(c) (d)

Figure 23. Moire fringe patterns under progressive blade movement. Blade angle 90°. Y - displacement.

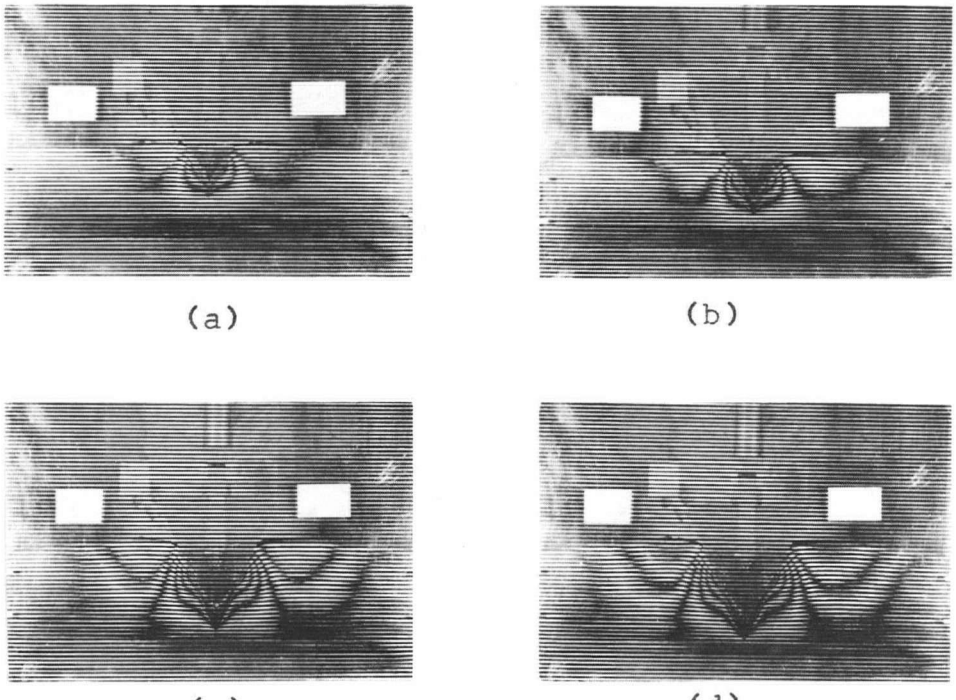

(a) (b)

(c) (d)

Figure 24. Moire fringe patterns under progressive intrusions of a 50° wedge.

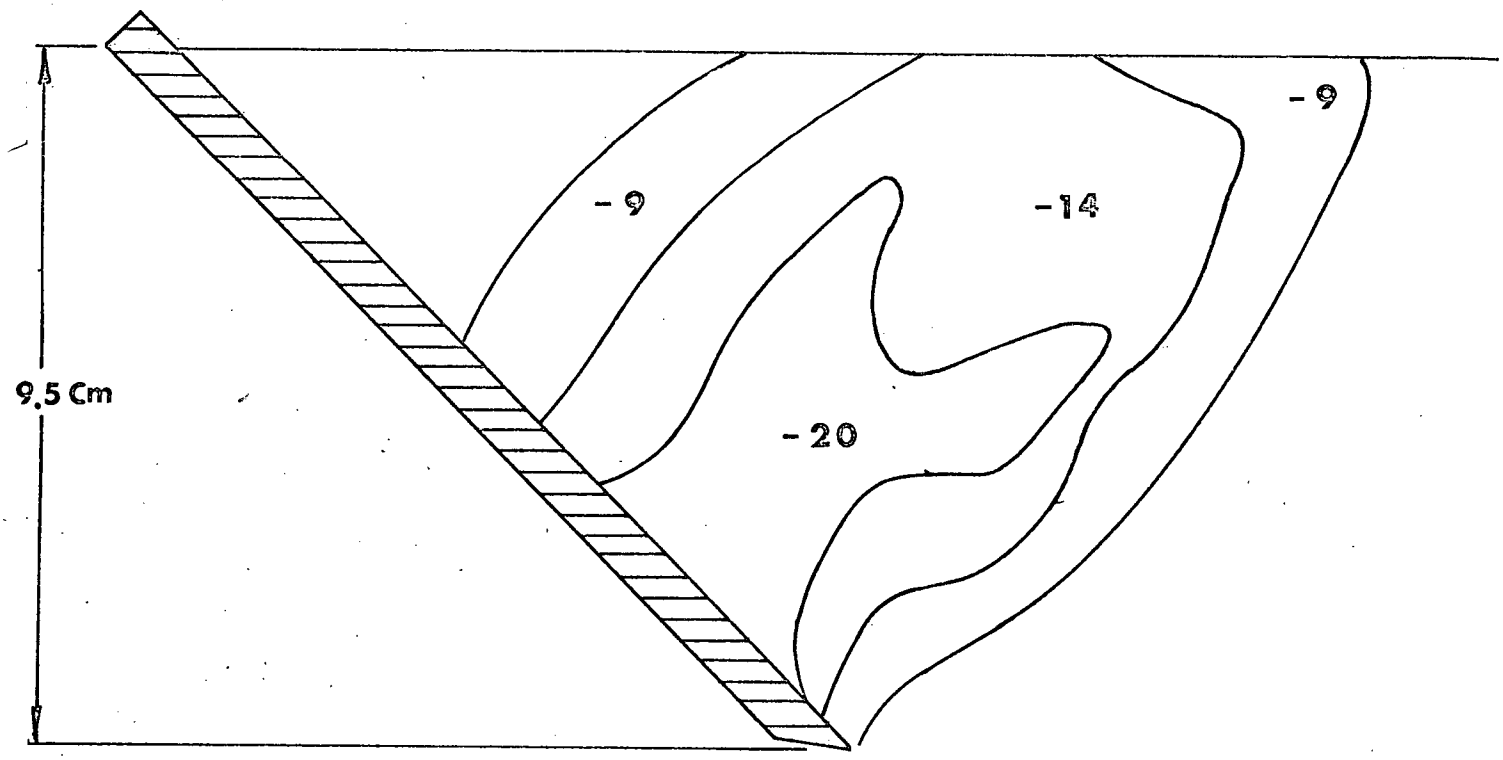

FIGURE 25. Percent strain in y-direction induced by a 45° tilted model flat blade after 21.5 Kg load application. Tool speed = 2 cm/min.

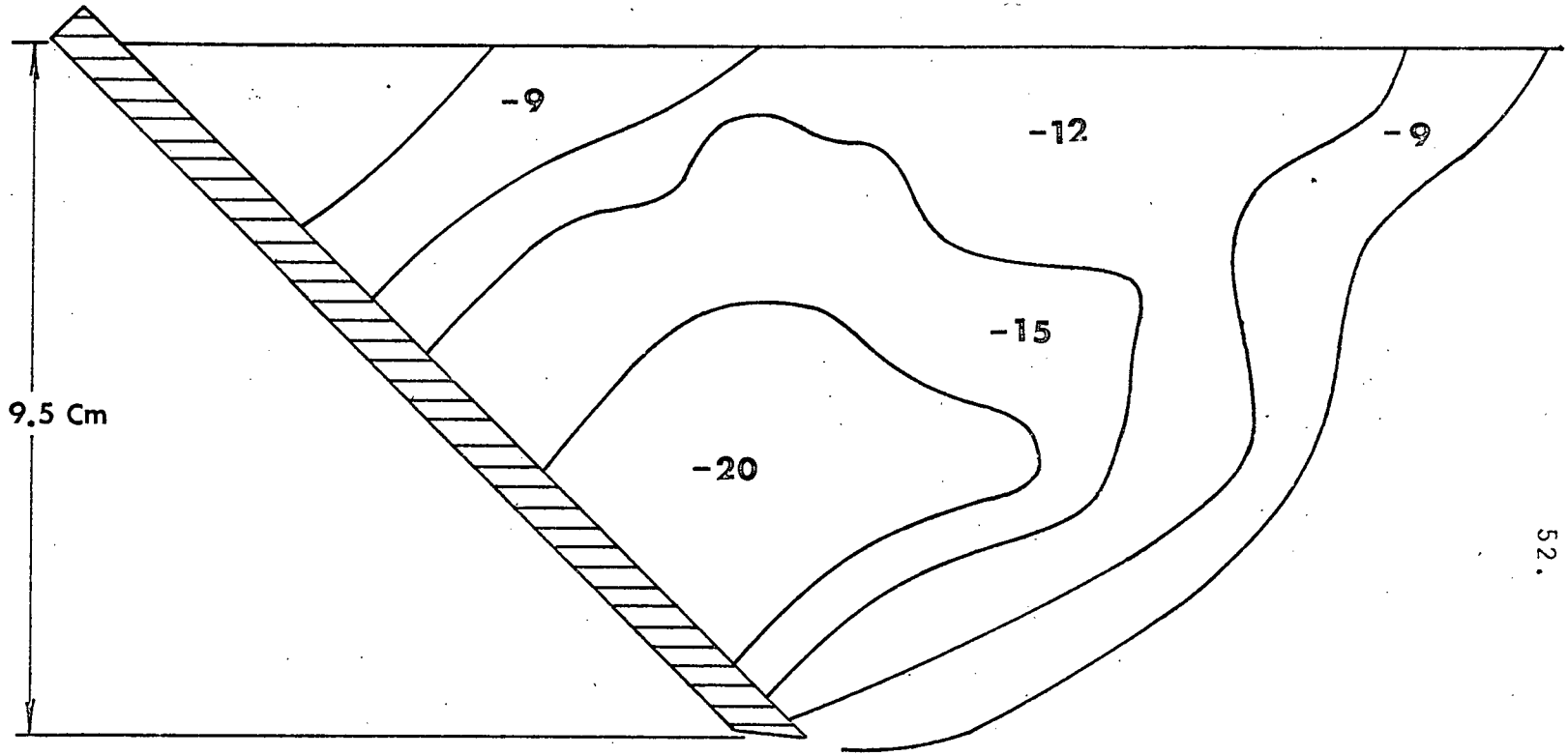

FIGURE 26. Percent strain in x-direction induced by a 45° tilted model flat blade after 21.5 Kg load application. Tool speed = 2 cm/min.

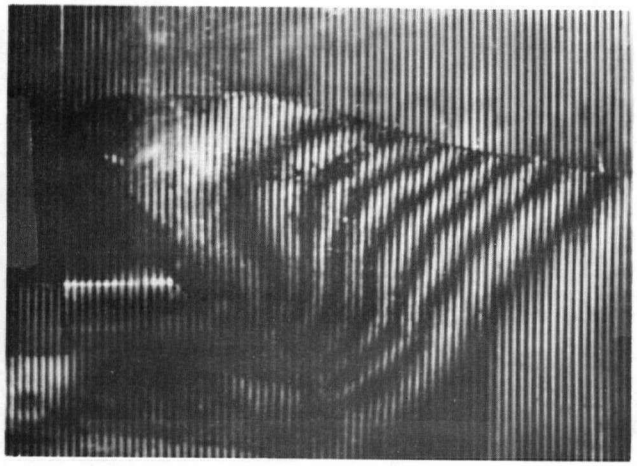

Figure 27. Moire fringe patterns induced by 45° blade movement.
X - displacement.

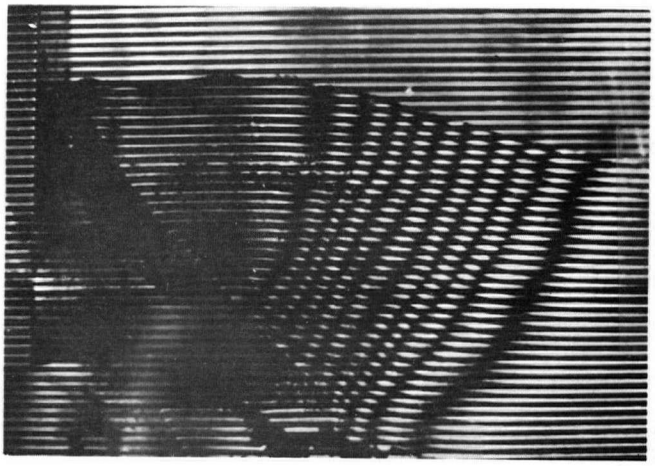

Figure 28. Moire fringe patterns induced by 45° blade movement.
Y - displacement.

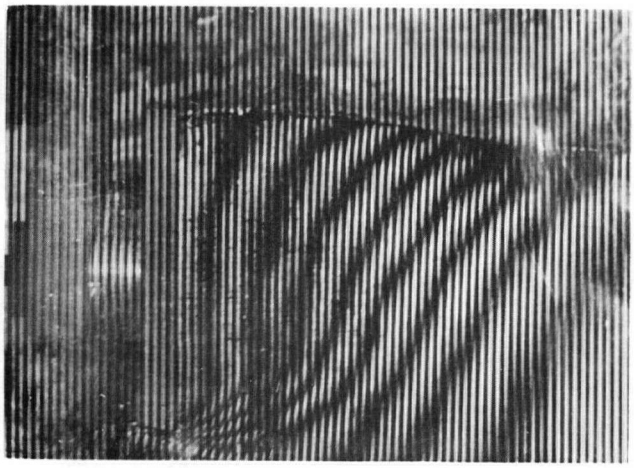

Figure 29. Moire fringe patterns induced by 90° blade movement.
X - displacement.

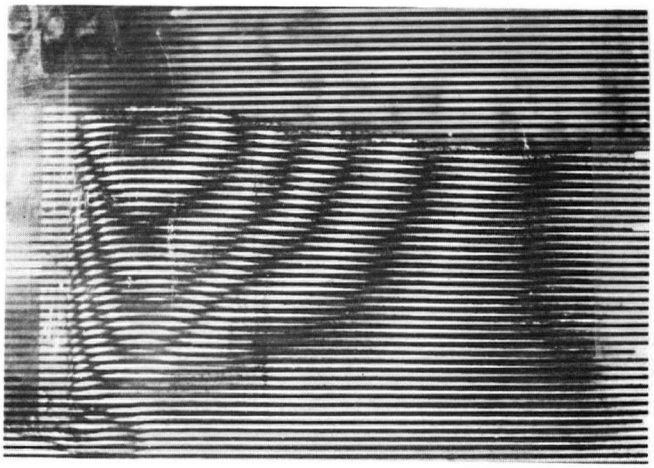

Figure 30. Moire fringe patterns induced by 90° blade movement.
Y - displacement.

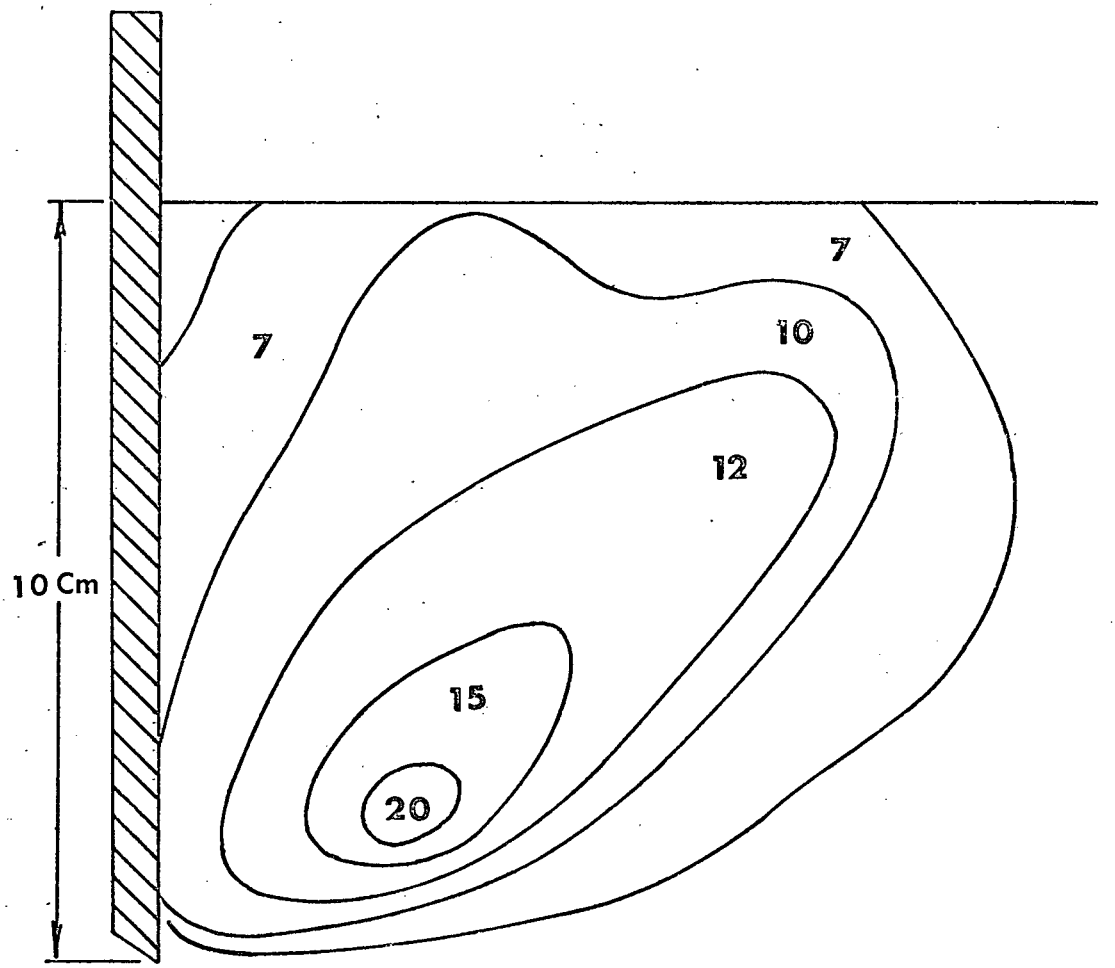

FIGURE 31. Percent strain in y-direction induced by a vertical model flat blade after 32 Kg load application. Tool speed = 2 cm/min.

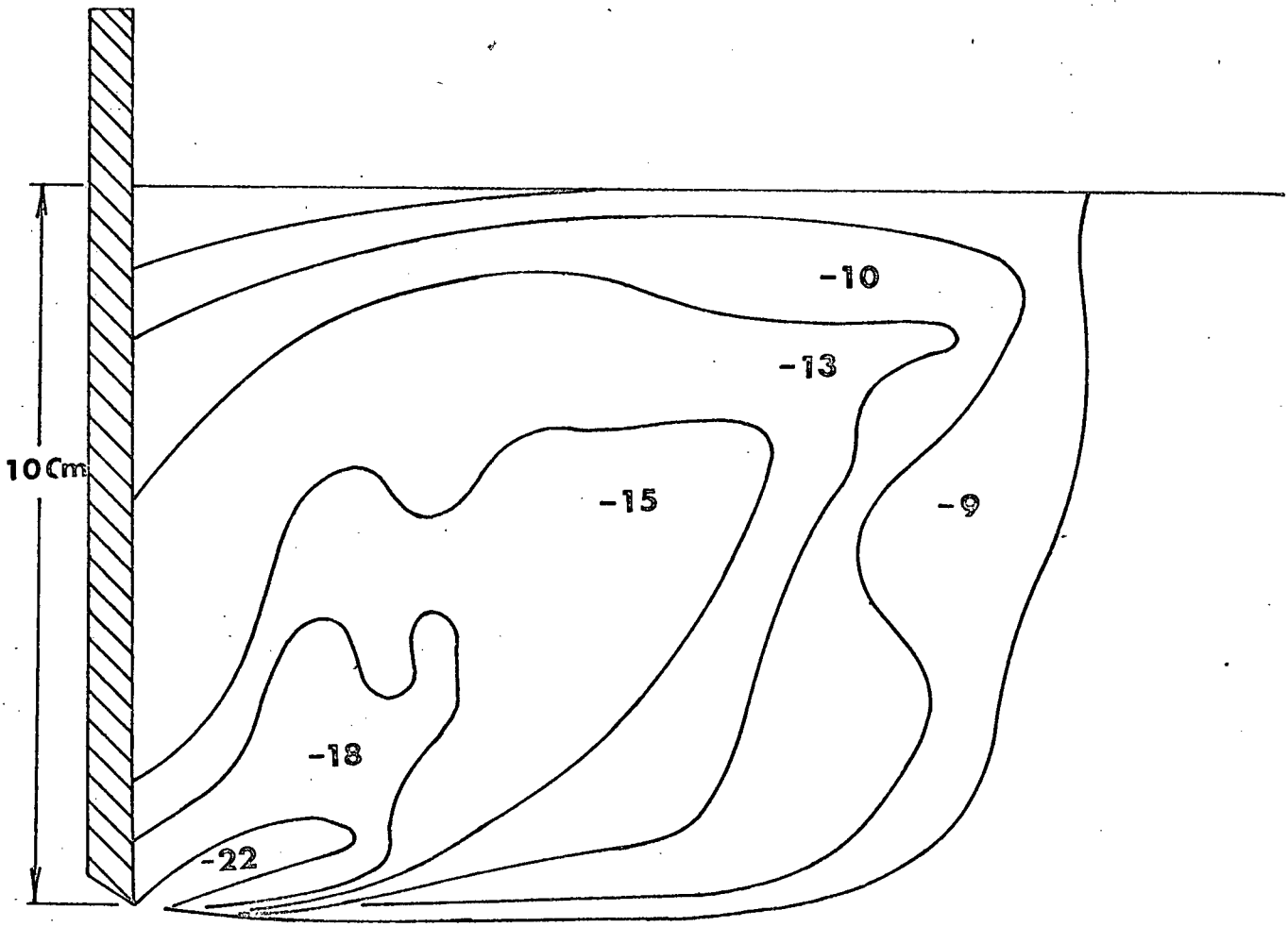

FIGURE 32. Percent strain in x-direction induced by a vertical model flat blade after 32 Kg load application. Tool speed = 2 cm/min.

parallel to the direction of blade travel. This claim is only partially correct as slip lines, even at greater depths, can not be parallel to the direction of blade travel. This phenomenon was clearly observed during moire experiments. Kostritsyn also did not observe surface hardening which is caused by the blade's sharp edged tip forcing soil to move downward.

These results are very encouraging indicating that the moire technique can be used to check the type and degree of soil manipulation by a soil machine, or it can be used to make initial investigations of new soil machine designs.

Double grid techniques should be tried for an overall strain analysis when desired soil physical properties cannot adequately be reproduced. The methods reported in this study gave approximately 5 percent strain resolution. High precision can be achieved by fringe multiplication techniques or by using a smaller grid pitch. A high speed camera can be used in situations involving high loading rates.

7. STRESS AND STRAIN RELATIONSHIPS IN SOIL

7.1 General Review

The moire method provides the measurement of soil deformation to the intrusion of soil-machines. Stress-strain relationships are required for logical design of soil-machine systems since measured displacement must be related to the force required to produce it.

Compression tests and direct shear tests are two examples of several possible methods of establishing stress-strain relationships in soil. A compression test has an advantage over direct shear tests as progress effects are smaller and the state of stress is known at all stages during the compression test. Existing compression methods produce bulging in the middle zone with a resultant non-uniform distribution of compressive stress especially at the ends of the specimen. Rowe (52a) has studied the importance of maintaining free displacements at the loading head during triaxial tests and Scott (61) indicated that information on the details of the stress-deformation behavior of material obtained from the usual compression test can be accorded only qualitative value.

The ends of a test specimen subjected to flat plate loading are hindered from expanding laterally due to friction, which results in stress concentrations at the edges as shown in Figure 39b. Lambe's (34a) illustration of the problem is shown in Figure 33(a). Dead zones occur at the top and bottom where practically no strain occurs. The center zone undergoes considerably greater strain than

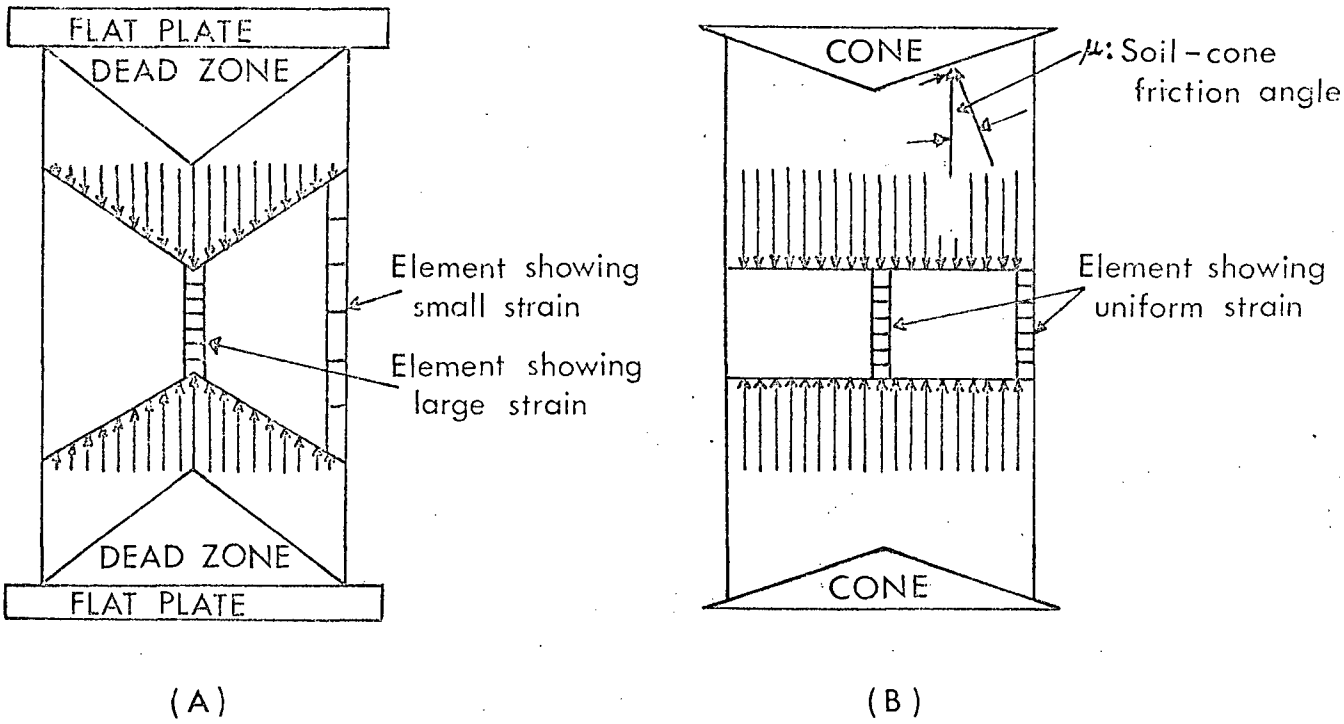

Figure 33. Displacements in axial compression test.
(A) Compression between flat plates.
(B) Compression between cones.

the edges. This difference was measured by using the moire method. Strains at the edges were computed by the moire technique and the total deformation of the center zone was directly measured by using a dial gauge. The differences were significant and increased with increase in deformation as shown in Figure 40. Hence existing methods do not provide uniaxial stress fields, and it was not possible to develop accurate stress-strain relations. To overcome this problem the following modified technique was developed.

Since non-uniform distribution of compressive stress was due to friction of the loading plate, the test specimen was compressed between two cones whose generator lines made an angle with the plane of compression equal to the soil-loading plate friction angle. As shown in Figure 33b the cone angle induces outward slipping of the soil to maintain a more uniform specimen diameter. A net soil displacement nearly parallel to the loading head movement combined with the effect of St. Venant's principle results in a more rapid diffusion of stress to a pure axial compression over a greater proportion of the specimen length.

7.2 Test Procedure and Apparatus

Two types of loading were used, a cone for the cylindrical specimen and a pyramid for the square specimen as shown in Figure 34.

The pyramid test, with the application of the moire technique was used as a means to check whether the

distribution of compressive stress was uniform. Pyramid and cone angles were determined from friction tests between the soil and the loading plate material. Since it was difficult to determine accurate friction angles, due to the presence of adhesion forces, angles of 110° to 160° in 10° increments were prepared. A combination of both friction and compression tests were used to obtain optimum loading plates. Plexiglas was used for pyramids (9 x 9 cm) and cones were machined from 12.5 cm diameter polypenco nylon Mc-903 rod. Cylindrical soil specimens were 5.5 cm diameter by 18 cm and the square specimens were 6.5 cm square by 18 cm.

7.3 Results and Discussion

Modified compression test overcame the problem of bulging and produced approximately pure axial compressive stress (Figures 35 and 39a). True axial stress and natural strain relations were plotted to find the compression modulus (secant modulus) for different loading rates. An approximation method was used to determine yield stress and this was compared with existing yield criterion theory. The volume changes were measured by comparing initial radius and height of the specimen to the final radius and height after the test. Moire technique was again used to measure the axial strains and they were compared with the dial gauge measurement.

7.3.1. Stress and strain relationships

Type I and Type III soils (see section 8.2) in the different moisture contents were tested by using 110°, 120° and 130° cones. True stress was computed by using a

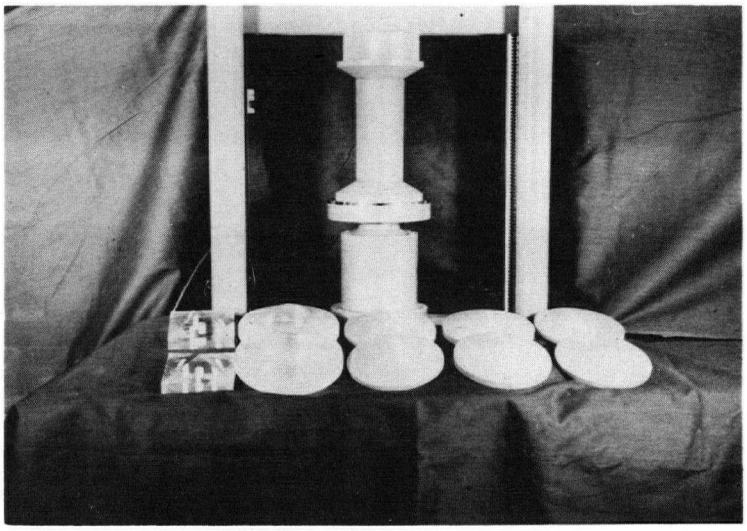

Figure 34. Cone and pyramid test apparatus.

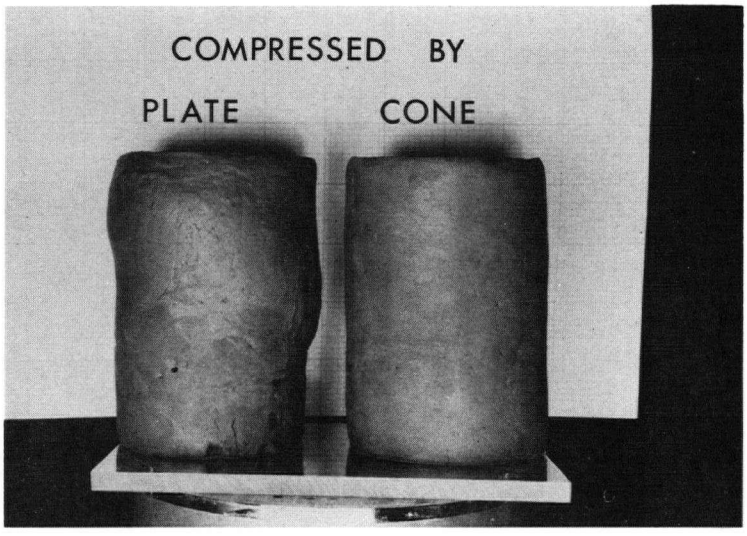

Figure 35. Loaded specimens after 12 percent deformation.

corrected cross-sectional area, which is computed from the following formula:

$$A = \frac{A_o}{1\text{-strain}}$$

where A_o = original area

A = corrected area.

The natural strains, used as axial strains, were computed by

$$\bar{\varepsilon} = \ln (1 - \varepsilon) \qquad [35]$$

where $$\varepsilon = \frac{h_o - h}{h_o} \quad . \qquad [36]$$

And when moire techniques are used,

$$\varepsilon = \frac{P}{D_Y + P} \quad .$$

When a dial gauge was used, lagrangian strain was computed from

$$\varepsilon = \frac{\Delta L}{L_o} \qquad [37]$$

where ΔL = change of specimen length as read from a dial gauge

L_o = the initial specimen length.

The 5 cm initial gauge length was marked before a test at the middle of the specimen and the change in gauge length (ΔL) was computed from the final length measured after the test. The conical loading heads which were inside of the test specimen therefore did

not affect the measurement.

Compressive stress was then evaluated from the relations:

$$\sigma = \frac{F}{A} \qquad [38]$$

where F = compressive force

and shear stress was computed from

$$\tau = \frac{\sigma}{2} \quad . \qquad [39]$$

True stress was then plotted against natural strain as shown in Figures 36 and 37. From these relationships, compression (Secant) and tangential moduli can be obtained and these moduli can be used to express stress in terms of strain in soils. True stress was again plotted against natural strain on a log-log scale, the graph was very nearly linear as shown in Figure 38. The plastic stress can be then approximated by:

$$\bar{\sigma}_p = K \varepsilon^n \qquad [40]$$

where K = the proportionality factor

ε = natural strain

n = strain hardening coefficient.

Strain hardening coefficient n and the proportionality factor K are determined from best fits to experimental data.

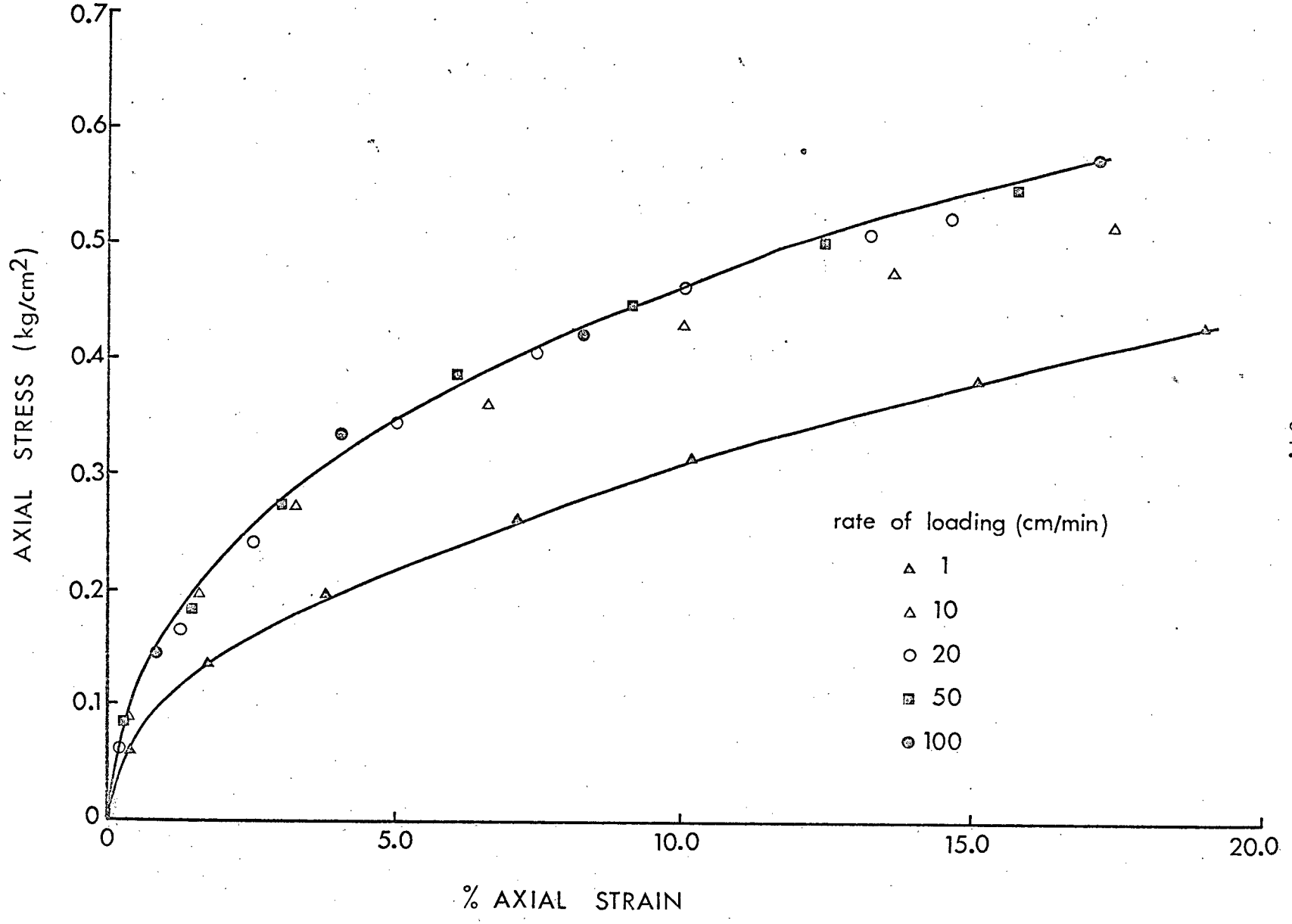

Figure 36. Stress-strain curve for unconfined compression on remolded Haney Clay Type I. MC = 11.3%. Density = 2.01 g/cm^3.

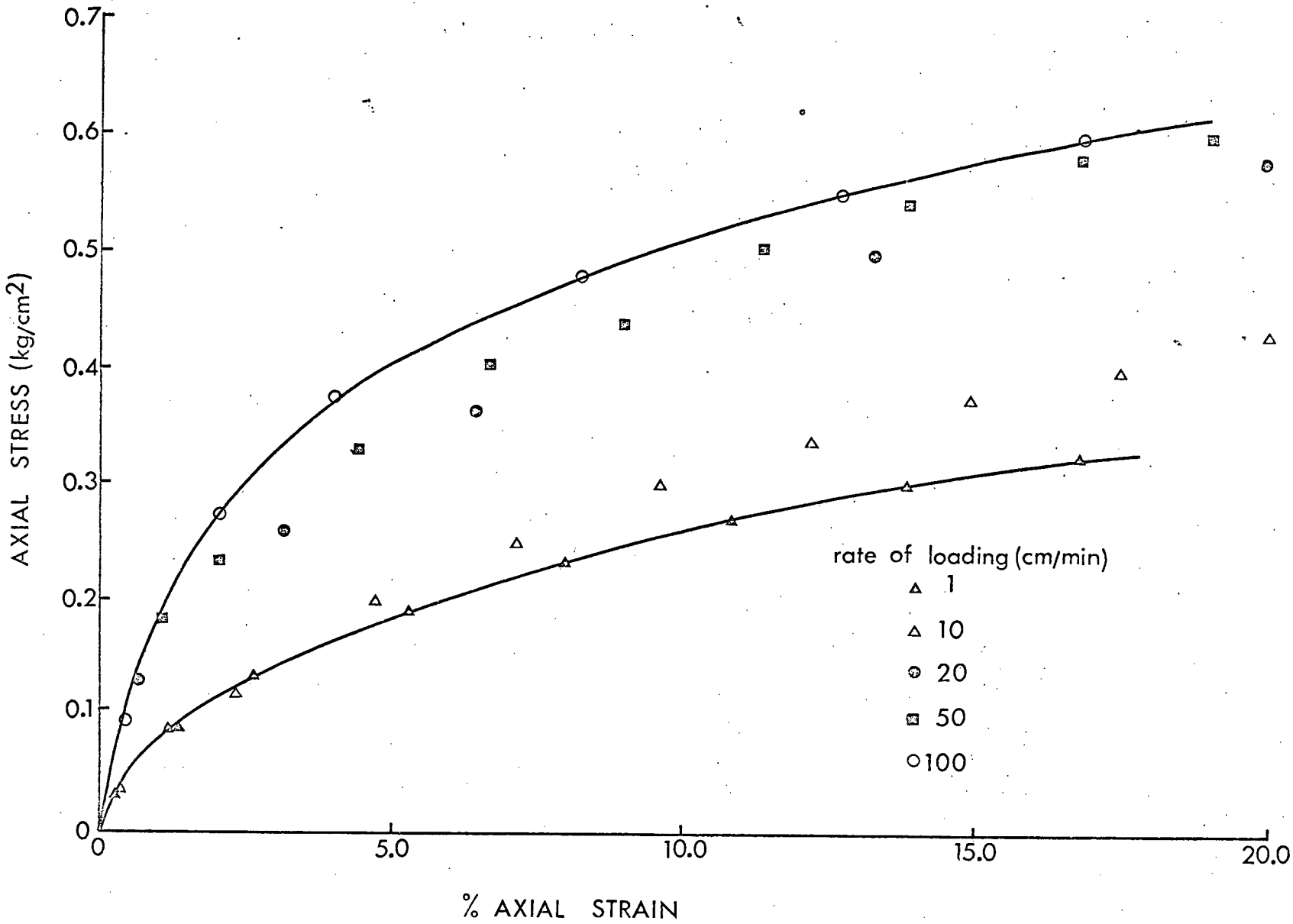

Figure 37. Stress-strain curve for unconfined compression on remolded Sandy Clay Type III. MC = 12.2%. Density = 2.28 g/cm^3.

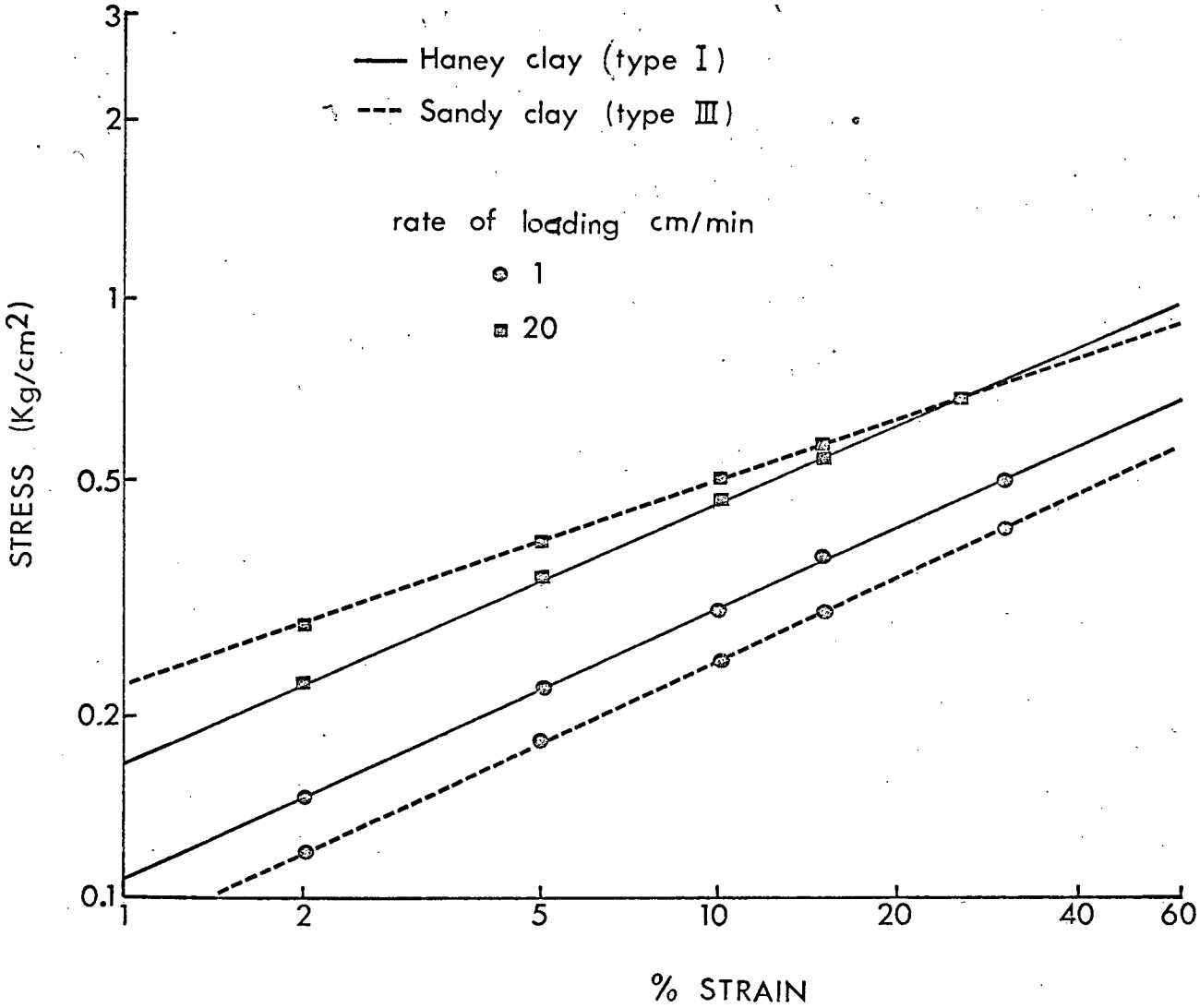

Figure 38. Log-log plot of stress-strain curve for Haney clay Type I, and sandy clay Type III. M.C. = 11.3%. Density = 2.01 g/cm^3.

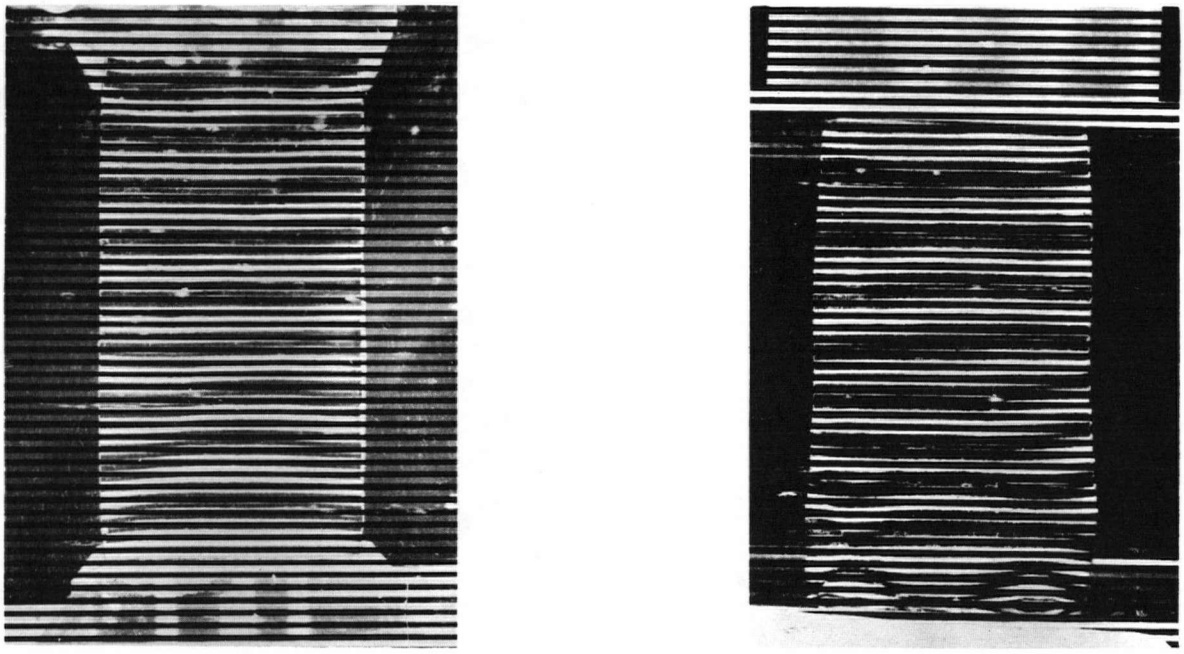

(a) (b)

Figure 39. Displacement patterns shown by moire effect for (a) pyramid loading head, (b) flat plate loading head. (Note non-uniform deformation at lower corners).

Another interesting comparison was the strain differences between the center and outer part of the specimen in flat plate compression tests. As previously discussed, lateral expansion resistance due to friction produced about 30 percent higher strain at the center than at the outer part. This difference was computed by measuring the strain on the outer part of the specimen by the moire method and the center part by a dial gauge. The moire patterns observed on the rectangular specimens, one compressed between two pyramids which was used as an improved method and the other compressed between two flat plates which has been the conventional method as shown in Figures 39a and 39b respectively.

As shown in Figure 39b, the stress concentration caused by friction obstructing lateral expansion can be observed at the bottom of the specimen, while Figure 39a shows uniform strain distribution.

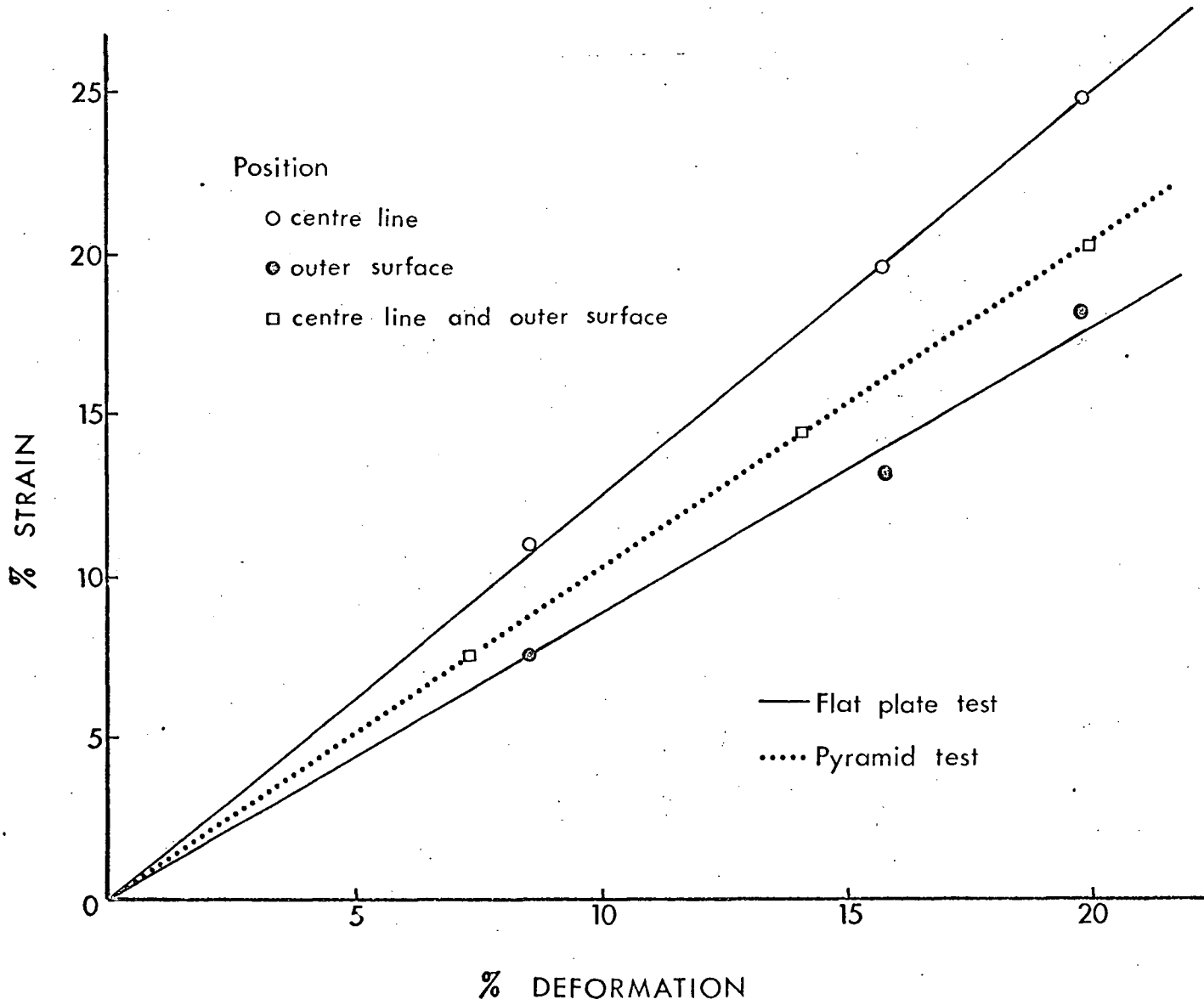

Figure 40. Strain differences between center line and outer surface of the specimen with flat plate and pyramid loading heads.

As an additional check on whether uniform and unrestricted expansion was obtained the volume changes were measured from the relation:

$$\text{Volume change} = \frac{\pi r^2 h}{\pi r^2_o h_o} \qquad [41]$$

where r and h are the radius and height respectively of the cylinder at any given time, and r_o and h_o are initial values of r and h. There was no significant volume changes in both types of soil when cones were used as compression heads, and at the rate of loading between 1 and 100 cm/min.

7.3.2. Yield stress in cohesive soil

The concept of "yield" in soils, particularly in cohesive soil is very difficult to define when the material does not have a linear stress-strain curve as occurs in some very ductile metals. The definition of yielding as the upper limit of elasticity therefore loses its meaning. Such non-linear stress-strain curves are characteristic of soils. In addition, in cohesive soils where physical properties control soil behavior, the stress-strain curves are also rate dependent. The work by Casagrande and Wilson (8) and Geuze (20) indicates the influence of creep effects on yield or failure of cohesive soil. Thus "yield" of a cohesive soil cannot be rigorously defined. Approximations may be worked out if accurate stress and strain relationships are established and rate effects are considered.

A further approximation made was the fitting of a straight line to the strain hardening portion of the stress-strain curve. This assumes that the yield surface will continue to expand with the stress and strain history but will retain the original shape. The elastic strain which is very small compared to the total strain was neglected and the material was regarded as incompressible. The straight line in Figure 41 is the corresponding stress-strain curve

used in this approximation method. The yield stress was then determined from the stress-strain curve obtained by the improved compression test-cone method.

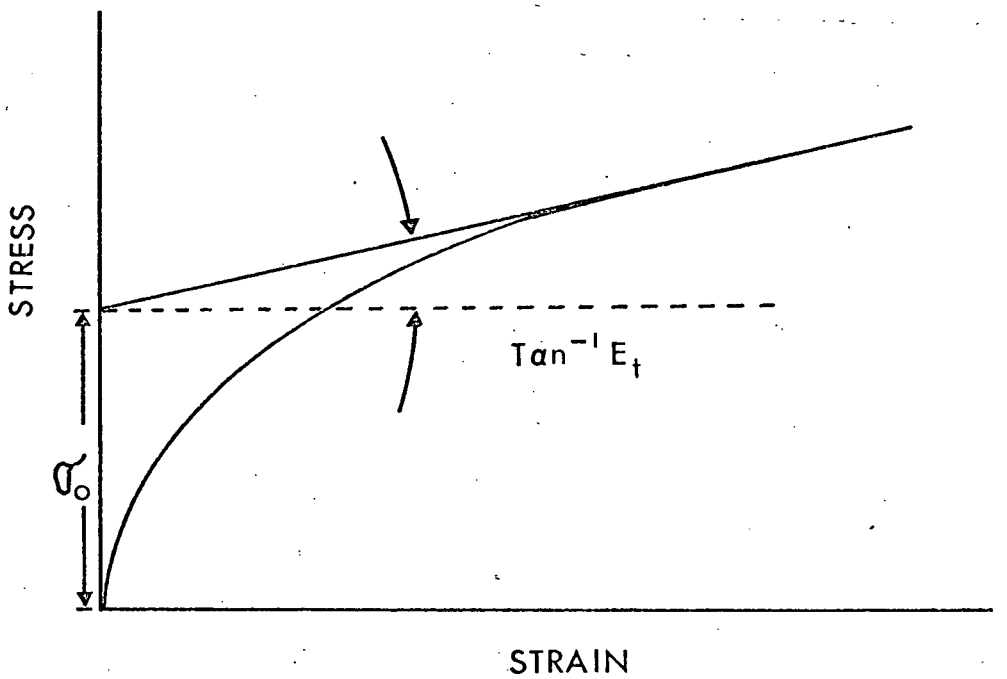

Figure 41. Approximated yield stress determined from the stress-strain curve.

To check the yield stress obtained from the described approximation method, yield stress was evaluated again from the maximum shear stress theory. Cohesive soils with a high moisture content flow like a ductile metal and the slip-line which appears at the onset of plastic flow is inclined at an angle of 45-50° with respect to the direction of the principal stresses during uniaxial compression.

The theory can be described as:

$$\tau_{max} = \frac{\sigma_1 - \sigma_3}{2} = \text{constant} \qquad [44]$$

and in uniaxial compression,

$$\sigma_1 = {}_2 = 0, \quad \sigma_3 = -\sigma_3$$

thus

$$\tau_{max} = -\frac{\sigma_o}{2} \quad .$$

Hence the yield condition requires that

$$\tau_{max} = \frac{1}{2}(\sigma_1 - \sigma_3) = \frac{\sigma_o}{2} \quad . \qquad [45]$$

The difference between values measured by the approximation method and computed by yield theory was generally less than 10 percent. The values obtained from the approximation method were used later in 10.1.3. for the analysis of practical design applications.

7.3.3. Stress-strain relationship and compression modulus by rate effect

As shown in Figure 42 and 43, the compression modulus decreased with decrease in loading rate in both

Type I and III soils. In other words, shear resistance increased with increased loading rate. These results again confirm the rate dependent characteristic of this Type I clay soil as observed in the stress wave test. However, on this particular soil, rate dependence became almost insignificant for rates of loading between 10 - 100 cm/min. From these results it is apparent that as long as the model soil machine travels between 10 - 100 cm/min., the velocity effect does not affect prediction equations of prototype machines in this soil. The approximate yield stress (Figure 41) at the 10 cm/min. loading rate was almost twice that of the 1 cm/min. (Figure 36). As shown in Figures 42 and 43 compression modulus decreased more than 70 percent below the 5 percent strain level and was essentially constant thereafter.

7.3.4. Application of slip plane theory

In a two dimensional element of soil stressed to failure under principal stress σ_1 and σ_3, failure occurs along a "slip plane" inclined at an angle α with the major principal plane. The well known Mohr-Coulomb failure criterion can be used to determine α as shown in Figure 45. The failure criterion is

$$s = C + \sigma \tan \phi \qquad [46]$$

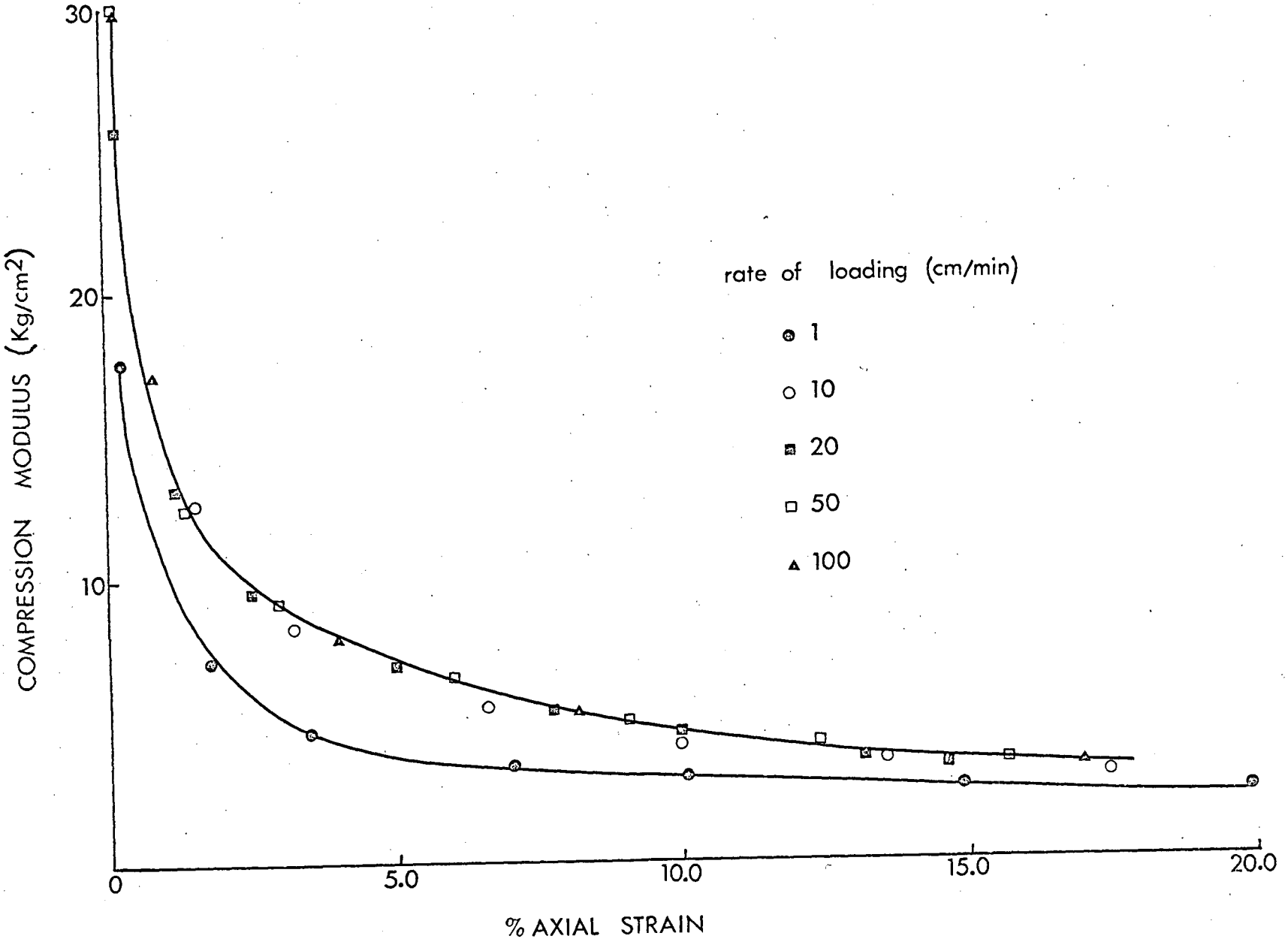

Figure 42. Compression modulus versus axial strain for Haney clay Type I. M.C. = 11.3%. Density = 2.01 g/cm^3.

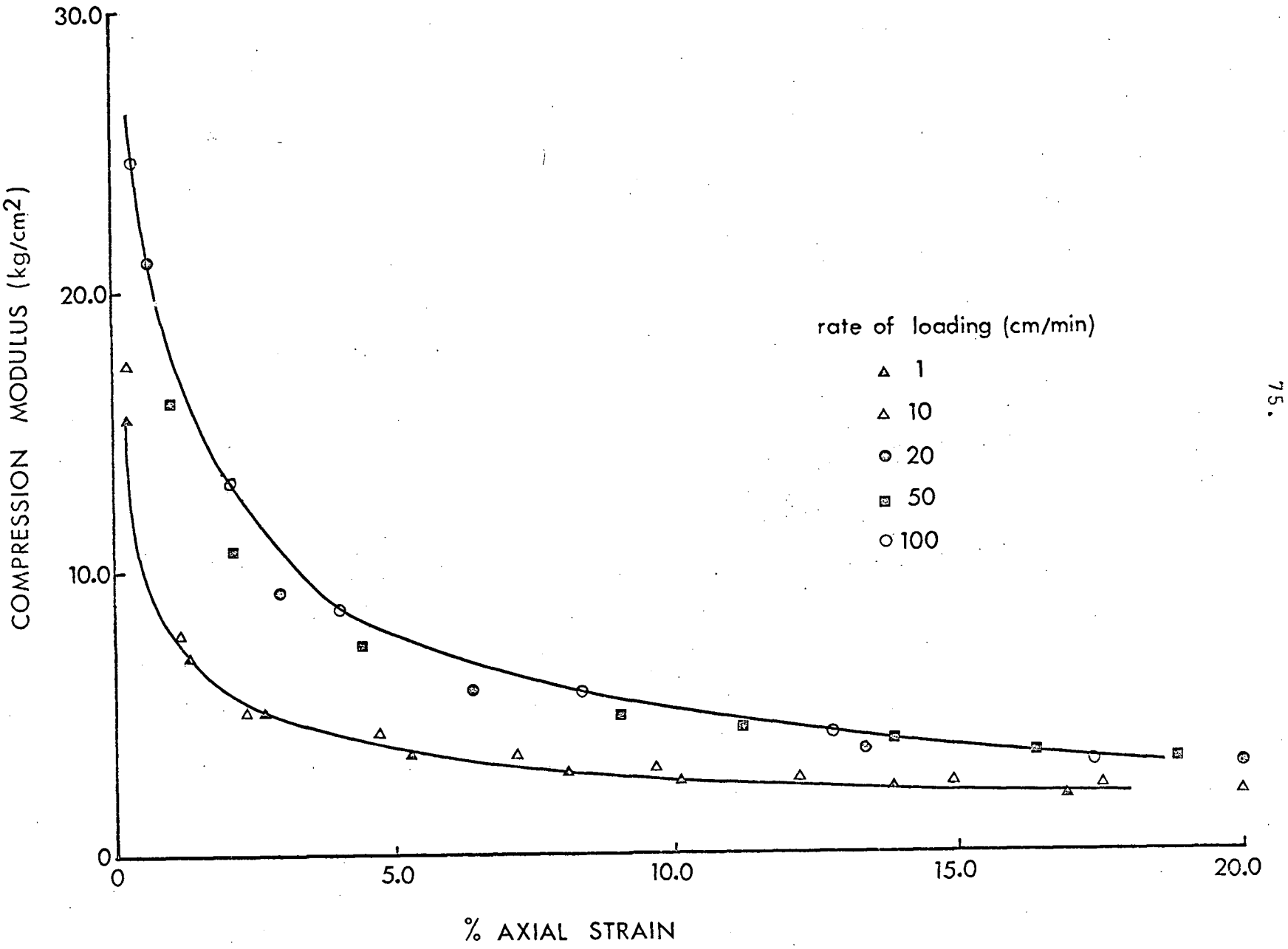

Figure 43. Compression modulus versus axial strain for sandy clay Type III. M.C. = 11.3%. Density = 2.28 g/cm^3.

where s = shear strength

C = cohesion

σ = normal stress

ϕ = angle of internal friction

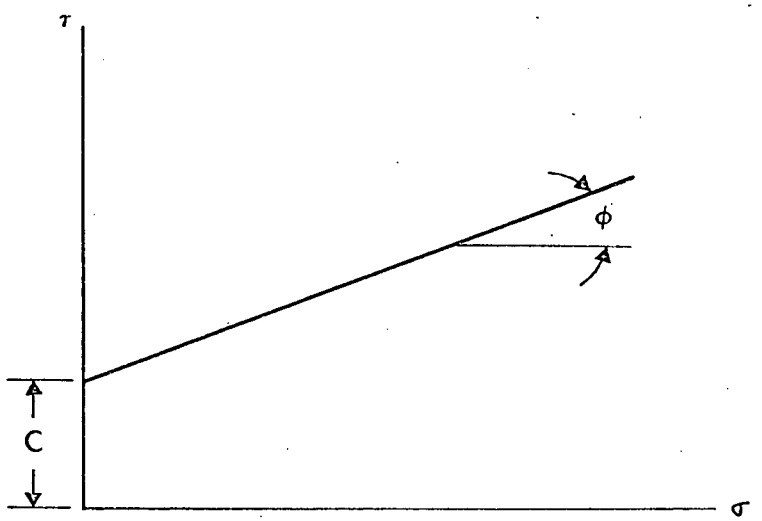

Figure 44. Failure envelopes.

The normal and shear stresses (σ and τ) on the failure surface are given by

$$\sigma = \frac{\sigma_1 + \sigma_3}{2} + \frac{\sigma_1 - \sigma_3}{2} \cos 2\alpha \qquad [47]$$

$$\tau = \frac{\sigma_1 - \sigma_3}{2} \sin 2\alpha \, . \qquad [48]$$

At failure the shear stress τ on the failure surface must be equal to the shear strength s. Substituting equation [47] and [48] in [46] and setting

$$s = \tau$$

$$(\frac{\sigma_1 - \sigma_3}{2}) \sin 2\alpha = c + (\frac{\sigma_1 + \sigma_3}{2} + \frac{\sigma_1 - \sigma_3}{2} \cos 2\alpha) \tan \phi \qquad [49]$$

By application of trigonometric relations, equation [49] may than be transformed into:

$$\sigma_1 = \sigma_3 + \frac{c + \sigma_3 \tan \phi}{\sin \alpha \cos \alpha - \cos 2\alpha \tan \phi} \, . \qquad [50]$$

Wu (67) gives a solution for obtaining the angle α which produces a failure plane for minimum values of σ_1 for given values of σ_3 by differentiating the denominator of equation [50].

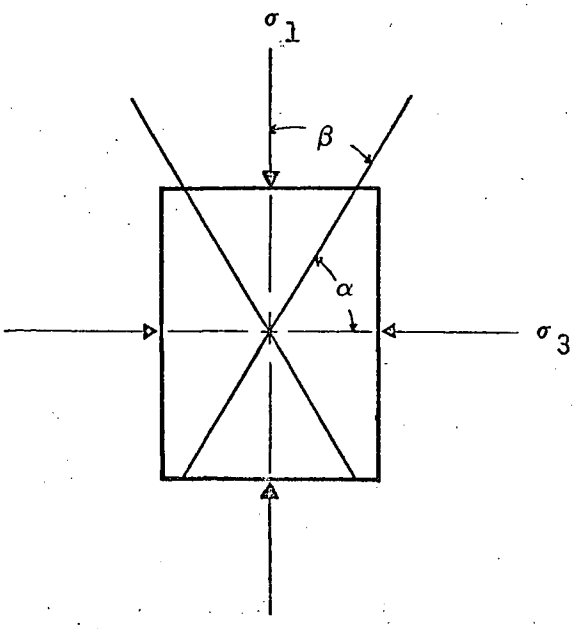

Figure 45. Failure plane.

The angle α can then be obtained from the relation

$$\alpha = 45° + \frac{\phi}{2} \quad . \qquad [51]$$

In uniaxial compression σ_3 becomes zero and equation [50] then reduces to the solution:

$$\sigma_1 = \frac{c}{\sin \alpha \cos \alpha - \cos 2 \alpha \tan \phi} \quad . \qquad [52]$$

Since the denominator of equations [50] and [52] are the same the slip plane angle can still be obtained as:

$$\alpha = 45° + \frac{\phi}{2} \quad .$$

Substituting $\alpha = 45° + \frac{\phi}{2}$ into equation [52] yields

$$\sigma_1 = \frac{2\,c}{\cos \phi - \sin \phi \tan \phi - \tan \phi} \, .$$

From equation [48], shear stress becomes

$$\tau = \sigma_1 \sin \alpha \cos \alpha \qquad [53]$$

when $\sigma_3 = 0$.

As α varies between 45° to 50°, sin α cos α approaches 0.5 and hence

$$\tau = \frac{\sigma_1}{2} \qquad [54]$$

which justifies equation [39] for computing shear stress.

The stress σ_1 obtained from the compression test and that computed from equation [53] were compared and found to be in good agreement (less than 5% difference).

8. DYNAMIC RESPONSE OF SOIL

Part of the energy applied in deforming a clay type soil is elastically stored and part is dissipated, therefore on an individual data point-by-point basis it is reasonable to consider soil response as viscoelastic.

Young's modulus for an elastic solid can be evaluated by measuring the velocity of a stress wave in the solid and using the relation

$$E = \rho C^2 \qquad [55]$$

where E = Young's modulus

ρ = soil density

C = velocity of stress wave.

The attenuation constant $\alpha(\omega)$ and phase velocity $C(\omega)$ in a viscoelastic medium are derived and they are, respectively

$$\frac{\alpha C}{\omega} = \frac{\sin \theta}{1 + \cos \theta} \qquad [56]$$

$$C = |E|/\rho^{1/2} \ \mathrm{SEC}\ (\theta/2) \qquad [57]$$

where α = attentuation constant

θ = phase angle

$|E|$ = complex modulus

ρ = density of medium

ω = frequency

C = stress wave velocity.

Details of the derivation are given in the appendix.

Equations [56] and [57] express linear viscoelastic wave propagation response where parameters |E| and θ are functions of ω and t but not of stress level.

Hunter (27) derived viscoelastic stress and strain formulae for simplified approximations by assuming that α and C are constant.

$$\sigma\ (x,\ t) = -\ \rho C V e^{-B(t\ -\ x/c)}\ -\ \alpha x \qquad [58]$$

$$\varepsilon\ (x,\ t) = -\ \frac{V}{1\ +\ \gamma}\ \left\{\frac{\alpha}{C} + \frac{\alpha}{\beta}\right\} + \alpha\ \gamma\ \{t\ -\ x/c\}$$

$$+\ \{C^{-1}\ -\ \alpha/\beta\}e^{-\beta(t-x/c)}\ \ e^{-\alpha x} \qquad [59]$$

where σ = stress

ε = strain

V = velocity of mass m at time of impact

m = mass

t = time

x = distance from the impacted end

A = area of specimen cross section

β = α C + (ρ C A/m)

γ = α m/ρ A

and other terms are as previously defined.

Both equations reduce to the corresponding solutions for an elastic solid as α → 0. Kondner (32) and others found that θ varies from approximately 10 degrees to less than one degree. Therefore, at the wave front x = ct and Hunter's equations reduce to:

$$\sigma = -\rho C V, \qquad [60]$$

$$\varepsilon = -\frac{V}{C} \text{ and} \qquad [61]$$

$$E = \rho C^2 . \qquad [62]$$

These solutions are identical to those for an elastic solid. This approximation may be used for soil, such as clay, where the phase angle is very small.

8.1 Procedure and Apparatus

Stress wave propagation was observed and measured in Haney clay and sandy clay soils with different moisture contents and densities. For the comparison between stress wave and vibration methods, the same specimens were used for both tests. Stress wave measurements were conducted immediately after vibration tests so that changes in moisture content and other physical properties were minimized.

Different sizes of rectangular and cylindrical specimens (Table I) were loaded on one end with a pendulum. A striking steel ball suspended with thin cotton cord was released with an electromagnet to produce the stress wave. The wave amplitude is controlled by varying the drop height and mass of the ball. Before impact the ball is held in position by a D.C. electromagnet, which was attached to the bottom of a rigid pendulum. The rod of the pendulum was held in position by a bracket connected to the pendulum framework. The pendulum rod holder and bracket was adjustable, thus allowing the ball to be positioned

accurately at a specific height.

The struck end of the soil specimen was covered by an aluminum plate to provide uniform pressure across the area. The specimen was suspended either by tapes or rested on foam rubber. However, it was found that after each impact, the point where the ball struck changed, due to permanent strain produced in the test specimen. The specimen position was checked after each impact and adjusted to maintain a fixed reference point.

A Tektronix 502A dual beam oscilloscope and Polaroid camera attachment was used as a recording device. Time exposures were taken of the beam traces. An external triggering circuit activated by contact between the steel ball and the aluminum cover plate was used to obtain a single horizontal sweep of the two oscilloscope beams. The accelerometers were connected to the oscilloscope through preamplifiers. The triggering circuit is shown in Figure 46.

In order to investigate whether an embedded accelerometer gauge in a specimen affects stress wave velocity a single gauge was used to pick up the final stress wave which had travelled along the specimen. The first pulse was generated by contact between the steel ball and the aluminum cover plate to produce a 12 volt pulse as a reference point. The very short period for stress wave propagation through the cover plate was neglected. Typical

pulse-time records are given in Figure 49.

Although the stress wave velocity in the test soil (30 m.p.s. to 300 m.p.s.) is much lower than in metal, a full sweep time of the oscilloscope in the order of 1 - 2 milli-seconds was used in order to avoid reproducing reflected waves on the oscilloscope screen.

Stresses were also measured by using Kistler Quartz Pressure Transducer, Model 606A, embedded in the specimen. The pressure gauges were calibrated with the electronic circuit of the Kistler charge-amplifier.

Specimens of Type I and Type III soils, 4.5 cm diameter by 85 cm long, were specially prepared for this test as shown in Figure 48. Density and moisture of Type I and Type III soils were 2.08 grams/cm^3 and 14.8% and 2.29 grams/cm^3 and 12.1% respectively. Pairs of pressure gauges were in turn positioned at 19 and 29, 29 and 39, 39 and 49, 49 and 59 cm from the impacted end. The first gauge position at 19 cm from the impacted end was chosen to have the best response and to simulate conditions in an infinite medium, following the suggestion by Durelli and Riley (17) that length to diameter ratio should be at least 4 to satisfy the above conditions. The major portion of the incident wave passed the last gauge position before the reflected wave arrived.

The intensity of impact loading was varied from that of stress wave propagation velocity measurements to

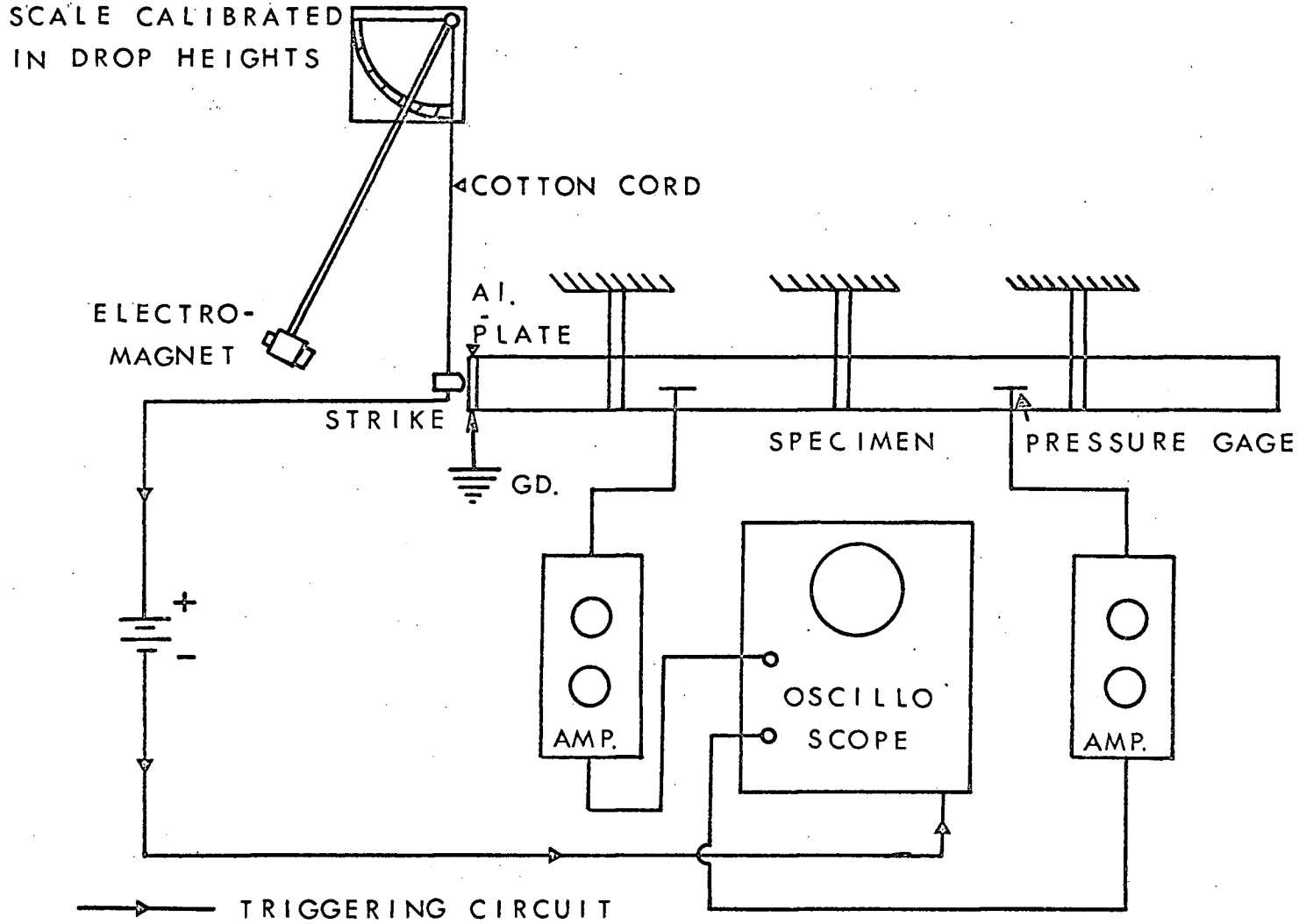

Figure 46. Schematic diagram of experimental apparatus for stress wave measurement.

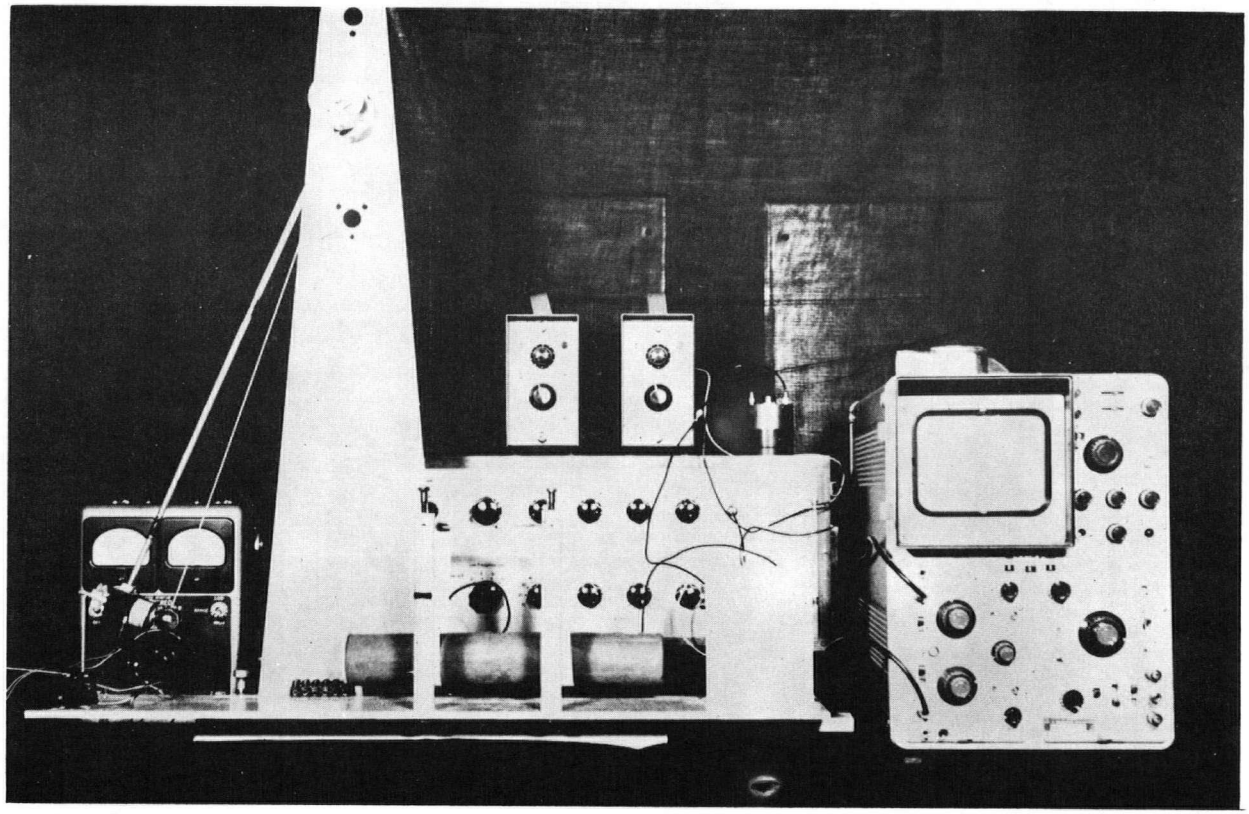

Figure 47. Equipment for stress wave measurement.

that of compressive stress measurements as well as from test to test. Low intensity loading was used at the beginning of a series of tests and higher intensity loadings at the end of the series.

When all tests were completed, measurements were made of sample density and moisture content at three locations along the length of the specimen.

8.2 Soil Specimen Preparation

The same mixing method as described in section 6.5.2. was again used for this experiment as well as for a forced vibration method to be described later. Different sizes and shapes of specimens were prepared by trimming in a procedure similar to that used for triaxial specimen preparation.

Type I and Type II soils were again used and one more Type III soil was added for this experiment. The Type III soil:

	Clay	Silt	Sand
Type III	20%	18%	62%

Density and moisture content were varied for different tests and are reported with the test results.

8.3 Results and Discussion

Stress wave propagation velocities were measured for different moisture contents and densities. Cylindrical and rectangular test specimens were used and their dimensions are given in Table 1. Soil composition was also

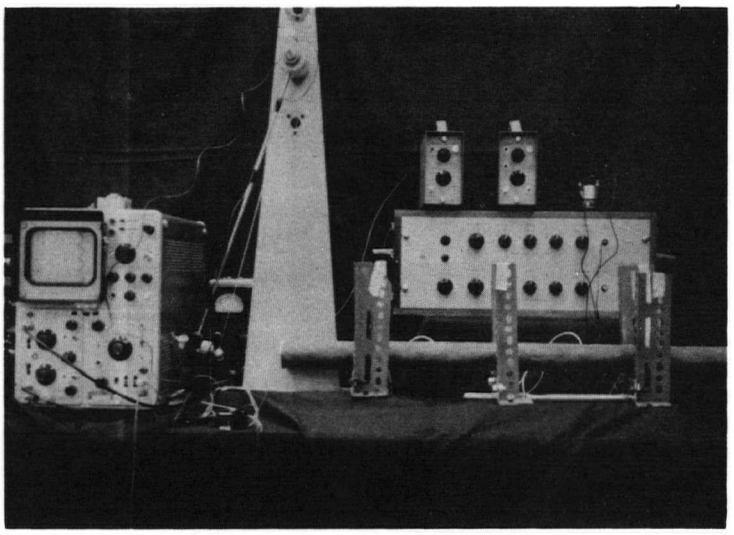

Figure 48. Instrumentation for stress measurement.

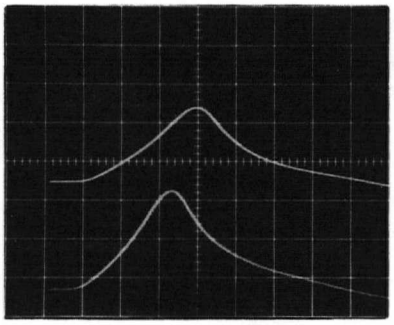

Upper position = 29 cm
Lower position = 19 cm

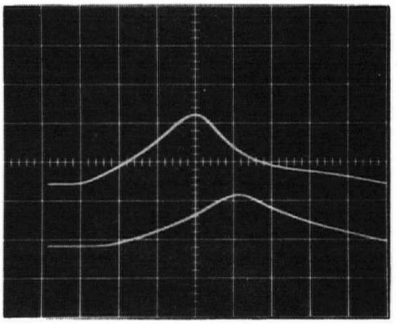

Upper position = 29 cm
Lower position = 39 cm

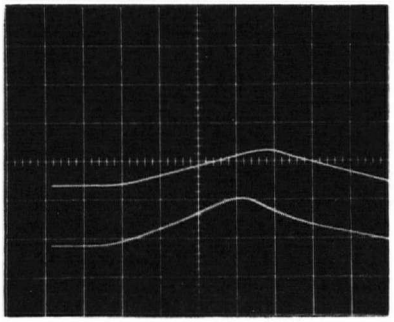

Upper position = 49 cm
Lower position = 39 cm

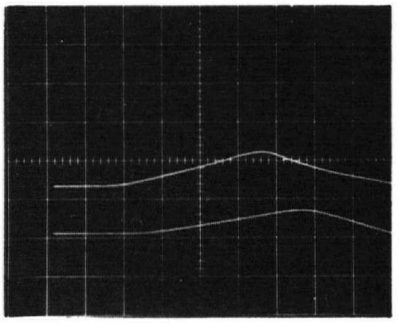

Upper position = 49 cm
Lower position = 59 cm

Vertical scale → 1 cm = 0.146 Kg/cm^3

Figure 49. Typical pressure gauge records on Haney clay.

varied by increasing the sand content in a high clay content soil. The propagation velocity of the different stress levels of the wave front was calculated by plotting the constant stress levels observed at different positions along the rod in the x - t plane to investigate rate dependency or independency of soil. Stress waves are shown in Figure 49 and the constant stress level plots are given in Figure 50.

8.3.1. Rate dependency of soil

It has been observed that soil response to applied load is time dependent and therefore modified Kelvin and Maxwell models were used by Murayama (39), Christensen and Wu (9) and Vey and Strauss (65). The methods used by these researchers have been mostly carried out by static or quasi-static loading conditions. It is therefore necessary to investigate whether soil obeys rate dependent theory under dynamic loading. The stress wave induced by impact of an 81.2 gram steel ball released from a height of 25 cm was recorded on the oscilloscope as shown in Figure 49 and the resulting stress-time record was analyzed.

Considerable stress attenuation took place as distance increased from the impacted end. Stress attenuation as a function of distance from the loaded end of the specimen in Type I and Type III soils are shown in Figure 51.

Constant stress levels induced by impact load were plotted in the x - t plane to investigate whether the soil was stress-rate (or strain-rate) dependent. This was accomplished by plotting the time t which had elapsed from initial impact until stress rose to a given level at a distance x from the impact point. According to the strain-rate independent theory, each strain increment must propagate with a constant velocity. If the material obeys the rate independent theory, any constant stress level plotted in the x - t plane must lie along a straight line while the stress level plotted in the x - t plane should lie along curved lines if the material exhibits any rate dependence.

It was concluded that the soil used was a rate dependent material as constant stress levels plotted in the x - t plane lay along curved lines as shown in Figure 50. The rate dependency observed during the quasi-static compression test, as shown in Figures 36 and 37, was verified by this stress wave technique.

8.3.2. Soil strength and physical properties vs. propagation velocity

Propagation velocities were measured for different moisture contents and densities. The least square method was used to draw the line of best fit for propagation velocity as a function of bulk density for each moisture content. From the data shown in Figure

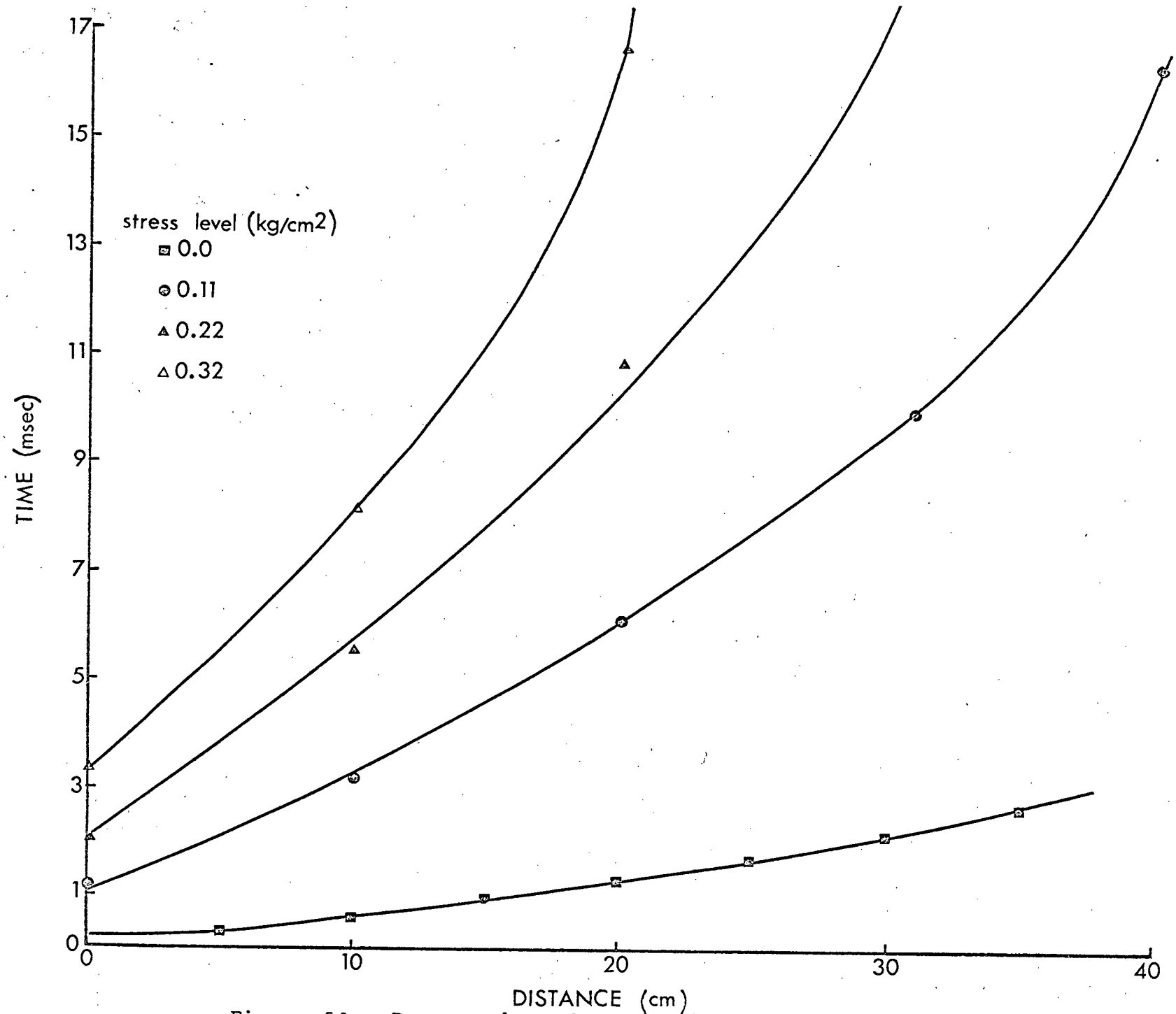

Figure 50. Propagation of stress increments in the x - t plane for Haney clay Type I.

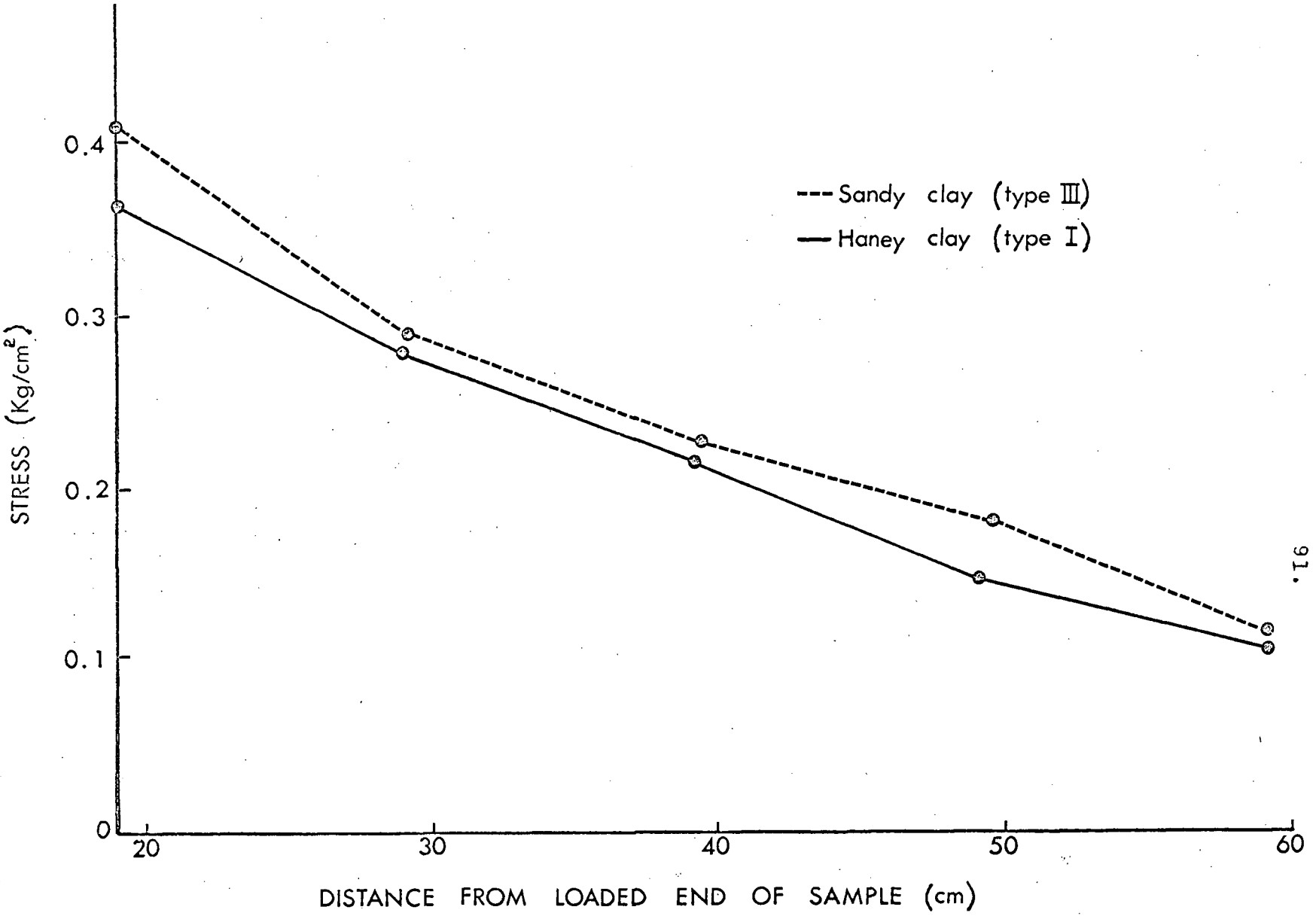

Figure 51. Stress attenuation as a function of distance from the loaded end of the specimen.

54 it can be seen that there was a noticeable increase in wave velocity with increased soil density while wave velocity decreased with increased soil moisture content. However, as moisture content increased the slope of propagation velocity increment was decreased compared with lower moisture contents.

Three different steel balls weighing 53, 81.2 and 155 grams were used. Each ball was released from heights of 10 cm, 20 cm and 30 cm. The height of ball and drop did not affect propagation velocity. It was therefore concluded that propagation velocity was independent of impact force and impact rate within the range of forces and rates used. This conclusion must be limited to the investigated range of moisture contents from 12.6 to 19.8 percent and bulk density range from 1.7 to 2.37 grams per cubic centimeters.

The stress wave velocity measurement obtained from the single gauge and the 12V D.C. reference pulse was compared with velocity measurements obtained by using two embedded accelerometer gauges. There was no noticeable difference in velocity by the two methods. Therefore the small (1 cm diameter x 1.5 cm long) accelerometer embedded in the specimen did not affect the propagation velocity in the soil. Typical records of reference pulse and stress wave position are shown in Figures 52 and 53.

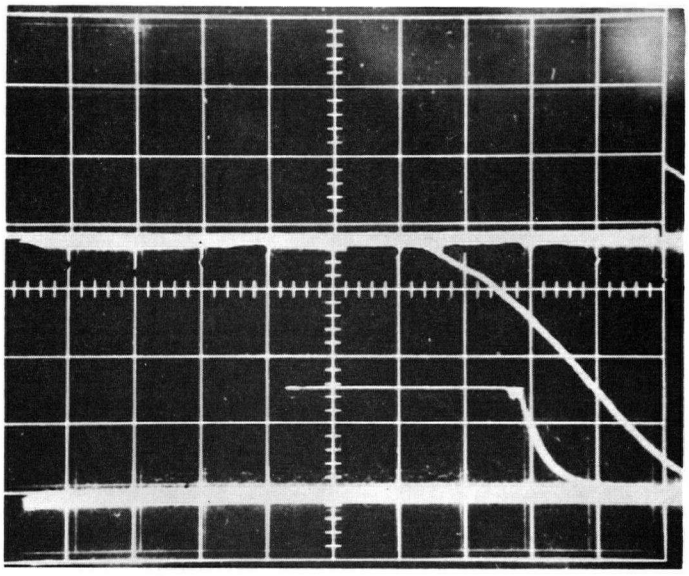

Figure 52. D.C. and wave pulses response in Type I soil.

Density = 1.98 grams/cm^3. M.C. = 13.3%.
Horizontal scale: 1 Div. = .2 m. sec.

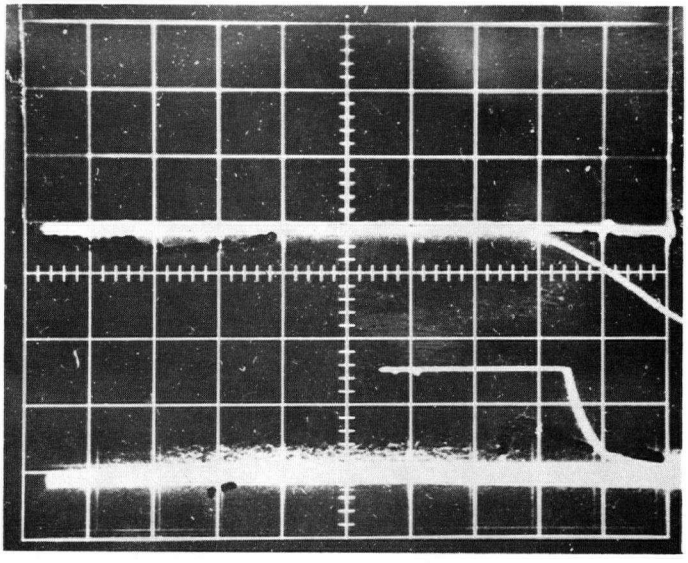

Figure 53. D.C. and wave pulses response in Type III soil.

Density - 2.3 grams/cm^3. M.C. = 12.8%.
Horizontal scale: 1 Div. = 1 m. sec.

Young's modulus computed from propagation velocity is shown in Table I. The values of E are as much as 75 percent greater than those evaluated from forced vibration tests on the same soil. There did not appear to be any significant effect from the shape of specimen, or any effect from the mounting method used (suspension or resting on foam rubber). No consistent relationship between propagation velocity and Young's modulus was found. For example, propagation velocity increased together with soil density as sand content of the clay soil was increased. The result was a calculated increase in Young's modulus while the mechanical strength of soil was reduced. This was probably due to a high dependence of the stress wave velocity to soil particle size. Hence this technique would not be suitable for measuring mechanical properties of soils, particularly when the soil consists of a wide range of particle sizes.

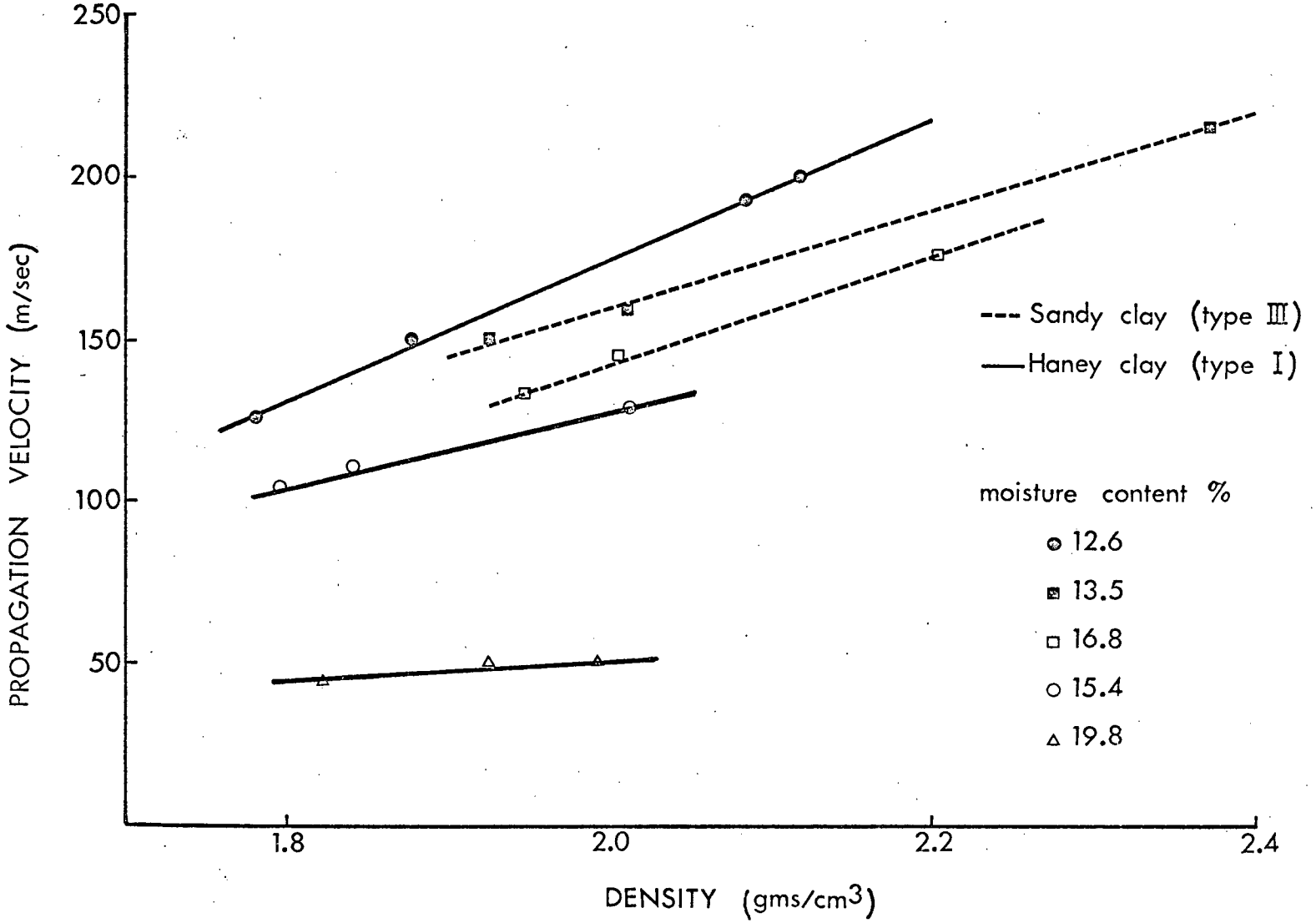

Figure 54. Stress wave propagation velocity versus density for different moisture contents.

TABLE I. Properties and Dimensions of Soil Tested and Its Results.

No.	Soil Type	Shape of Specimen	Density gr/cm^3	Dimensions cm	Water Content %	Modulus of Elasticity Kg/cm^2 X 100				Poisson's Ratio		Stress Wave Velocity m/sec.
						E_l	E_f	E_{sw}	G	μ_l	μ_f	
TYPE I	HANEY CLAY	□	2.1	4.5x3.6x18	12.1	6.5	7.06	8.23	2.35	0.38	0.5	196.1
		○	2.1	5(Dia.)x14.5	12.1	5.85	5.80	8.65	1.80	0.62	0.61	201.0
	CLAY	□	1.98	4.5x3.6x18	13.3	4.69	5.39	7.10	1.69	0.39	0.59	188.2
		○	2.01	5(Dia.)x14.5	13.0	4.23	4.68	7.37	1.59	0.33	0.47	191.0
TYPE III	SANDY CLAY	□	2.38	4.5x3.6x18.2	12.8	5.52	5.77	11.62	1.88	0.47	0.53	221.0
		○	2.38	5(Dia.)x14.5	12.8	5.36	5.42	12.07	1.95	0.38	0.39	225.2
TYPE I	HANEY CLAY	○	1.81	5(Dia.)x33	20.3			0.42				49.0
TYPE II	SANDY CLAY	○	1.97	5(Dia.)x33	16.7	1.8		2.04				101.6
		○	2.19	5(Dia.)x33	15.8	3.8		4.25				138.1

E_l : Modulus of elasticity computed from longitudinal resonance frequencies.
E_f : Modulus of elasticity computed from flexural resonance frequencies.
E_{sw} : Modulus of elasticity computed from stress wave velocity.
G : Modulus of rigidity computed from torsional resonance frequencies.

9. DETERMINATION OF ELASTIC MODULI

9.1 Procedure and Apparatus

The main function of equipment used in the forced vibration method, is to excite and detect resonance in the soil specimen and measure the frequency of this resonance. This was accomplished by using the equipment shown in Figures 55 and 56 and illustrated in Figure 57.

The output of the audio oscillator is amplified and then fed to the horn driver, the mechanical energy of which is transmitted through air to the soil specimen. When the oscillator frequency was scanned, it eventually reached one of the mechanical resonance frequencies of the soil specimen. The predominant characteristic of the specimen in resonance was the large increase in the amplitude of its vibrations when excited at its mechanical resonance frequencies. This varying amplitude was detected by a Bruel and Kjaer accelerometer type 4336, in contact with the specimen. The accelerometer output was amplified and fed to the cathode ray oscilloscope. A frequency counter connected to the oscillator was used to determine the resonance frequency more accurately than by reading the oscillator scale itself.

9.1.1. Longitudinal and torsional resonance frequency measurements

The specimen was supported on thick foam rubber pads at the nodal point. The diagrammatic sketch for

this method is given in Figure 57a. The soil specimen was vibrating freely when the supporting pad was sufficiently thick and spongy (10 cm for a 1.5 kilograms specimen). The resulting vibrations of the specimens were detected with a crystal pick-up which lightly touched the specimen. This method not only simplified testing procedures for soil but also eliminated undesirable inertia of the specimen and pick-up accessories which could change the specimen's resonance frequency. The torsional resonance frequencies, fundamental and overtones, were measured by transmitting mechanical energy to the opposite side from the crystal pick-up attachment as shown in Figure 57b. This method is sometimes confused with the output of flexural resonance frequency. The first overtone of torsional resonance and the fundamental resonance frequency of flexure were then distinguished by noting whether the response on the oscilliscope continued or died out as the attached points of the vibrator and pick-up were moved from the ends toward the center along the long axis of the specimen. Thus, the response of the specimen is noticeably reduced for a torsional mode but will continue for the flexural mode. This method also locates the nodal points along the long axis of the specimen.

9.1.2. Flexural resonance frequency measurement

Flexural resonance frequency was easily measured by resting the specimen on thick sponge rubber at the two nodal points as shown in Figure 57c. Mechanical energy was transmitted by the horn driver which was placed at the bottom of the specimen and between the foam rubber supports. In this way the problem of the confusion with torsional resonance frequency was eliminated. The remaining measuring devices are the same as used in the other resonance frequency measurements.

9.1.3. Poisson's ratio measurement

It is necessary to compute Poisson's ratio first to use the correction factors for determination of other elastic moduli. An approximate Poisson's ratio may be computed directly from the fundamental resonance frequencies of the cylindrical specimen as

$$\mu = \frac{1}{2}\left(\frac{f_e}{f_t}\right)^2 - 1 \qquad [63]$$

where f_e = fundamental longitudinal resonance frequency

f_t = fundamental torsional resonance frequency.

Young's modulus (E_1 or E_f) and shear modulus (G) were then computed. Poisson's ratio for the rectangular specimen may be more accurately computed from the

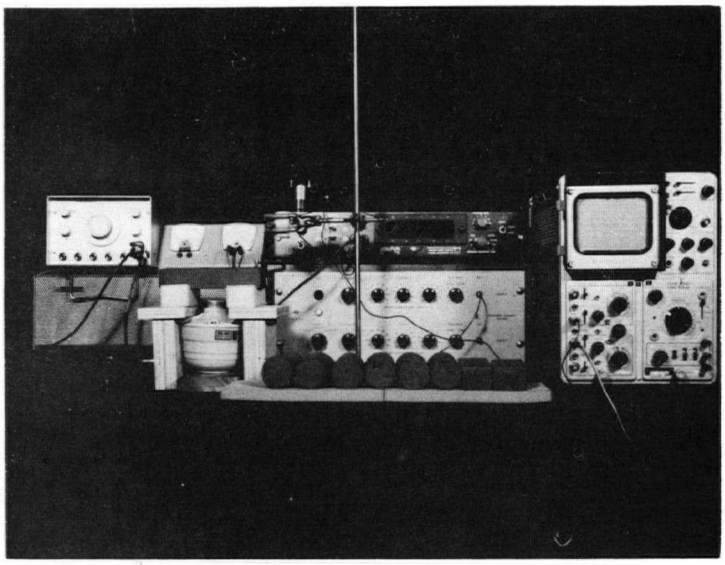

Figure 55. Electronic equipment for the measurement of torsional and flexural resonance frequencies.

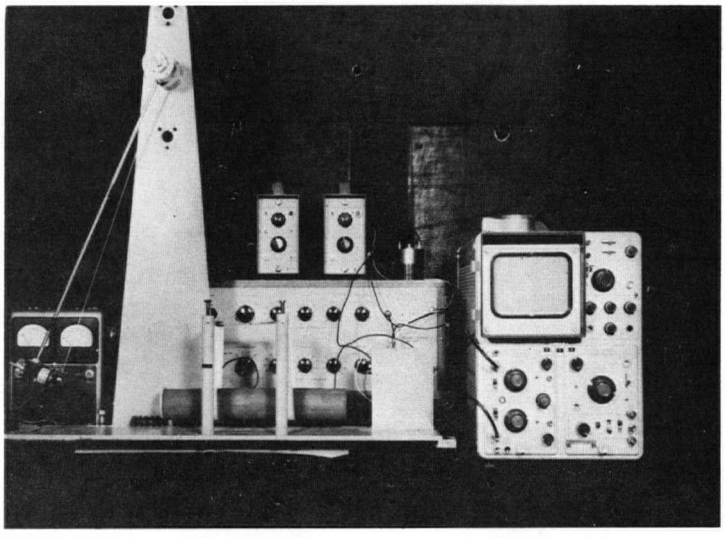

Figure 56. Apparatus for the longitudinal resonance frequencies.

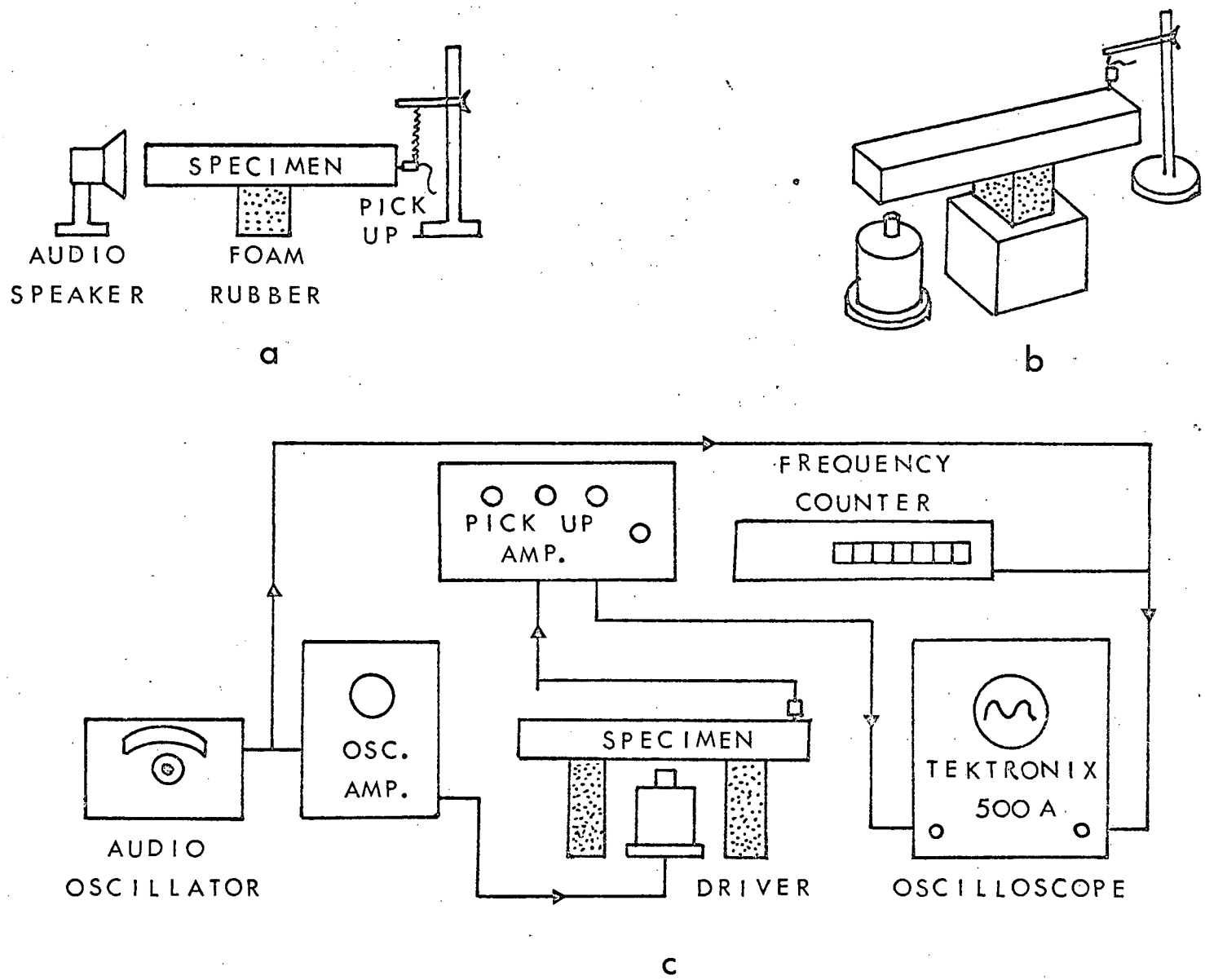

Figure 57. Sketch of equipment used for dynamic resonance measurement.

relationship

$$\mu = \frac{1}{2}\left(\frac{E_l \text{ or } E_f}{G}\right) - 1 \qquad [64]$$

where E_l = Young's modulus computed from the longitudinal resonance frequency

E_f = Young's modulus computed from the torsional resonance frequency.

9.1.4. Soil specimen

The specimens were prepared from the same Haney clay and mixtures of clay and Ottawa sand that were used for stress wave propagation tests. Most specimens used for this test were used for stress wave propagation measurements made immediately after the vibration test. The modulus obtained from the vibration test was then compared with results computed from the stress wave propagation measurement for the same soil physical condition.

Different sizes of cylindrical and rectangular specimens were tested and correction factors, due to size and shape effects as given in A.S.T.M. (60) tables were applied. Dimensions for the cylindrical and rectangular specimens are given in Table I.

9.2 Results and Discussion

Elastic data were obtained for Haney clay and sandy clay soils by the forced vibration method. The results for these soils are summarized in Table I. Both shape of the test specimen and the type of resonance

frequency (longitudinal or flexural) affected results.

Rectangular specimens produced higher moduli and higher Poisson's ratio compared to values obtained from cylindrical ones. The moduli computed from longitudinal and flexural resonance of cylindrical specimens were also more consistent than those obtained by rectangular specimens.

9.2.1. Modulus computed from the flexural resonance frequency

Young's modulus was evaluated by measuring flexural resonance frequencies of the test specimen both for cylindrical and rectangular shapes and by using the following equations:

a) Cylindrical specimen:

$$E = 1.261886 \frac{\rho s^4}{d^2} f_f^2 T_n \qquad [65]$$

b) Rectangular specimen:

$$E = 0.94642 \frac{\rho s^4}{t^2} f_f^2 T \qquad [66]$$

where E = Young's modulus

μ = Poisson's ratio

ρ = density of material

s = length of specimen

d = diameter of cylindrical specimen

t = cross-sectional dimension in the direction (or plane) of vibration (flexure of prisms only)

n = 1, 2, 3, ... = order of vibration

f_f = fundamental resonance frequency

f_n = resonance frequency of the nth node of vibration

T_n = correction factor given in A.S.T.M. Vol. 61, 1961 (pp. 1231-1233)

where $T = 1 + 6.585\,(1 + 0.0752\,\mu + 0.8109\,\mu^2)\left(\frac{t}{s}\right)^2 - 0.868\left(\frac{t}{s}\right)^4 - \frac{8.340\,(1+0.2023\,\mu+2.173\,\mu^2)\left(\frac{t}{s}\right)^4}{1+6.338\,(1+0.14081\,\mu+1.536\,\mu^2)\left(\frac{t}{s}\right)^2}$.

As shown in Table 1, the modulus obtained from the rectangular specimen was up to 17% higher than that computed from the cylindrical specimen. This was probably due to the assumptions and approximations Spinner and Tefft (60) made in computing the modulus of the rectangular specimen. As sand content increased the difference between the two shapes was decreased to less than 8 percent. This method which requires a more complicated test procedure was affected by the specimen shape as well as producing inconsistent results during the test.

9.2.2. Modulus computed from the longitudinal resonance frequency

Young's modulus was computed from the following equations for:

a) Cylindrical specimen:

$$E = \frac{\rho}{K_n}\left(\frac{2sf_n}{n}\right)^2 \qquad [67]$$

where $$K_n \approx 1 - \frac{T_1^2 n^2 \mu^2 d^2}{8s^2} \text{ if } \frac{dn}{2s} << 1 .$$

Otherwise, K_n, correction factor for the nth node of longitudinal vibration was given in A.S.T.M. (60).

b) Rectangular specimen:

Equation [67] may be used if the following equation is substituted into K_n

$$d^2 = \frac{2}{3}(a^2 + b^2) \qquad [68]$$

a and b = cross-sectional dimensions of prismatic specimens, with restriction $a < b$.

In this method the computed modulus was not influenced by the specimen shape to the same extent as it was for the flexural tests. The test procedure was simple and the results were more consistent.

9.2.3. Shear modulus computed from the torsional resonance frequency

Torsional resonance frequencies are important not only because a shear modulus can be computed but also because an accurate determination of Young's modulus requires a knowledge of Poisson's ratio which, in turn, is a function of E/G.

The theory for this type of vibration is both accurate and simple for cylindrical specimens. The cylindrical shape however introduces experimental

difficulties. Rectangular specimens on the other hand are the easiest to deal with experimentally, but the equations involved are neither as simple nor as accurate as those for cylinders. Both shapes of specimen were therefore used for this test and their results were compared as shown in Table 1. The relation of shear modulus to torsional resonance is

$$G = \left(\frac{2\ sf_n}{n}\right) R \qquad [69]$$

where R depends on the shape of the specimen.

For a cylindrical specimen R = 1 and is independent of the value of d/s the definitions of which are the same as given for equations [65] and [66]. Equation [69] is therefore exact for cylindrical specimens.

For rectangular specimen R becomes

$$R = \left[\frac{1 + \left(\frac{b}{a}\right)^2}{4 - 2.521\ \frac{a}{b}\left(1 - \frac{1.991}{e^{\pi\frac{b}{a}} + 1}\right)}\right]\left[1 + \frac{0.00851\ n^2 b^2}{s^2}\right] - 0.060\ \left(\frac{nb}{s}\right)^{3/2}\ \left(\frac{b}{a} - 1\right)^2. \qquad [70]$$

Spinner and Tefft (60) indicated however that the accuracy of equation [70] is within about 0.2 percent for b/s < 0.3 and b/a < 10 in a fundamental mode of vibration.

Shear moduli obtained from specimen shapes

showed that the results computed from the rectangular specimen gave about 8 to 20 percent higher values than those obtained from the cylindrical specimen in high clay content soil. The difference was reduced as the sand content was increased.

9.2.4. Poisson's ratio

The shear modulus was evaluated from the torsional resonance frequency measurements and Young's modulus was determined from the longitudinal resonance frequencies. Then Poisson's ratio may be computed from

$$\mu = \frac{E}{2G} - 1 \qquad [71]$$

where μ = Poisson's ratio

E = Young's modulus, and

G = shear modulus.

By successive approximation a more accurate value of μ was determined by first substituting an approximate μ into equation [64] then substituting E into equation [71].

As shown in Table I computed values for Poisson's ratio ranged however from 0.33 to 0.62, whereas values must be less than 0.5. Therefore, techniques and equipment must be improved before the method can be used for the reliable determination of Poisson's ratio.

9.2.5. Significance of elastic strains

The strains in an element of soil yielding under a force applied by a soil-machine in general would have a recoverable or elastic and a permanent strain. In practical applications the elastic strains may be neglected entirely and only permanent strains need be considered. The contribution of elastic strain to the total force required to deform a soil however requires investigation.

In accordance with one of the assumptions made, it is assumed that the components of the resultant strains are the sums of elastic and permanent components:

$$\varepsilon_x = \varepsilon'_x + \varepsilon''_x \qquad [72]$$

$$\gamma_{yz} = \gamma'_{yz} + \gamma''_{yz} \qquad [73]$$

where ε'_x = elastic strain component

ε''_x = plastic strain component

γ' = elastic shear strain

γ'' = plastic shear strain

For the components of the elastic strains it is assumed that Hooke's law is valid:

$$\varepsilon'_x = \frac{\lambda + G}{G(3\lambda + 2G)}\sigma_x - \frac{\lambda}{2G(3\lambda + 2G)}(\sigma_y + \sigma_z) \qquad [74]$$

$$\varepsilon'_y = \frac{\lambda + G}{G(3\lambda + 2G)}\sigma_y - \frac{\lambda}{2G(3\lambda + 2G)}(\sigma_z + \sigma_x) \qquad [75]$$

$$\varepsilon'_z = \frac{\lambda}{G(3\lambda + 2G)}\sigma_z - \frac{\lambda}{2G(3\lambda + 2G)}(\sigma_x + \sigma_y) \qquad [76]$$

$$\left.\begin{aligned} \gamma'_{xy} &= \frac{1}{G}\tau_{xy} \\ \gamma'_{yz} &= \frac{1}{G}\tau_{yz} \\ \gamma'_{zx} &= \frac{1}{G}\tau_{zx} \end{aligned}\right] \qquad [77]$$

In uniaxial state of stress,

if σ_x = applied uniaxial stress

then $\sigma_y = \sigma_z = \tau_{xy} = \tau_{yz} = \tau_{zx} = 0.$

Equations [74], [75] and [76] then reduce to

$$\varepsilon'_x = \frac{\lambda + G}{G(3\lambda + 2G)}\sigma_x \qquad [78]$$

$$\varepsilon'_y = \varepsilon'_z = \frac{\lambda}{2G(3\lambda + 2G)}\sigma_x \qquad [79]$$

where $\lambda = \dfrac{G(2G - E)}{E - 3G}$

(λ = Lamé's constant)

E = Young's modulus

G = Shear modulus.

The elastic strain limit is as difficult to determine in soil as it is in some ductile metals. The arbitrary elastic strain has to be small enough to ensure that the elastic limit is below or at the yield stress. The elastic

moduli obtained by the forced vibration method was substituted into equation [78] with σ_x chosen as the yield stress which was determined by the method described in section 7.3.2. For this purpose it was assumed that the yield stress is at the elastic limit. The computed strain was approximately 0.0005 cm per cm which implies that the elastic strain must be smaller than 0.05 percent. Hence the elastic strain is very small compared to total strain usually induced by soil-machine systems and therefore it can be neglected in determining the total force required to deform a soil. Only the permanent plastic strain is therefore considered.

10. APPLICATION OF THEORY OF PLASTICITY

10.1 General Review

Soil is primarily subjected to plastic deformation by soil machines. Plasticity theory was applied to deal with stresses and strains in soil masses resulting from the intrusion of machine systems. The behavior of soil is of course considerably different from that of an ideal plastic material, but analysis by plastic theory provides a theoretical basis on which the actual behavior of soil masses may be compared.

Limited work has been conducted on the study of soil flow beneath a wheel and plate. The experiments of Reece and Wong (50) have revealed the deformation of the soil body beneath wheels and showed that the effects at the soil-wheel interface depend on the whole soil flow field. Haythornthwaite (26) applied a method of upper and lower boundary solutions based on plastic equilibrium theory to study the grouser plate of a tracked vehicle. The results computed from values of shear strength parameters and dissipated energy were not satisfactory, particularly when α is large. Dagan and Tulin (15) also used a classical approach in applied mechanics: the soil behavior is represented by material constitutive equations, the stresses and velocity field are interrelated through equations of motion and the particular solution for the wheel is obtained by integration with the appropriate

boundary conditions.

Unfortunately the difficulties encountered in such an approach are formidable. The most important problem is the lack of a good mathematical representation of the soil behavior in the form of constitutive equations, dealing with relationships between stresses and strains. For the above reasons, in this preliminary study the problem has been simplified by adopting a number of assumptions and approximations throughout the analysis. When soil is subjected to intrusion of a soil-machine, the soil behavior is considered as a rigid-plastic incompressible material. Further assumptions are that soil-machines can be considered two-dimensional, rigid and undergoing steady motion. Soil behavior assumptions limits the applicability of results to soft clays with relatively high water content.

This section presents applications of theory and experiments to a number of soil-machine problems. Although a practical soil condition in the field would be different from laboratory test conditions, solutions by this method may provide some of the needed design parameters for soil-machine systems.

10.1.1. Theory

Consider a soil-machine travelling at a constant velocity in a soil mass. The strain rates introduced by the movement of the soil-machine in the

soil are denoted by $\dot{\varepsilon}_x$, $\dot{\varepsilon}_y$ and $\dot{\varepsilon}_z$ where the subscripts x, y and z refer to the coordinate axes. High moisture contented clay soil is assumed to be incompressible, and thus the following equation of incompressibility, relating the principal strain rates holds,

$$\dot{\varepsilon}_x + \dot{\varepsilon}_y + \dot{\varepsilon}_z = 0 \qquad [80]$$

The distortional strain rates $\dot{\varepsilon}_{xy}$, $\dot{\varepsilon}_{yz}$ and $\dot{\varepsilon}_{xz}$ are not small for large soil-deformation by soil-machines and may not be neglected. The generalized strain rate is defined as:

$$\dot{\varepsilon} = \frac{\sqrt{2}}{3}[(\dot{\varepsilon}_x - \dot{\varepsilon}_y)^2 + (\dot{\varepsilon}_y - \dot{\varepsilon}_z)^2 + (\dot{\varepsilon}_x - \dot{\varepsilon}_z)^2 + 6\,(\dot{\varepsilon}_{xy})^2 + 6\,(\dot{\varepsilon}_{yz})^2 + 6\,(\dot{\varepsilon}_{zx})^2]^{1/2} \qquad [81]$$

Since the principal displacements occur in planes parallel to the x - y plane and $\dot{\varepsilon}_z$ is negligible for a two dimensional system the problem reduces to plane strain. Hence

$$\dot{\varepsilon}_z = \dot{\varepsilon}_{xz} = \dot{\varepsilon}_{yz} = \dot{t}_{xz} = \dot{t}_{yz} = 0$$

and equation [81] becomes

$$\dot{\varepsilon} = \frac{\sqrt{2}}{3}[(\dot{\varepsilon}_x - \dot{\varepsilon}_y)^2 + (\dot{\varepsilon}_y)^2 + (\dot{\varepsilon}_x)^2 + 6\,(\dot{\varepsilon}_{xy})^2]^{1/2} \qquad [82]$$

The general procedure to be followed is now outlined. A relation must be obtained between the generalized

stress σ and the generalized strain ε. Concurrently the strain rate components must be found from kinematic considerations and the generalized strain rate $\dot{\varepsilon}$ found from [82]. The generalized stress then may be evaluated by the following manner. Figure 36 shows a typical true stress-strain curve for uniaxial compression in clay soil. The straight line is the corresponding stress-strain curve used in this analysis. In particular the elastic region of the curve is ignored completely and the approximate straight line relation to rigid plastic theory is applied. This is reasonable since soil deformations are sufficiently large to produce total strains much greater than the elastic strain. For many ductile materials, such as aluminum, the straight line approximation of the strain hardening portion of the stress-strain curve is satisfactory (53). The main advantage of this approximation is the resulting mathematical simplifications which do not greatly affect the validity of the analysis.

With the assumption of linear hardening, the generalized stress and strain increments are related by $\delta\sigma = E_t \dot{\varepsilon}$. Integration of this equation yields the following stress-strain relation

$$\sigma = \sigma_o + E_t \varepsilon \qquad [83]$$

where σ = generalized stress (flow stress)

σ_o = yield stress

E_t = slope of the line approximating the strain hardening portion of the stress-strain curve from a simple compression test

ε = generalized strain.

10.1.2. Plastic flow of cohesive soil

Indentation of clay soil by a rigid wedge was studied to observe the plastic flow and shear line patterns (Figures 58 and 59). As the wedge was pressed into the plastic clay body, the volume of raised "lips" on both sides of the wedge must be equal to the volume displaced by the wedge. The shear line pattern is indicated in Figures 58 and 60. To prove that cohesive soil is a plastic material which flows under the application of a load, consider the geometry of the wedge shown in Figure 60. AG is the undeformed surface and AE the "lip". AEB and CED are regions of constant state; BEC is a centered fan formed by the first shear lines.

If the vertical velocity of the wedge was taken as the unit of velocity, and if the time t was counted from the instant when the wedge touches the clay body, the depth of penetration equals t.

The "lip" AE makes an angle α-β with the X axis.

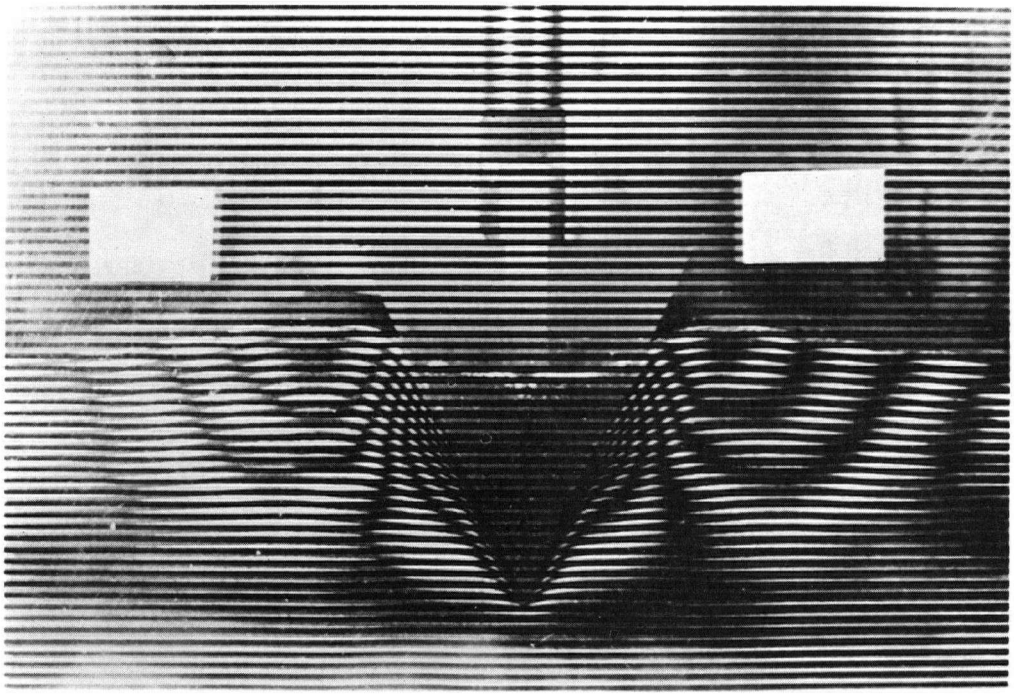

Figure 58. Moire fringe patterns induced by a 50° wedge. Y - displacement.

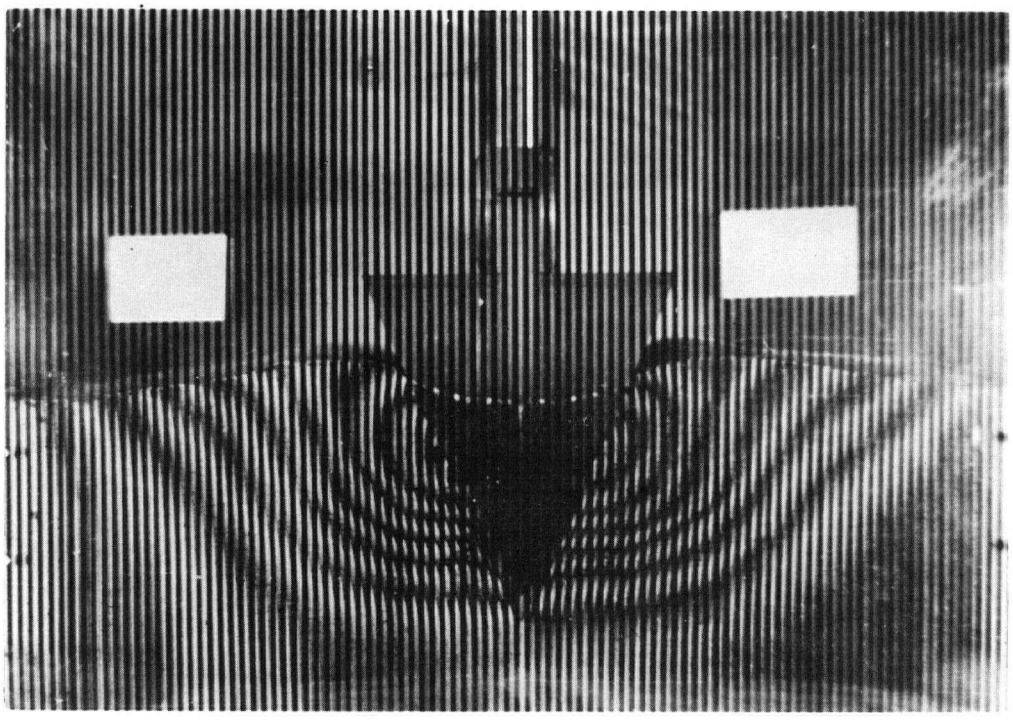

Figure 59. Moire fringe patterns induced by a 50° wedge. X - displacement.

Then a, b, and S are also found in terms of t, α, and β as follows:

$$a = \frac{t}{\cos \alpha - \sin (\alpha-\beta)} \qquad [84]$$

$$b = t \sin (\alpha-\beta) \frac{\sin \alpha + \cos (\alpha-\beta)}{\cos \alpha - \sin (\alpha-\beta)} \qquad [85]$$

$$s = \frac{t \sin (\alpha-\beta)}{\cos\alpha - \sin (\alpha-\beta)} \qquad [86]$$

and

$$\alpha = 1/2 \left[\beta + \cos^{-1} \tan \left(\frac{\Pi_1}{4} - \frac{\beta}{2}\right)\right] \qquad [87]$$

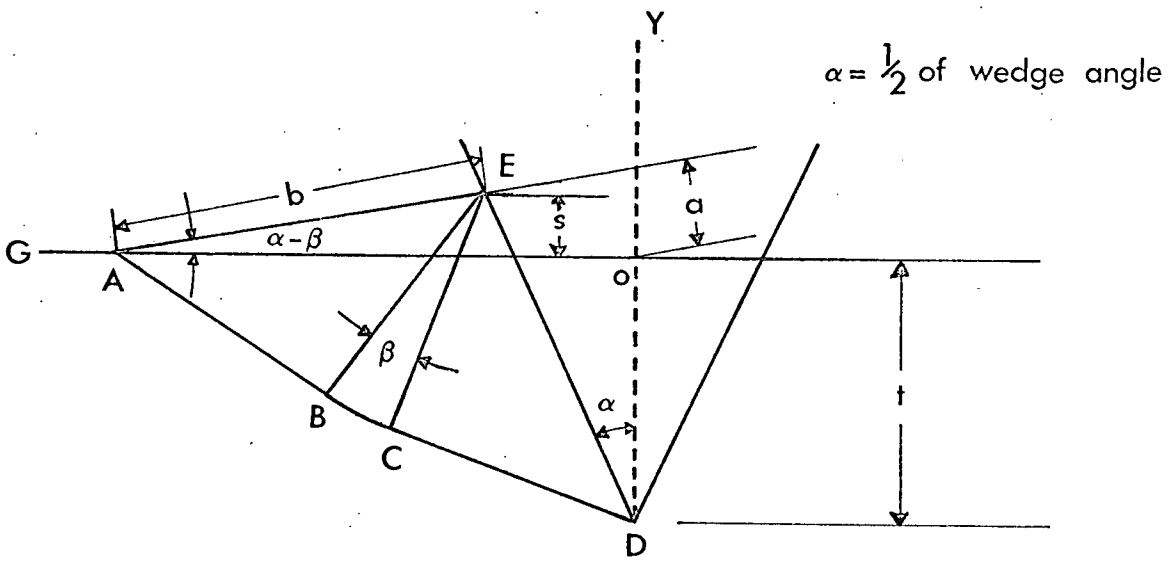

Figure 60. Possible stress field for indentation of a frictionless wedge in cohesive soil.

10.1.3. Wedge test

Those values a, b, s and α and β were measured from the experiment as shown in Figure 58. The differences were about 8.5 percent between the experiment and theoretical steady state flow. The raised "lip" AE was not a straight line.

The force F_1 necessary to drive the wedge into the plastic material is

$$F_1 = 2 P_f b (\sin \alpha + \mu' \cos \alpha) \quad [89]$$

where P_f = flow stress on the flank of the wedge

μ' = coefficient of sliding friction

Approximate flow stress was computed from the strains measured by moire method and yield stress measured by compression test. To simplify the theory, the strain hardening portion of the stress-strain curve from static compression tests was again approximated by a straight line (Figure 41). Finally, elastic strains, which are very small compared to plastic strains were neglected, and the material was regarded as incompressible. The yield stress can then be obtained from the compression test as described in section 7.3.2.

The force measured to drive the wedge into the clay soil and the force computed from equation [89]

after substituting flow stress obtained from equation [83] were less than 15 percent different. However, if soil was considered as a rigid-perfect plastic material and the approximated yield stress was substituted into equation [89] results differed by more than 30 percent. This increase was due to neglecting the strain-hardening effect, hence strain-hardening effect in cohesive soil can not be neglected. This experiment showed that plasticity theory may be applied as a means of analyzing soil-machine systems. Though clay soil behaves approximately like a plastic material, it still follows rate dependent theory. It is, therefore, concluded that clay soil is a visco-plastic material and strain rate has to be considered.

10.1.4. Grouser test

For further study on the validity of the Tresca yield criteria and approximated flow stress in soil subjected to the intrusion of a soil-machine, Type II and Type III grouser plates was conducted on soil Type I. The shape and dimensions of Type II and Type III grouser are given in Table III and Figure 61.

To satisfy the equilibrium conditions, the stress P_H and P_V acting over the area ab and bd must be equal to Q (Figure 63). The yield stress was computed the same way as in the indentation test. A

compression test specimen was made from an undisturbed part of the soil in the grouser experiment. The speed of the grouser and compression head were the same at 2 cm/min.

The force Q measured by the recorder and Q computed from the flow stress acting on the grouser plate were 26.4 Kg and 21.02 Kg respectively. The difference was increased compared to the wedge test probably due to additional approximations of the stress field under the grouser plate. However the difference was still less than 20 percent.

Grousers with three different trailing edges inclined at 30°, 45° and 60° were used for the comparison study in order to find an improved design in traction and floatation. As shown in Figures 64 and 67, this type would certainly decrease the traction though it showed an increase in floatation compared with the type shown in Figure 62 provided both types of grouser were fully submerged. This is due to stress concentration at the lifting edge resulting in non-uniform stress distribution in the soil under the grouser which causes early failure of the soil. Maximum traction occurs when uniform stress distribution is obtained. The problem of a dead zone at the intersection of vertical and horizontal plates occurred in edge trailed

grousers in the same way as in the other types.

From the above test, it can be concluded that the modified yield stress can be used to compute flow stress to the intrusion of soil-machine systems as an approximation method. Hence the moire method can be applied to soil to study desired design parameters in soil-machine model design.

TABLE II DIMENSION OF GROUSER TYPE I and II

Dimensions* / Shape		A	B	C	D	E	θ	Width
TYPE I	Grouser A	130		74	62	12	-	37
	Grouser B	65		43	31	12	-	37
TYPE II	Grouser A	70	66	71	37	8	30°	37
	Grouser B	70	48	71	37	8	45°	37
	Grouser C	70	39	71	37	8	60°	37

* All dimensions in millimeters

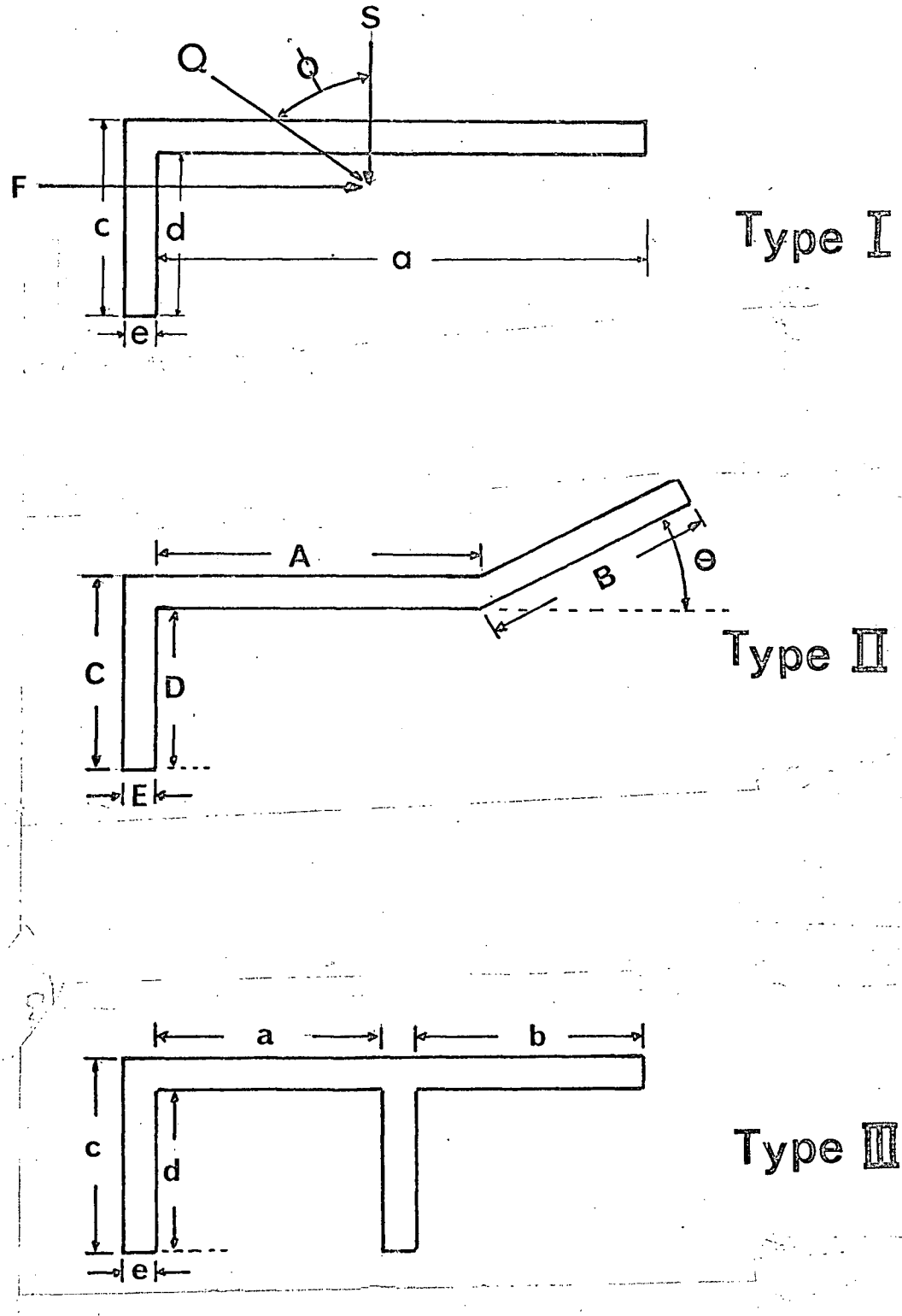

Figure 61. Grouser Type I to III and dimensions.

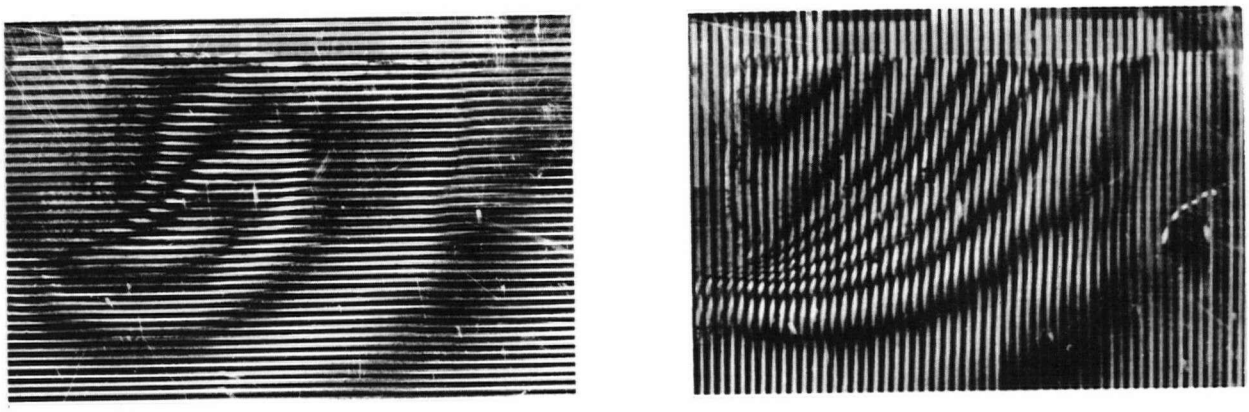

Figure 62. Moire patterns induced by Type I grouser loading.

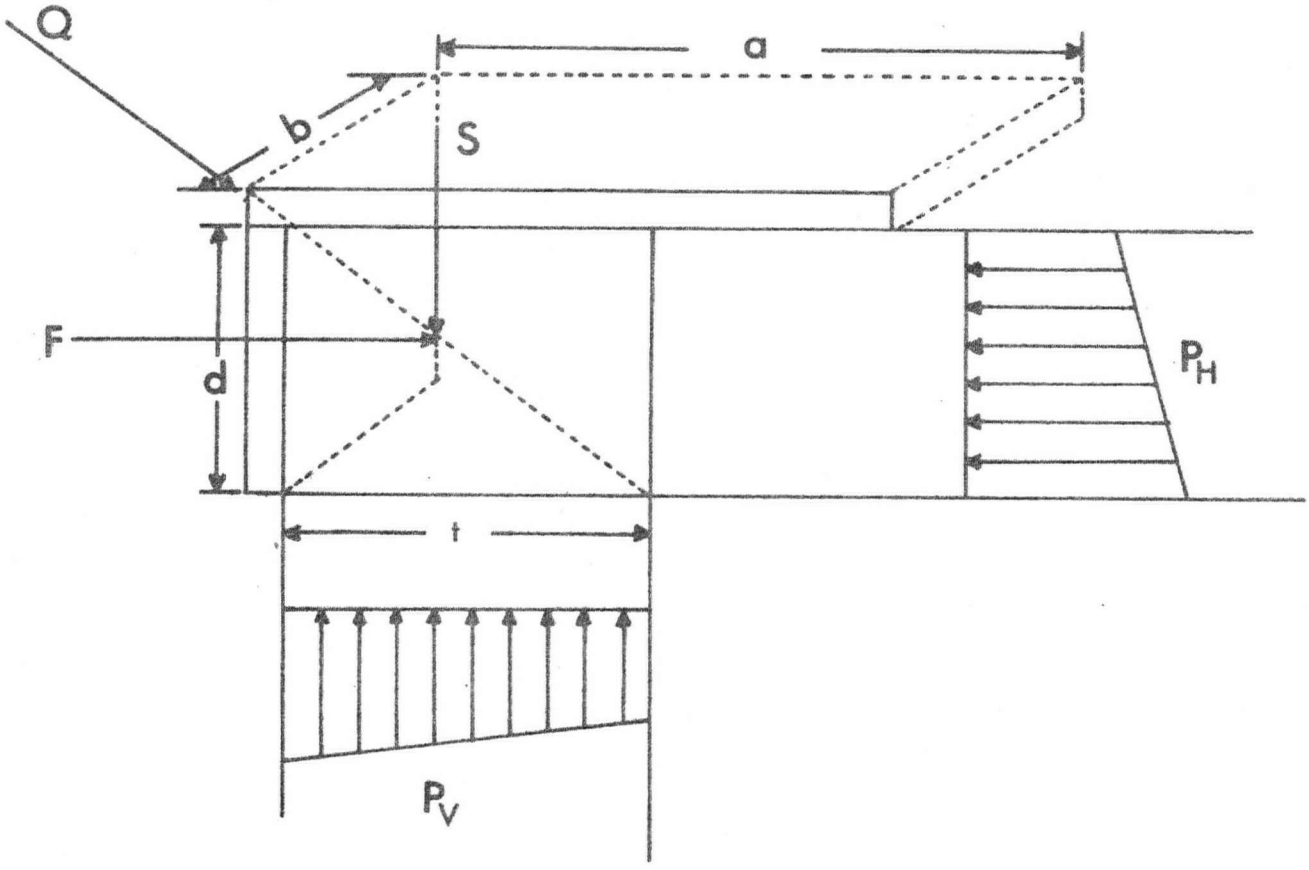

Figure 63. Possible stress field under the grouser Type I.

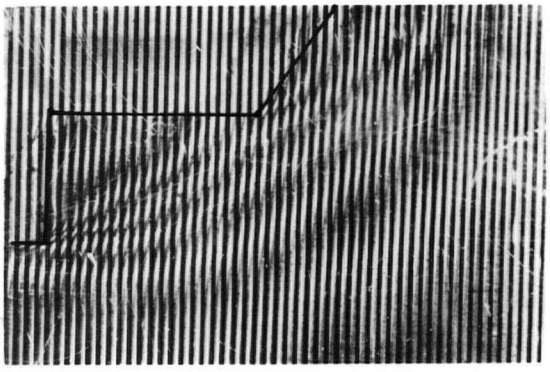

Figure 64. Moire fringe patterns formed under a 60° edge trailed grouser showing horizontal displacements.

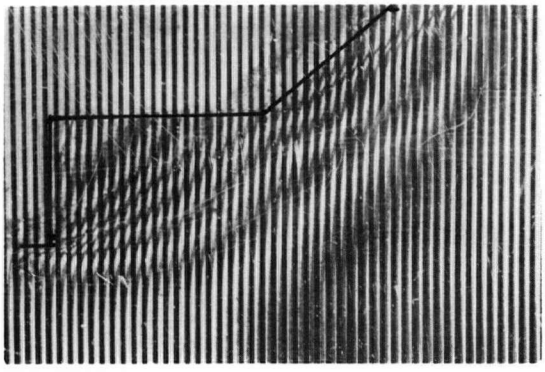

Figure 65. Moire fringe patterns formed under a 45° edge trailed grouser showing horizontal displacements.

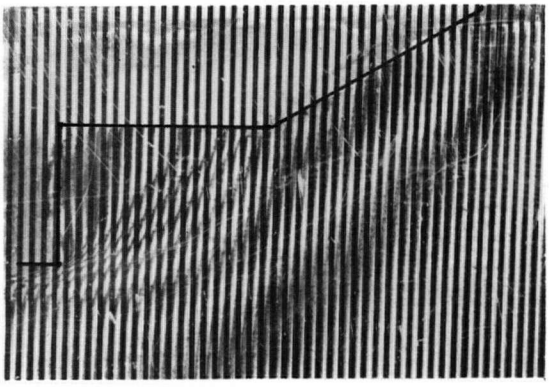

Figure 66. Moire fringe patterns formed under a 30° edge trailed grouser showing horizontal displacements.

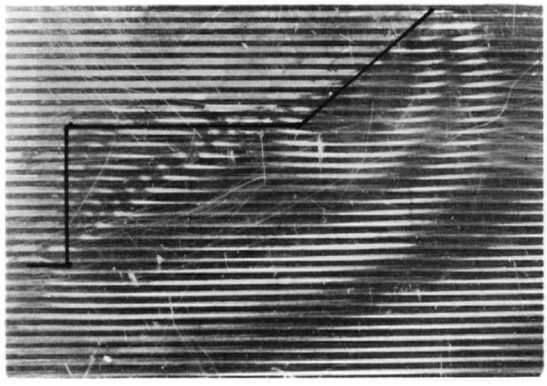

Figure 67. Moire fringe patterns formed under a 45° edge trailed grouser showing vertical displacements.

11. PHOTOELASTIC GELATIN AS A SIMULATED SOIL

11.1 General Review

Soil physical behavior induced by soil-machine systems is often difficult to investigate either analytically or experimentally. For example, in comparing design parameters affecting soil reactions, the validity of the analytic solution is questionable when soil-machine systems become complex. In addition, it is impossible to estimate an idealized mathematical model without experimental results as errors due to assumptions are inevitable.

Model tests can be used to examine the parameters of design shape, and provide a comparison to those of the prototype. A model can be tested in a prototype soil by manipulating the model under a desired condition. However, such methods require complex and expensive soil bin testing facilities. For this reason they often have limited appeal to a practicing engineer wishing to have answers to specific design problems.

In addition, it is difficult to examine differently shaped models under the same condition due to the problems of reproducing the physical characteristics of soils such as uniformity and bulk density. It is even more difficult to compare models with slight differences in shape since differences in results must distinguish between model shape and uncontrolled variation in soil conditions.

Photoelastic gelatin mixtures which have high optical sensitivity give an easier and simpler experimental approach to a specific test such as a simulated soil. Gelatin has been known for a long time but its early use was restricted because its mixtures were extremely fickle and weak.

However, since 1940, with the advent of large field diffused light polariscopes, gelatin has been used on a few occasions for specialized problems mostly on soil mechanic structures.

Farquharson and Hennes (18) used it to study stress in a mass of earth around tunnels. Crisp (14), Richards and Mark (51) and Tan (62) used it to analyze soil mass gravity structures. However, the most extensive study of gelatin properties has been carried out by Moreno and Benito (36), (37) in Spain including work on three-dimensional analysis. Osokina (44) and Shichabalov (58) in Russia also studied its physical property and used it in modelling geological cross sections.

Mellinger et al. (35) in the U.S. Army Engineer Division used it for the first time under dynamic loading conditions to investigate stress behavior under the moving vehicle wheel.

This study describes comparison tests of differently shaped model grousers using gelatin mixtures under static

conditions.

Viscoelastic behavior of gelatin mixture was described together with clay soil which may be considered to have similar viscoelastic properties.

Dimensional analysis for theoretical quantitative analysis within the elastic limit is given in Appendix II using viscoelastic constants as major physical variables.

11.2 Viscoelastic Properties of Soil and Gelatin

Rheological properties of clays have been studied extensively by Murayama and Shibata (38), (39), Christensen and Wu (9) and several others.

Murayama described its structure in terms of type of joints, elastic and viscoelastic joints, where no relative sliding between segments occurred at the elastic joint and the segment slides on the surface of the adjacent segment holding the adsorbed water at the viscoelastic joint. Hence he used the mechanical model as shown in Figure 69 which represents the rheological behavior of clay and obtained formulae well in agreement with the results of experiments.

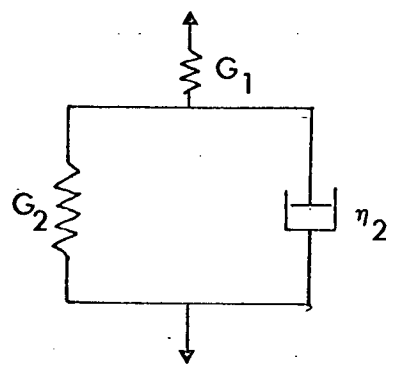

Figure 68. Kelvin model

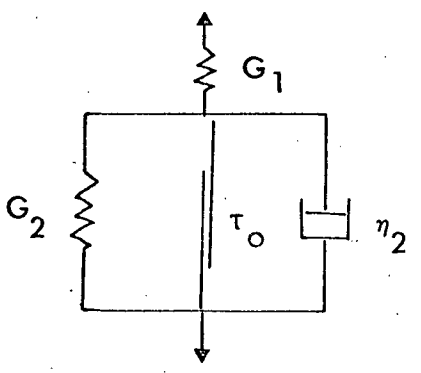

Figure 69. Murayama model

As shown in classical and Murayama viscoelastic mechanical models, it consists of an independent Hookean spring, G_1, connected in series with a Kelvin and a modified Kelvin element. The latter element is composed of a Hookean spring, G_2, and a dashpot, coefficient, η_2, and a slider τ_o in the Murayama model to represent non-linearity.

Christensen used another type of model as shown in Figure 70.

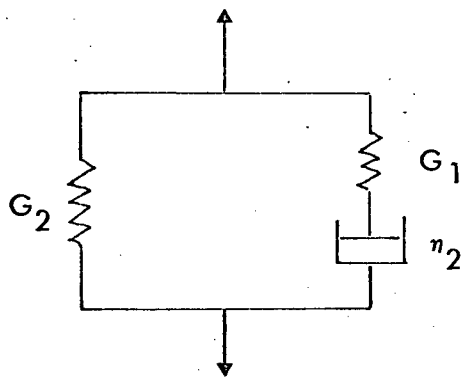

Figure 70. Christensen and Wu model

It may be erroneous to assume that all types of clay content soil belong to the above types of mechanical models. However they can be used to represent certain types of clay soils, and mathematical formulae derived from these models may be used to represent rheological properties of clay soil.

The rheological property of gelatin was, for the first time, expressed in terms of stress and strain as a

function of time, i.e. viscoelastic property, by Richards and Mark (51).They constructed the creep curve by plotting maximum shear strain as a function of time. As shown in Figure 71, a mechanical model which represents the viscoelastic property of gelatin was used and G_1, G_2, η_2, and η_3, the viscoelastic constants were evaluated.

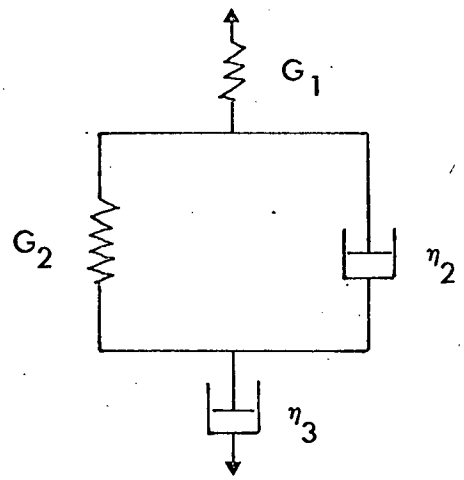

Figure 71. Maxwell and Kelvin model combination

11.3 Procedure and Apparatus

11.3.1. Preparation of gelatin mixtures

The gelatin mixture used consisted of; gelatin 20.58%, glycerin 21.60%, hydrochloric acid 2.11% and water 55.70% by weight. A refined, ground commercial gelatin was poured slowly into boiling distilled water with continuous stirring. After the gelatin mixture was cooled to 50°C, glycerin and acid were added. Additional acid may be added if improved transparency

of gelatin mixture is desired. When the mixture temperature reduced to 45°C, it was carefully poured through a funnel into the mould. Excessive air bubbles were screened out by a No. 100 Tyler sieve before pouring into the mould. The mould was kept in a refrigerator at 4.5°C for not less than 18 hours. A thin layer of silicon grease was applied to the surface of the mould to ease dismantling of the gelatin mixture prior to testing. A light (5w) lubricating oil was used during the test to reduce the friction between the gelatin mixture and glass.

A 25 cm field diffused light polariscope with mercury monochromatic and white light sources were used for all observations. Black and white, and colour photographs were taken with a Pentax camera using Kodak plus-X and Kodachrome II films. Only isochromatics were recorded by a circular polariscope in a dark field. Isoclinics were also recorded by a plane polariscope from which the stress trajectories were constructed.

11.3.2. The test soil-machine

The calibration mould, made of plexiglas had an inside dimension of 6.9 x 4.25 x 19 cm. Moulds for grouser tests were 45 x 3.8 x 15 cm. Model grousers made of plexiglas, consisting of 2 main types, type II and type III, and 3 different shapes each were

inserted in the surface of the gelatin in the mould immediately after the gelatin mixture was poured. The dimensions and shapes of grouser are given in Table III and Figure 61.

11.4 Results and Discussion

11.4.1. Block test

Tests on gelatin blocks were carried out by the same method used by Frocht (19) and by Durelli et al. (16) to evaluate elastic constants of the gelatin. These constants were calculated by measuring deformations and photoelastic fringe location on the square gelatin block standing under it own weight, which provided a condition of plane stress and plane strain. Hence plane stress and maximum shear stress can be easily evaluated. Fringe values and Young's modulus were calculated from the following equations:

$$f = \frac{\tau_{max}.H}{n} \qquad [90]$$

where f = gelatin fringe value

τ_{max} = maximum shear stress

H = thickness of model

n = fringe order

and,

$$E = \frac{d\ \mu\ 1}{\gamma - 1} \qquad [91]$$

where E = Young's modulus

d = density of gelatin

μ = Poisson's ratio for gelatin = 0.5

l = height of gelatin block

γ = increased ratio between the width at the bottom and top of the gelatin block.

A creep curve was constructed from the block test by plotting the maximum shear strain as a function of time for constant maximum shearing stress. As shown in Figure 72, the creep curve shows viscoelastic behavior, which may be represented by a Kelvin and Maxwell model combination (see Figure 71).

This model can be described by a mathematical equation:

$$\gamma = \tau\left[\frac{1}{G_1} + \frac{1}{G_2}\left(1 - e^{(G_2 t/\eta_2)}\right) + \frac{t}{\eta_3}\right] \qquad [92]$$

where, γ = shear strain

τ = constant shear stress

G_1 & G_2 = instantaneous and retarded shear moduli

η_2 & η_3 = material viscosities

t = time after application of the constant shear stress τ.

Hence we may be able to calculate viscoelastic constants G_1, G_2, η_2 and η_3 by taking a series of γ, τ, and t values from the creep curve.

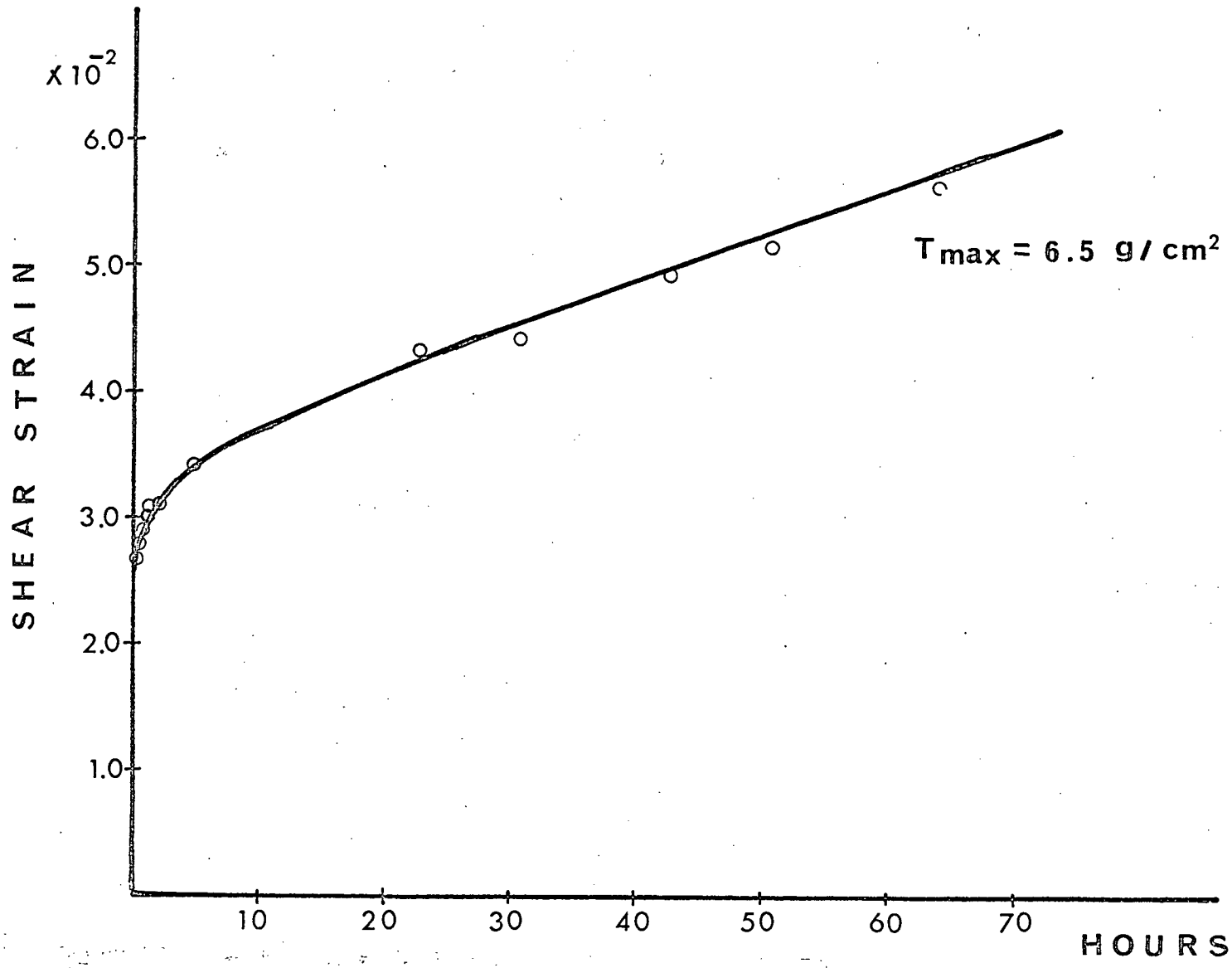

Figure 72. Creep curve for block test.

11.4.2. Grouser tests

Two different types of grousers were used to investigate the stress behavior in gelatin, or simulated soil. Figure 61 shows the types of grousers used and their dimensions are given in Table III.

TABLE III.DIMENSIONS FOR GROUSERS TYPE II AND III

Dimensions / Shape		A	B	C	D	E	θ	Width
TYPE III	Grouser A	25*	25	32	26	5.5	-	
	Grouser B	50	50	32	26	5.5	-	
	Grouser C	65	65	32	26	5.5	-	
TYPE II	Grouser D	70	66	71	37	8	30°	37
	Grouser E	70	48	71	37	8	45°	37
	Grouser F	70	39	71	37	8	60°	37

* All dimensions in millimeters

The static loads S and F (see Figure 61) were applied by dead weights, S = 631 grams and F = 1352 grams throughout all tests. The load F was applied by a pulley system.

Type III test

Three differently spaced grousers (A, B and C) as listed in Table III were analyzed. Isochromatics taken from these grousers are shown in Figure 75. Higher

fringe order or higher stress field was encountered in the front grouser and more uniformly distributed in the front and rear flanges as the spacing was increased. However, for all three grousers, the configuration of the fringe pattern was similar. The reason for a higher stress field on the front grouser was probably due to the narrow space between front and rear grousers, which causes a higher stress reaction due to compaction in front of the rear grouser. These isochromatic figures also show the configuration of maximum shear stress as it is half of the difference of two principal stresses. Figure 79 shows stress trajectories for grousers A, B and C respectively. Figure 79 shows that not much difference in stress trajectories exists between front and rear grousers regardless of spacings. However, the isoclinics for the first grouser expanded horizontally toward those of the second as the flange spacing increased. The result of this is to expand the Q stress trajectory (dotted line) more radially toward the rear of the grouser which should increase traction under the same normal load and grouser sinkage.

However, maximum traction for unit normal load can only be obtained by placing grousers at an optimum spacing as longitudinal space along the track is always

limited.

Type II test

Grousers with trailing edges inclined at 45° were used by Ikeda and Persson (28) to investigate the improvement of traction and floatation. However the angle of the trailing edge should be investigated to provide optimum performance. Three different trailing edge angles were investigated, grousers D-30°, D-45° and F-60°. All other dimensions appear in Table III.

As shown in Figure 76, grouser D gave the lowest fringe order at the trailing edge which relates more directly to reaction stress against sinkage than to traction. Hence grouser D would give best floatation. The highest fringe order was encountered at the front of grouser D, which contributes to traction. Increasing the trailing edge angle reduces the fringe order at the front of the grouser. However the steeper trailing edge angle yielded higher fringe orders under the trailing edge. Therefore, some doubt still exists as to whether grouser D would give the most superior performance in terms of resistance to sinkage and higher traction. Quantitative analysis would be required to prove any superiority.

Figure 78 shows stress trajectories for grousers D, E and F respectively.

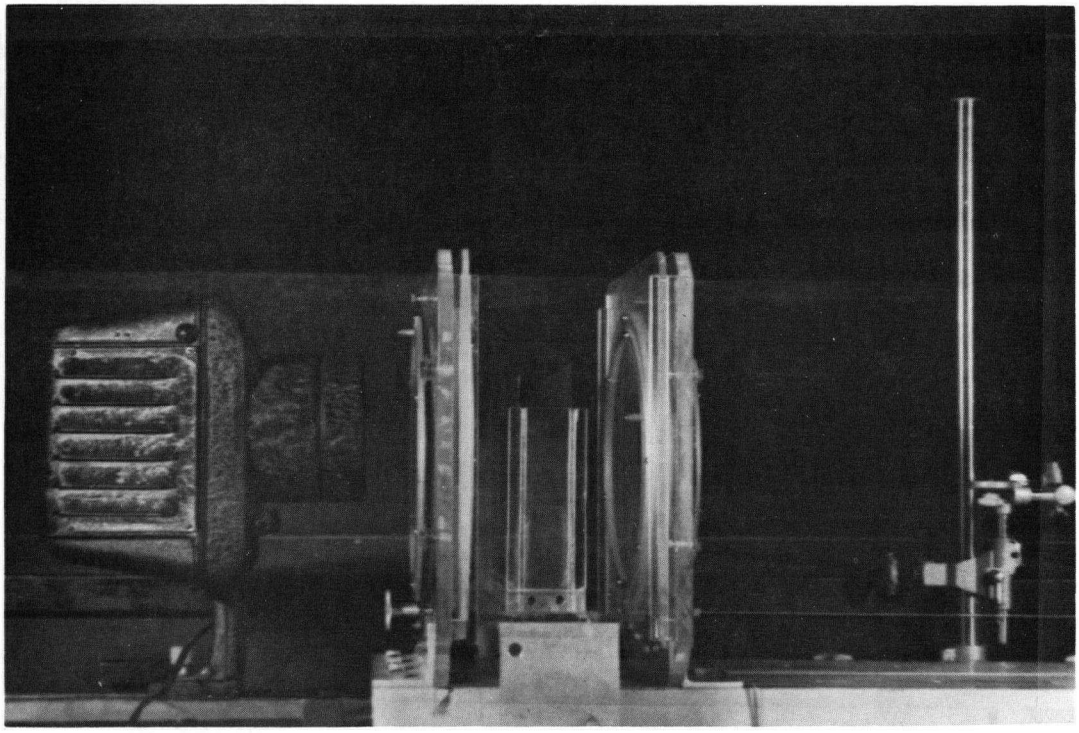

Figure 73. Polariscope

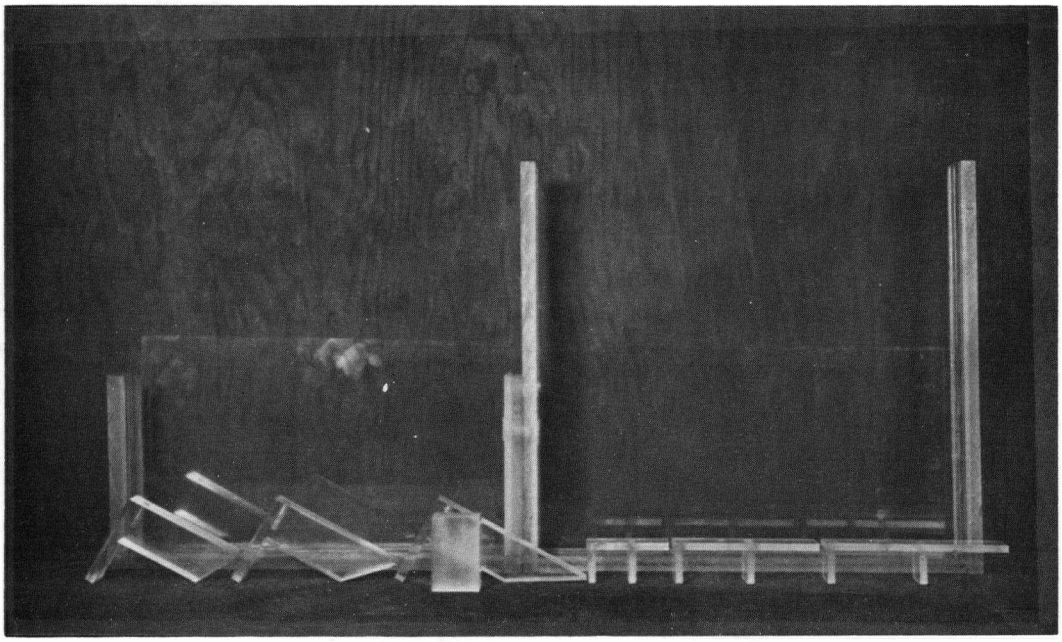

Figure 74. Grouser models and testing apparatus

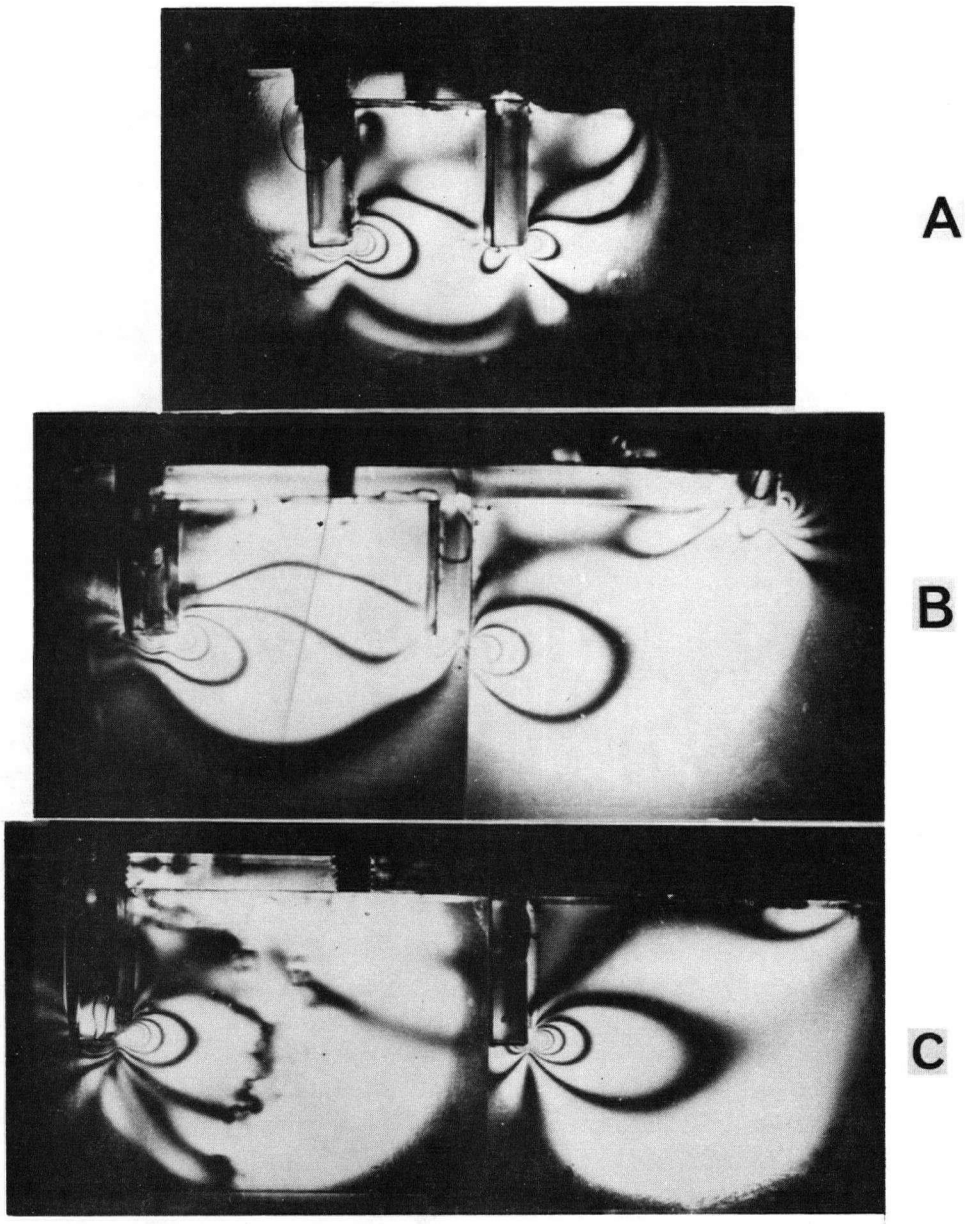

Figure 75. Isochromatics for grouser type A, B and C.

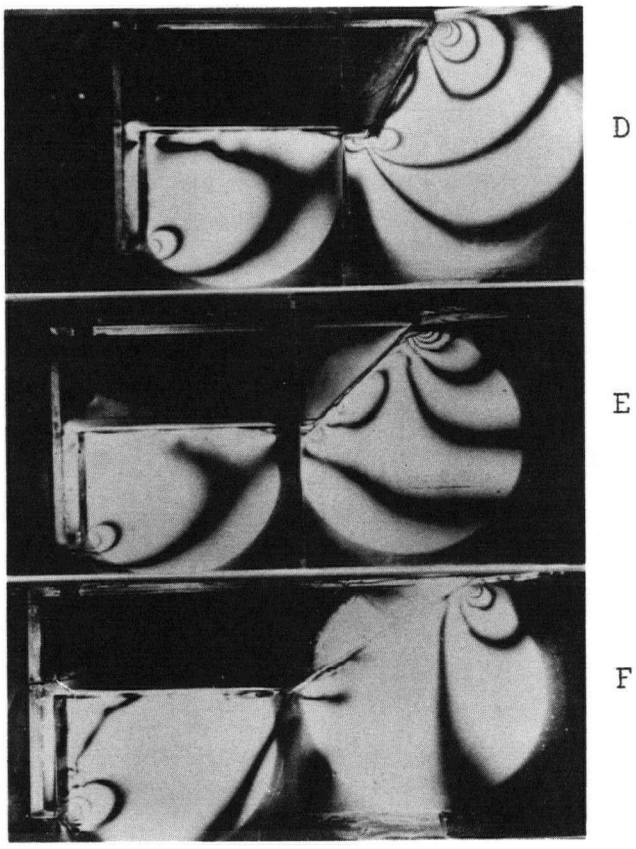

Figure 76. Isochromatics for grouser type D, E and F.

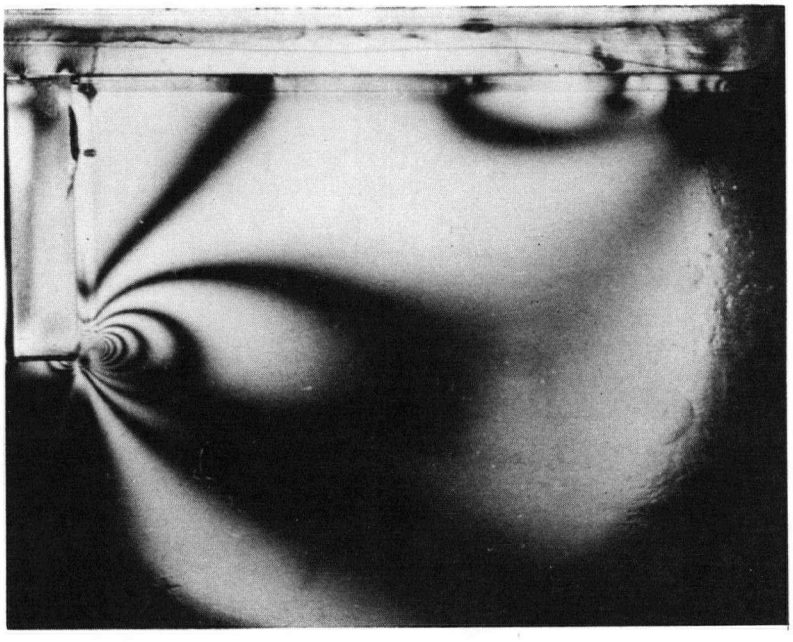

Figure 77. Isochromatic and isoclinic patterns under the Type I grouser.

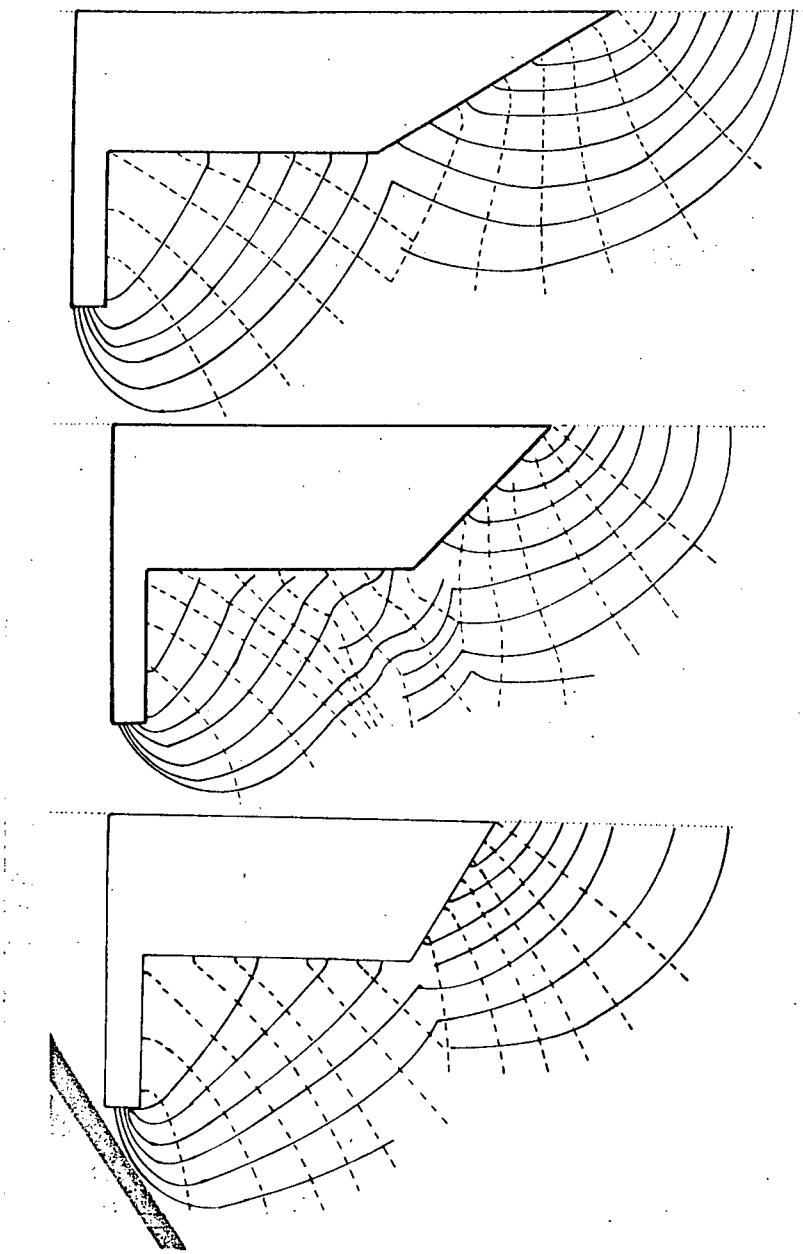

Figure 78. Stress trajectories under edge trailed grouser Type II. Constructed from photo-elastic gelatin. Edge trailed angle (A) 30°, (B) 45° and (C) 60°

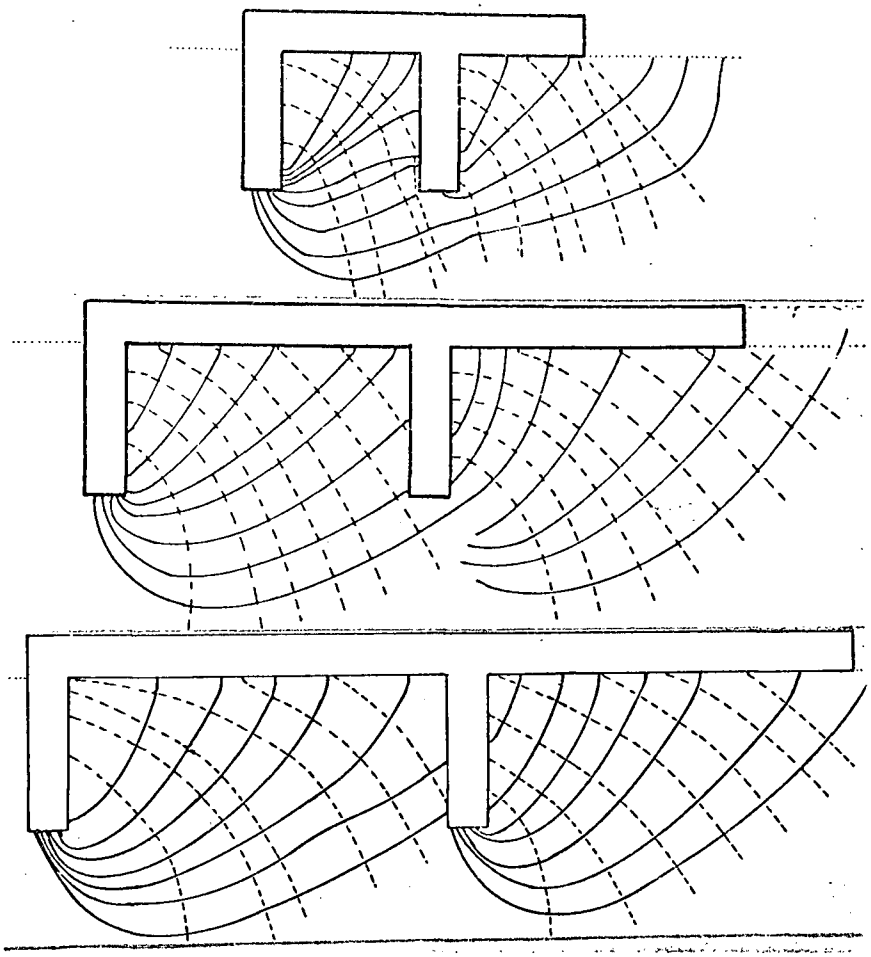

Figure 79. Stress trajectories under the grouser Type III. Constructed from photoelastic gelatin.

As stress trajectory figures show, P stress trajectories (solid line) at the trailing edge for grouser D showed more horizontally spreaded patterns toward the rear of the grouser while the Q stress trajectories (dotted lines) showed steeper gradients toward the bottom of the grouser which obviously contributes to floatation. However the stress trajectories of the front part of all grousers have similar patterns

regardless of the trailing edge angle, except for a more complex stress trajectory at the bottom of grouser E.

11.4.3. Comparison test between gelatin and actual soil

Sufficient information has been developed to analyze the stress trajectories and normal stress distribution on planes in the gelatin. It still requires however comparison on how closely it can be simulated on an actual soil. The following practical comparison was carried out.

Square Plate:

The analysis of stress behavior in the contact plane of the square plate was carried out in gelatin under the model square plate as shown in Figure 80 for qualitative comparison of results between simulated clay soil (gelatin) and real clay soil.

Stress distribution in the contact plane of the square plate (Figure 84) was evaluated by separating stresses along the lines of principal stress, A-A', B-B', and C-C' (Figure 83). As we see in Figure 82 it is not easy to determine the radius of curvature of the transverse lines of principal stress. However, lines of principal stresses intersect at successive isoclinic lines at angles varying from 60° to 90°.

One of Filon's methods for solving the Lame-Maxwell equations was used by applying cotangent values to angles between the P line and the isoclinic.

This equation is

$$\delta P = (P - Q) \cot \psi \, \delta\beta \qquad [92]$$

where δP = increment in P along the P line of principal stress

β = isoclinic parameter to one of the parameters $(\beta + \delta\beta)$ in this case the interval of $\delta\beta = 10°$.

ψ = angle between P line and the isoclinic.

(P - Q) values at the points of intersection of A-A', B-B'; and C-C' with isoclinics were obtained from the isochromatics in Figure 80.

Table IV shows the measurements from which the values P and Q, minimum and maximum principal stresses respectively are determined.

The results obtained from the gelatin model (Figure 84) showed good agreement with the results from clay tests in the Civil Engineering Handbook (11). Gelatin tests shown in Figure 84 and clay test results in reference (11) indicated high stresses measured under the edge of the plate, with stresses under the center of the plate somewhat less than average. This is due to the abilities of clay and gelatin to resist shear and tension. However, clay results showed a little

steeper gradient at the edge of the plate compared to the gelatin test due to higher shear and tensile strength properties of gelatin.

Isoclinics and stress trajectories are shown in Figures 81 and 82 respectively. In Figure 80, fringe patterns show the high concentration of shear stress at the edge of the plate.

Grouser test comparison. Comparison of stress trajectories by the moire and gelatin method are shown in Figure 85. The stress trajectories from the gelatin were established by observing isoclinics (Figure 77) and in the soil they were drawn by plotting the directions of maximum principal strain (or stress) measured by the moire method. The results were in agreement although gelatin showed more details. Results obtained in gelatin and in soil are shown in Figures 75, 78 and 64 to 67, respectively. As shown in Figure 85, sensitive gelatin showed more distinguishing stress concentration at the sharp corners and edges compared to the soil test. While qualitative results can be used quantitative results can not be compared as stresses in the gelatin are in the elastic region while in the soil they are in the plastic region.

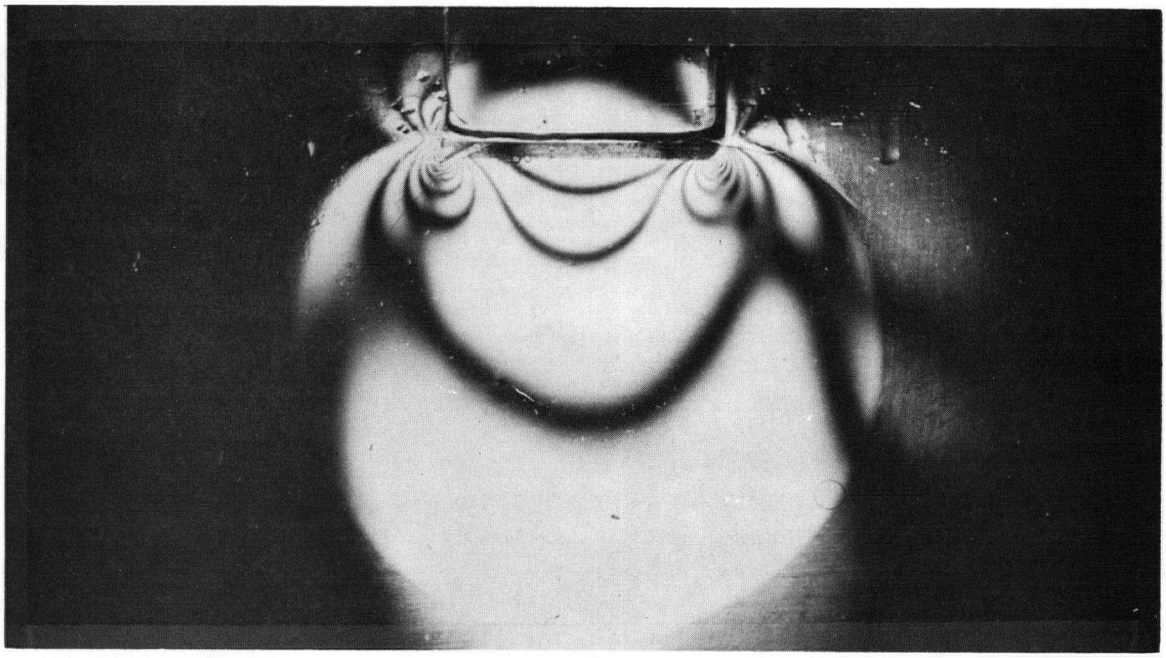

Figure 80. Isochromatic and isoclinics at 50° for 4.5 cm plate/

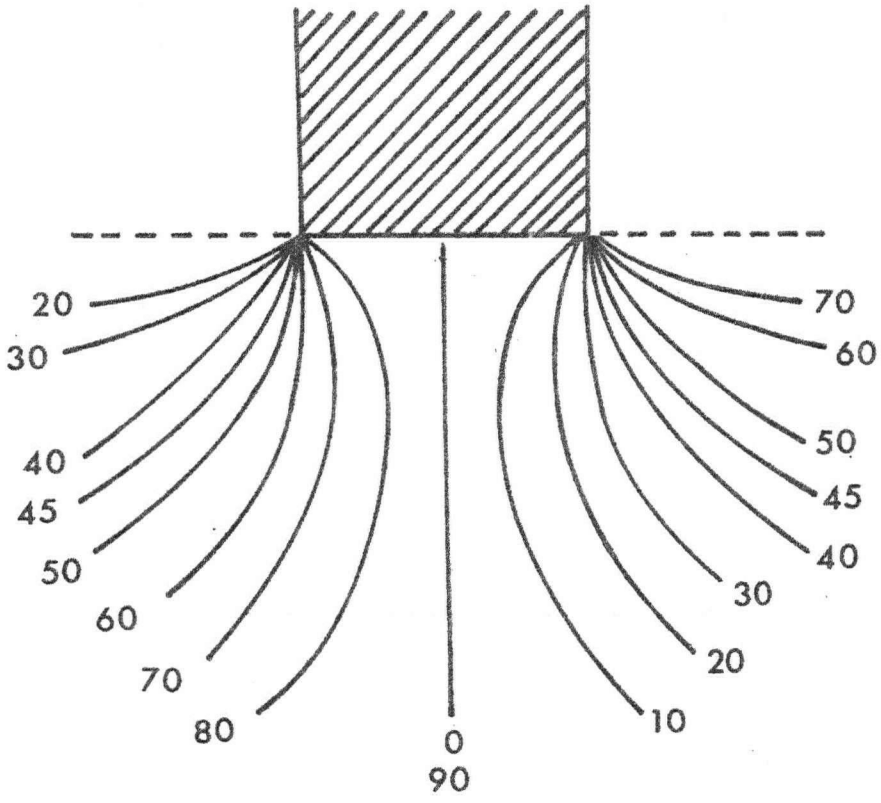

Figure 81. Isoclinics under the square plate.

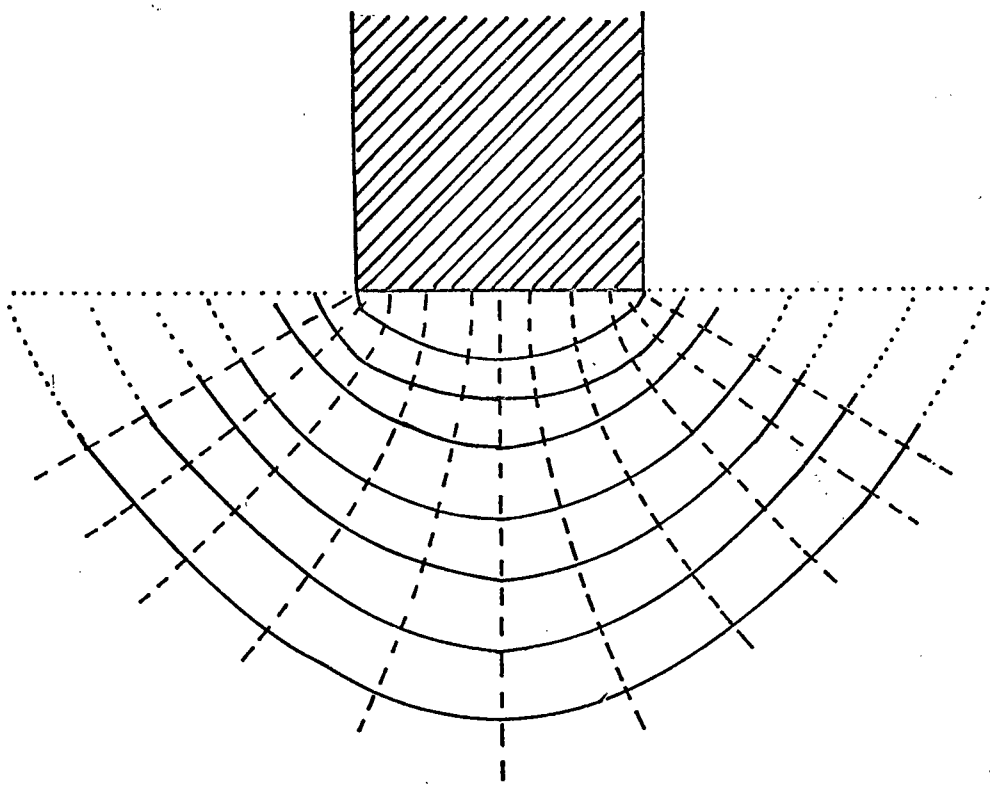

Figure 82. Stress trajectories under the square plate.

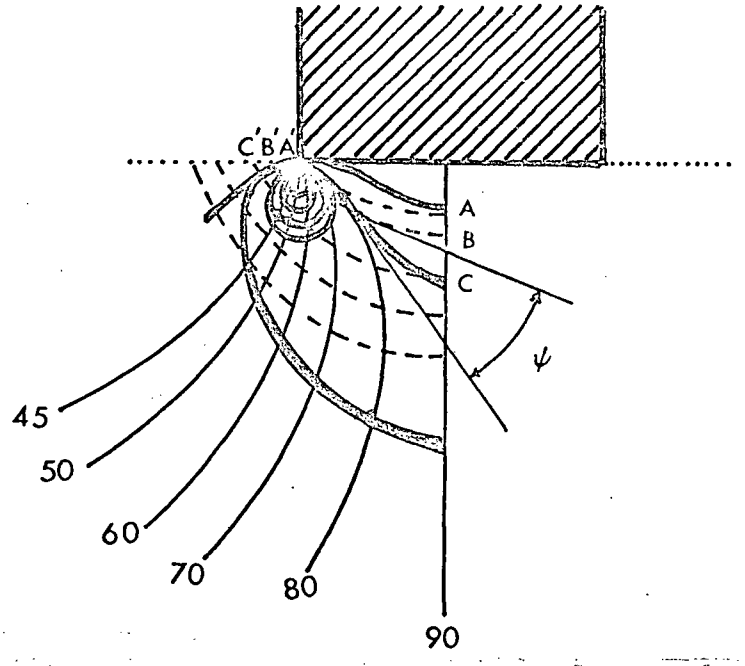

Figure 83. Isoclinics, isochromatics and stress trajectories under the square plate.

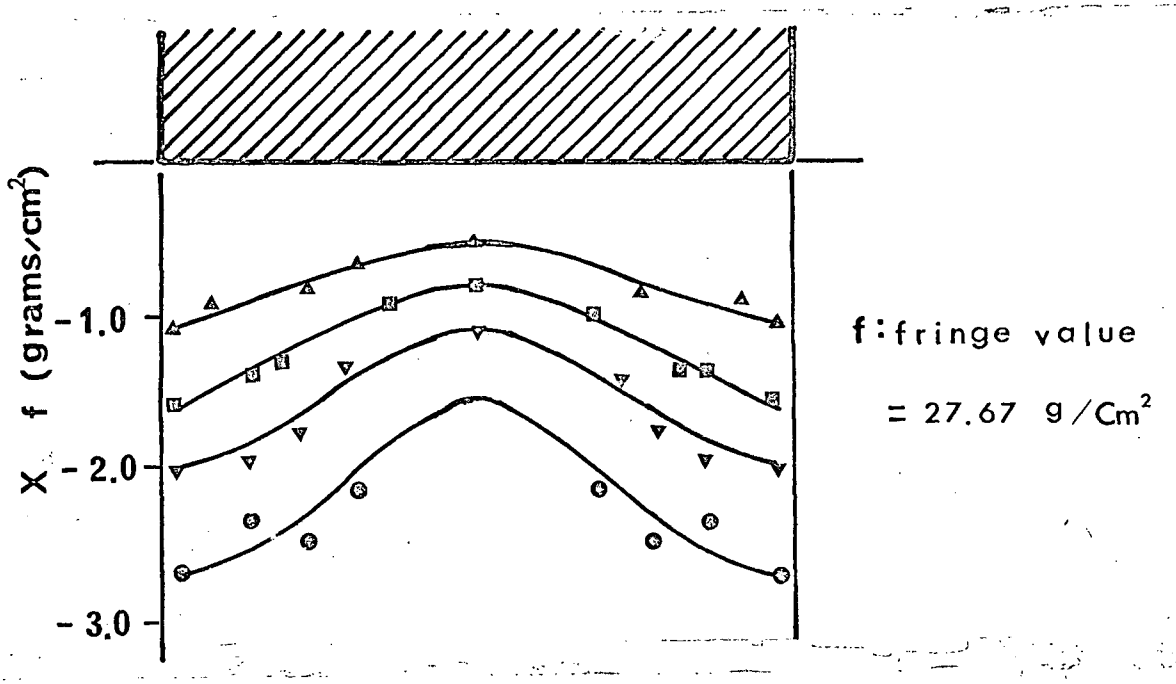

Figure 84. Stress distribution in the contact plane of the square plate.

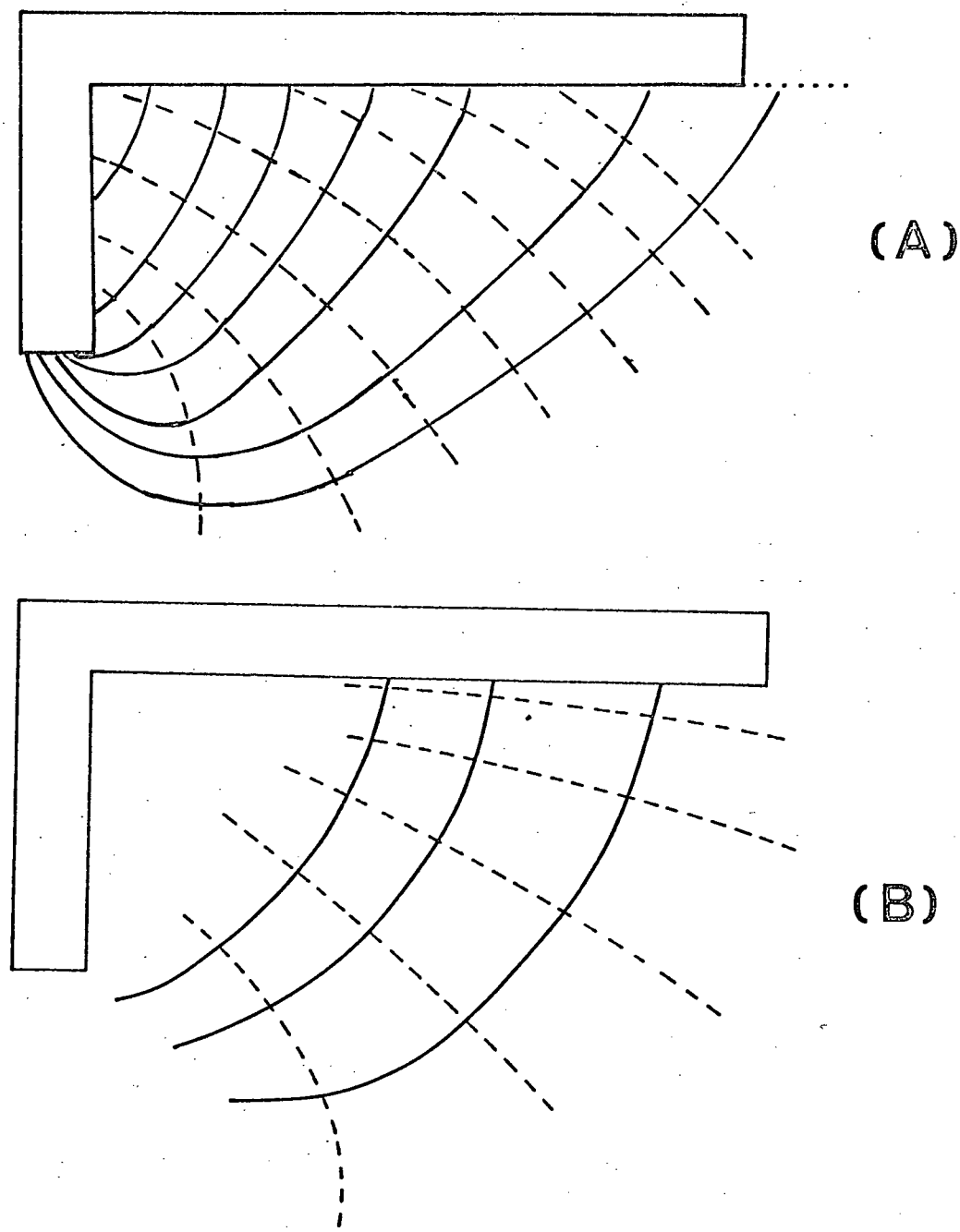

Figure 85. Stress trajectories under grouser Type I. (A) constructed from photo-elastic gelatin test. (B) constructed from moire pattern on Haney clay Type I.

TABLE IV. CALCULATION OF STRESSES ALONG LINE OF PRINCIPAL STRESS

Line of Principal Stress	P-Q (gr/cm^2)	ψ (Degrees)	cot ψ	(P-G) cot ψ	(P-Q) cot ψ (mean)	$\delta\beta$ Radians	δ P (gr/cm^2)	P (gr/cm^2)	Q (gr/cm^2)
A - A'	0	-	-	0		-	-	0	0
					0	0.175	0		
	1.1 f	90	0	0				0	-1.1 f
					3.73 f	0.175	0.653 f		
	2.0 f	15	3.73	7.46 f				0.653 f	-1.347 f
B - B'	0	-	-	0				0	0
					0	0.175	0		
	1.4 f	90	0	0				0	-1.4 f
					1.28 f	0.175	0.222 f		
	2.0 f	30	1.28	2.56 f				0.222 f	-1.78 f
					5.06 f	0.175	0.885 f		
	3.1 f	25	2.15	6.66 f				1.28 f	-1.82 f
C - C'	0	-	-	0				0	0
					0	0.175	0		
	2.1 f	90	0	0				0	2.1 f
					0.83 f	0.175	0.142 f		
	2.3 f	55	0.7	1.61 f				0.142 f	2.158 f
					1.86 f	0.175	0.326 f		
	2.5 f	50	0.84	2.1 f				0.468 f	2.232 f
					2.75 f	0.175	0.482 f		
	3.5 f	46	0.97	3.4 f				0.964 f	2.536 f

f = fringe value
P, Q = principal stress line

12. SUMMARY AND CONCLUSIONS

The following is a summary of the nature and scope of the complete study, the results of the experimental investigations and the subsequent conclusions. The study was limited to simple scaled soil-machine systems on Haney clay and on mixed Haney clay and Ottawa sand in semi solid to plastic range.

1. A new method for determining the physical and mechanical properties of soil was used to understand the more basic qualitative and quantitative soil reactions to the intrusion of soil-machine systems.

2. The moire technique can be used to find normal strains, maximum and minimum principal strains, direction of strains, shear strain and maximum shear strain in soils. Strains can be measured at any desired time on any particular region of interest. This technique has been applied to wedge-shaped tools, flat-blade tools and models of footings in high clay content soils. Two dimensional strain fields have been calculated to display characteristic differences between tool types. Hence the moire method can be successfully used to determine some of the design parameters of soil-machine systems.

3. The introduction of cone and pyramid loading heads significantly improved the compression test to approximate pure axial stress. The approximated yield stress and E_t

(tangential modulus) obtained from this type of compression test can be used to compute flow stress in soil resulting from the intrusion of soil-machines.

4. In comparison to the total strain produced in a soil by a soil machine the elastic strain is very small and the force required for elastic deformation of a soil can be neglected without significant error.

5. Rate dependency of Haney clay soil was verified by observing stress wave propagation in soil. Other qualitative physical properties were observed to influence stress wave propagation. It was found that wave velocity increased with increase of soil particle size while wave velocity decreased with increased soil moisture content. However, at high moisture content levels the slope of propagation velocity increment was decreased compared to the slope observed at lower moisture content levels.

6. Forced longitudinal and torsional vibration of a soil specimen permits the determination of elastic constants of soil.

7. Strain hardening effect was significant in cohesive soil and must be considered in stress-strain relationships. The soil cannot be considered as a perfectly rigid plastic material.

8. The theory of plasticity can be successfully used in conjunction with experimental observations to establish

stress-strain relationships in the soil on the assumption that strain hardening is linear and elastic strains are negligible.

9. The cohesive soil used in this study was a visco-plastic material since it was found to be rate dependent and closely followed plasticity theory.

10. Photo-elastic gelatin as a simulated soil provides a useful qualitative aid to design of soil-machine systems. Stress trajectories and slip lines studied by the gelatin method resembled the results observed by the moire method in actual soil.

13. RECOMMENDATIONS FOR FURTHER STUDY

Although this study provides many useful basic qualitative and quantitative soil parameters, for the development of soil-machine systems, the study is limited to Haney clay and to mixtures of Haney clay and Ottawa sands, in the plastic and semi-solid range.

Further investigations should be conducted on different soils in a wider range of water contents with additional soil-machine systems, to verify the validity of the method over a wider range of conditions.

A finer grid pitch should be developed for more accurate measurement of soil deformation by the moire technique.

APPENDIX 1

Theory for Stress Wave Propagation in a Visco-elastic Medium

When the wave length of longitudinal waves in a rod is large compared to the diameter of the rod, the wave propagation can be expressed adequately by a one-dimensional theory which neglects lateral inertia. The governing equations are that of motion,

$$\frac{\partial \sigma}{\partial x} = \rho \frac{\partial^2 u}{\partial t^2} \qquad [1]$$

the strain-displacement relation,

$$\varepsilon = \frac{\partial u}{\partial x} \qquad [2]$$

and the equation describing the mechanical properties of the solid. The latter is most conveniently taken in either the Laplace or Fourier representation. The Laplace method may be used as a technique for obtaining certain general results appertaining to the propagation of the wave front while, as might be expected, the Fourier method is important from an experimental viewpoint.

Solution by Laplace Transform

The Laplace transforms of equations [1] and [2] are respectively:

$$\frac{\partial \bar{\sigma}\ (x,s)}{\partial x} = \rho\ s^2\ \bar{u}\ (x,s) \qquad [3]$$

$$\bar{\varepsilon}\ \ (x,s) = \partial\ \bar{u}\ (x,s)\ /\ \partial x \qquad [4]$$

in which the equilibrium condition was assumed to be satisfied prior to t = 0, and where the explicit dependence of the stress and strain transforms on the spatial coordinate

has been recognized. Eliminating any two of $\bar{\sigma}$, $\bar{u}$, $\bar{\varepsilon}$ between equations [3], [4] and the Laplace transform $\bar{\sigma}$ in a form analogous to Hooke's law for an elastic solid

$$\bar{\sigma}\ (s) = E\ (s)\ \bar{\varepsilon}\ (s) \qquad [5]$$

leads to a second-order differential equation

$$\{\frac{\partial^2}{\partial x^2} - \mu^2\ (s)\}\ (\bar{\sigma},\ \bar{u},\ \bar{\varepsilon}) = 0 \qquad [6]$$

where $\mu\ (s) = \rho^{1/2}\ s\ [E\ (s)]^{-1/2}$ $(\mu > 0,\ \arg s = 0)$.

The general solution for [6] is given by

$$(\bar{\sigma},\ \bar{\varepsilon},\ \bar{u}) = A\ (s)\ e^{\mu(s)x} + B\ (s)\ e^{-\mu(s)x} \qquad [7]$$

where A(s), B(s) are to be determined by boundary conditions obtained in any specific problem.

Finally, by means of the inverse Laplace transformation, we obtain

$$\sigma\ (x,t) = (2\ \pi\ i)^{-1} \int_c \bar{\sigma}\ (0,\ s) e^{-\mu(s)x+st}\ ds \qquad [8]$$

for $x > 0$ and $t > 0$,

where

$$\bar{\sigma}\ (0,s) = \int_0^\infty \sigma\ (0,t)\ e^{(-st)}\ dt \qquad [9]$$

and $\mu(s)$ is determined from the equation

$$\mu^2 = \rho\ s^3 \int_0^\infty g\ (t)\ e^{(-st)}\ dt \qquad [10]$$

so that it is positive when s is real and positive. In this expression ρ is the density of the rod and g(t) is the strain per unit stress at time t after the application of a constant stress. This solution however is restricted to a mostly theoretical significance and the simplest solid.

Solution by Fourier Transform

The solution by Fourier methods closely parallels that of the Laplace transform. In place of equation [6],

$$\{\frac{\partial^2}{\partial x^2} - \lambda^2 (\omega)\} (\bar{\sigma}, \bar{\varepsilon}, \bar{u}) = 0 \qquad [11]$$

can be derived for the basic differential equation defining the Fourier transforms. In this equation the complex function λ of the real variable ω is given by

$$\lambda (\omega) = \lambda_1 (\omega) + i \lambda_2 (\omega) \qquad [12]$$

where λ_1 is a positive even function

$$\lambda_1(\omega) = (\rho/|E(i \omega)|)^{1/2} \omega \sin (\theta (\omega)/2) = 0 \qquad [13]$$

and λ_2 an odd function

$$\lambda_2(\omega) = (\rho/ |E(i \omega)|)^{1/2} \omega \cos (\theta (\omega)/2). \qquad [14]$$

The general solution of [11] is given by

$$(\bar{\sigma}, \bar{\varepsilon}, \bar{u}) = A (\omega) e^{\lambda x} + B (\omega) e^{-\lambda x} \qquad [15]$$

where A and B are determined by the boundary conditions.

For the semi-infinite rod $e^{\lambda x}$ diverges exponentially for large x. It follows that A(ω) vanished identically and that B is given by the Fourier transform,

$$\begin{aligned} \bar{\sigma} (x,\omega) &= \bar{\sigma} (0,\omega) e^{-\lambda x} && \text{(a)} \\ \bar{u} (x,\omega) &= \bar{u} (0,\omega) e^{\lambda x} && \text{(b)} \\ \bar{\varepsilon} (x,\omega) &\quad \bar{\varepsilon} (0,\omega) e^{\lambda x} && \text{(c)} \\ \bar{v} (x,\omega) &= \bar{v} (0,\omega) e^{\lambda x} && \text{(d)} \end{aligned} \qquad [16]$$

The inversion of equation [16a] is given by

$$\sigma\ (x,t) = \frac{1}{2\pi} \int_{-\infty}^{\infty} \bar{\sigma}\ (0,\omega)\ e^{-\lambda x + i\omega t}\ d\omega \qquad [17]$$

When $\sigma\ (0,t)$ is real, [17] may be expressed in more physically significant form,

$$\sigma\ (x,t) = \frac{1}{\pi} \int_{o}^{\infty} [\sigma_R(\omega)\ \cos\ \{\omega(t - x/c(\omega)\}$$

$$-\sigma_1\ (\omega)\ \sin\ \{\omega(t - x/c(\omega))]\ e^{-\alpha(\omega)x}\ d\omega \qquad [18]$$

Where σ_R and σ_1 are the real and imaginary components of $\bar{\sigma}\ (0,\ \omega)$:

$$\sigma_R(\omega) = \int_{-\infty}^{\infty} \sigma(0,t)\ \cos\ (\omega t)\ dt \qquad [19]$$

$$\sigma_1(\omega) = \int_{-\infty}^{\infty} \sigma(0,t)\ \sin\ (\omega t)\ dt \qquad [20]$$

and where

$\bar{\sigma}\ (0,\omega) \equiv \sigma_R\ (\omega) + i\ \sigma_1\ (\omega)$ $c\ (\omega)$ and $c\ (\omega)$ are positive even functions defined by the equations

$$\alpha\ (\omega) = \lambda_1\ (\omega) \qquad [21]$$

$$c\ (\omega) = \omega/\lambda_2\ (\omega) \qquad [22]$$

APPENDIX II

Conditions of Viscoelastic, Statical Similarity

A system defined by the following quantities is considered:

τ	=	maximum shear stress	ML^{-2}
H	=	grouser length	L
D	=	other pertinent lengths	L
G_1	=	independent hookean spring constant	ML^{-2}
G_2	=	spring constant in Kelvin model	ML^{-2}
η_2	=	dashpot coefficient in Kelvin model	$ML^{-2}T^{-1}$
W	=	force applied	M
g	=	acceleration of gravity	LT^{-2}

From the above identified physical variables, dimensionless terms, called "Pi" terms, were established as in the Buckingham Π theorem.

Thus the general equation for maximum shear stress in the soil can be expressed as:

$$\frac{\tau}{G_1} = f\left[\frac{H\eta_2^2}{gG_1^2}, \frac{G_2 g^2 \eta_2^4}{G_1^4}, \frac{W \eta_2^4}{g^2 G_1^5}\right] . \qquad [1]$$

Since the above equation is entirely general, it applies to any other system, in this case gelatin, which is a function of the same variables. Hence it applies to a specific system called the model, and the following design and operating conditions should be satisfied.

$$\frac{\tau}{G_1} = \frac{\tau m}{G_{1m}} \qquad [2]$$

$$\frac{H\eta_2^2}{G_1^2} = \frac{H_m\eta_{2m}^2}{G_{1m}^2} \qquad [3]$$

$$\frac{G_2\eta_2^4}{G_1^4} = \frac{G_{2m}\eta_{2m}^4}{G_{1m}^4} \qquad [4]$$

and:

$$\frac{W\eta_2^4}{G_1^5} = \frac{W_m\eta_{2m}^4}{G_{1m}^5} . \qquad [5]$$

Since $g = g_m$, and where sub-m applies for the model.

Once laboratory tests provide the viscoelastic constants for the soil to be used, and the model scale η is decided, the G_{1m} could be evaluated by selecting the proper η_{2m} from the tables of viscoelastic constants of gelatin. As ;

$$G_{1m} = \frac{\eta_{2m}\, G_1}{\eta_2}\, n^{1/2} \qquad [6]$$

then G_{2m}, W_m could also be calculated from the equation

$$G_{2m} = \frac{G_2\, \eta_2^4\, G_{1m}^4}{G_1^4\, \eta_{2m}^4} \qquad [7]$$

and

$$W_m = \frac{G_{1m}^5\, W\eta_2^4}{G_1^5\, \eta_{2m}^4} . \qquad [8]$$

If above design and operating conditions would be satisfied, the τ_m obtained from gelatin test would predict the τ in the soil to be tested by the prototype machine from the

equation:

$$\tau = \tau_m \frac{G_l}{G_{lm}} , \qquad [9]$$

14. BIBLIOGRAPHY

1. Ang, A.H.S. and G.C. Chang. Numerical calculation of inelastic plane soil-structure interaction. Proceedings International Symposium on Wave Propagation and Dynamic Properties of Earth Materials, pp. 393-409 (1967).

2. Baker, W.J. and G.E. Triandafilidis. Kinematics of wave propagation in laterally confined columns of sand. Proceedings International Symposium on Wave Propagation and Dynamic Properties of Earth Materials, pp. 411-422 (1967).

3. Barnes, K.K., C.W. Bockhop and H.E. McLeod. Similitude in studies of tillage implement forces. Agricultural Engineering, Vol. 41, No. 2, pp. 32-37 (January 1960).

4. Batdorf, S.B. Air-induced ground shock - a one dimensional theory. Proceedings International Symposium on Wave Propagation and Dynamic Properties of Earth Materials, pp. 423-432 (1967).

5. Biot, M.A. Theory of Propagation of elastic waves in a fluid-saturated porous solid. Journal of Acoustic Soc. of America, Vol. 28, No. 2 (1956).

6. Bockhop, C.W. Similitude in investigations of tillage implements. Unpublished Ph.D. thesis. Ames, Iowa. Library, Iowa State University of Science and Technology (1957).

7. Boyd, C.W. Investigations of dry sand behavior under moving rigid wheels. Unpublished Ph.D. thesis. Department of Civil Engineering and Applied Mechanics, McGill University, (1967).

8. Casagrande, A. and S.D. Wilson. Effect of rate of loading on the strengths of clays and shales at constant water content. Geotechnique, Vol. 2, pp. 251- (1951).

9. Christensen, R.W. and T.H. Wu. Analysis of clay deformation as a rate process. Journal of the Soil Mechanics and Foundation, ASCE, 90: pp. 125-157 (1964).

10. Chancellor, W.J. and R.H. Schmidt. Soil deformation during piston sinkage. Agricultural translation 5: (2) pp. 235-239 (1962).

11. Civil Engineering Handbook, Fourth Edition, McGraw-Hill, pp. 8-87 (1959).

12. Constantino, C.J., A. Wachowski and U.L. Barnwell. Finite element solution for wave propagation in layered media caused by a nuclear detonation. Proceedings International Symposium on Wave Propagation and Dynamic Properties of Earth Materials, pp. 59-70 (1967).

13. Cooper, A.W., G.E. Vanden Berg, H.F. McColly and A.E. Erickson. Strain gauge cell measures soil pressure, Agricultural Engineering 38: pp. 232-235, 246 (1957).

14. Crisp, J.D.C. The use of gelatin models in structural analysis. Proc. (B) Inst. of Mech. Eng., 1 B (12), pp. 580-604 (1952).

15. Dagan, G and M.P. Tulin. A study of the steady flow of a rigid plastic clay beneath a driven wheel. Journal of terramechanics, Vol. 6, pp. 9 (1969).

16. Durelli, A.J., E.A. Phillips and C.H. Tsao. Introduction to the Theoretical and Experimental Analysis of Stress and Strain. McGraw-Hill, New York (1958).

17. Durelli, A.J. and W.F. Riley. Performance of embedded pressure gauges under static and dynamic loadings. Sixty-fourth Annual Meeting Symposium on Soil Dynamics, A.S.T.M., pp. 20-37 (1962).

18. Farquharson, F.B. and R.G. Hennes. Gelatin models for photoelastic analysis of stress in earth masses. Civil Engrg., 10: (4) pp. 211-214 (1940).

19. Frocht, M.M. Photoelasticity. John Wiley and Sons, New York (1941 and 1948) 2 vols.

20. Geuze, E.C.W.A. The uniqueness of the Mohr-Coulomb concept in shear failure. Laboratory shear Testing of Soils. ASTM Spec. Publ. 361, pp. 52-64 (1963).

21. Gill, W.R. Soil deformation by simple tools. Transactions of ASAE, Vol. 12, No. 2, pp. 234-239 (1969).

22. Gill, W.R. and G.E. Vanden Berg. Soil dynamics in tillage and traction. Agricultural Research Serive, United States Department of Agriculture. Agriculture Handbook No. 316.

23. Gupta, C.P. and A.C. Pandya. Behavior of soil under dynamic loading. Its application to tillage implements. Trans. of ASAE 10 (3), pp. 352-358, 363.

24. Hampton, D. and R.A. Wetzel. Stress wave propagation in confined soils. Proceedings International Symposium on Wave Propagation and Dynamic Properties of Earth Materials, pp. 433-442 (1967).

25. Hardin, B.O. and W.L. Black. Vibration modulus of normally consolidated clay. Journal of Soil Mechanics and Foundations Division, ASCE, Vol. 94, No. SM2, pp. 353-369 (1968).

26. Haythornwaite, R.M. Methods of plasticity in land locomotion studies. Proc. 1st Intern. Conf. Mech. Soil-Vehicle Systems, Turin (1961).

27. Hunter, S.C. Progress in solid mechanics, pp. 26-28. Amsterdam, North Holland Publishing Co. (1960).

28. Ikeda, T. and S.P.E. Persson. A track shoe for soft soil. Transactions of the ASAE 11: No. 6, pp. 746-749 (1968).

29. Ishihara, K. Propagation of compressional waves in a saturated soil. Proceedings International Symposium on Wave Propagation and Dynamic Properties of Earth Materials, pp. 451-467 (1967).

30. Ishimoto, M. and K. Irda. Determination of elastic constants of soils by means of vibration methods. Bull. Earthquake Research Institute, Vol. 15, pp. 67 (1937).

31. Khamidov, A. Use of gamma-rays in the study of the effects of wheels on the soil. Trudy VIM 28: pp. 94-107, illus. Journal Agricultural Engineering Res. 6: pp. 147-1521 Eng. Translation (1961).

32. Kondner, R.L. Stress-strain-time spectrum response of a cohesive soil high speed testing. Vol. V. Interscience, pp. 147-162 (1965).

33. Kondner, R.L. Stress wave propagation in terms of dynamic response spectra. Proceedings International Symposium on Wave Propagation and Dynamic Properties of Earth Materials, pp. 483-490 (1967).

34. Kostritsyn, A.K. Cutting of a cohesive medium with knives and cones. Vsesoiuzz. Akad. Sel skokhoziaistuennyich Nank. Zeml. Mekh. Sborn. Trudov. (Leningrad) 3, - pp. 247-290. Natl. Inst. Agri. Engin., English translation 58. (1956).

34A. Lambe, T.W. Soil Testing for Engineers, pp. 99. Wiley and Sons (1951).

35. Mellinger, F.M., J.H. Hubbard and R.L. Peters. Photoelastic studies for vehicle mobility research. U.S. Army Engineer Waterways Experiment Station, Corps of Engineers, Vicksburg, Miss., Contract Report No. 3-118 (August 1965).

36. Moreno, C.A. Estudio de gelatinas para modelos foto-elasticos, Laboratorio Central de Ensayo de Materiales de Construccion, Pub. No. 58, Madrid (1958) (In Spanish).

37. Moreno, C.A. and C. Benito. Estudio fotoelasticos tridimensionales con modelos de gelatina. Lab. Central ENsayo de Mat. de Const. Pub. No. 73, Madrid (1960) (In Spanish).

38. Murayama, S. and T. Shibata. Flow and stress relaxation of clays. Springer-Verlog. Berlin/Heidelberg (1966).

39. Murayama, S. and T. Shibata. Rheological properties of clays. Proceedings, 5th International Cong. on Soil Mech. and Foundations (6) pp. 26-29, Paris, France (1961).

40. Nacci, V.A. and R.J. Taylor. Influence of clay structure on elastic wave velocities. Proceedings International Symposium on Wave Propagation and Dynamic Properties of Earth Materials. The University of New Mexico Press, pp. 491-502 (1968).

41. Nichols, M.L. and I.F. Reed. Soil dynamics VI. Physical reactions of soils to moldboard surfaces. Agricultural Engineering 15: pp. 187-190 (1934).

42. Nichols, M.L., I.F. Reed and C.A. Reaves. Soil reaction: To plow share design. Agric. Engineering 39: pp. 336-339 (1958).

43. Olson, D.J. and J.A. Weber. Effect of speed on soil failure pattern in front of tillage tools. Paper No. 650691, S.A.E. (1965).

44. Osokina, A.M. Solutions of gelatin and glycerin as a material for photoelastic measurement. Colloid Jnl. 19: (6), (1957).

45. Plantema, G.A. Soil pressure cell and calibration equipment. 3rd Internatl. Conf. Soil Mech. and Found. Engin. Proc. (Zurich) Vol. 1, pp. 283-288 (1953).

46. Prager, W. and P.E. Hidge. Theory of perfectly plastic solids, Wiley and Sons, Inc. (1951).

47. Reaves, C.A., A.W. Cooper and F.A. Kummer. Similitude in performance studies of soil-chisel systems. Transactions of ASAE, Vol. 11, No. 5, pp. 658-660, 664 (1968).

48. Reaves, C.A., R.L. Schafer, R.J. Garrity and C.P. Kolthoff. Similitude of bulldozer blade, pp. 577-579, 583 (1969).

49. Redshaw, S.C. A sensitive miniature pressure cell. Jour. Sci. Inst. 31: pp. 467-469 (1954).

50. Reece, A.R. and J.Y. Wong. Prediction of rigid wheel performance based on the analysis of soil-wheel stresses. Part I. Performance of driven rigid wheels. Journal Terramechanics 4 (1), pp. 81 (1967).

51. Richards, R. Jr. and R. Mark. Gelatin models for photoelastic analysis of gravity structures. Experimental Mechanics, pp. 30-38, (January 1966).

52. Roscoe, K.H., J.R.F. Arthur and R.G. James. The determination of strains in soils by an X-ray method. Civil Engineering and Public Works Rev. 58: pp. 873-876 and 1009-1012 (1963).

52a. Rowe, P.W. and Barden L. Importance of free ends in triaxial testing. Jr. of the Soil Mech. and Foundations Div. ASCE, Vol. 90, SM1, (January 1964).

53. Schwartzbart, H. and W.F. Brown, Jr. Notched bar tensile properties of various materials and their relation to the unnotch flow curve and notch sharpness. Trans. A.S.M., Vol. 46, pp. 998 (1954).

53a. Sciammarella, C.A. and A.J. Durelli. Moire fringes as a means of analyzing strains. Proceedings of A.S.C.E., Engineering Mechanics Div., Vol. 87, No. EM1, pp. 56-74 (1961).

54. Selig, E.T. and R.A. Wetzel. A miniature piezoelectric gauge for static and dynamic soil stress measurements. Contract Report No. 1-105 for U.S. Army Engineers Waterways Experiment Station (1964).

55. Siemens, J.C., J.A. Weber and T.H. Thornburn. Mechanics of soil as influenced by model tillage tools. Trans. of ASAE, Vol. 8, No. 1, pp. 1-7 (1965).

56. Schafer, R.L., C.W. Bockhop and W.G. Lovely. Model-prototype studies of tillage implements. Transactions of the ASAE, Vol. 11, No. 5, pp. 661-664 (1968).

57. Schafer, R.L., C.A. Reaves and D.F. Yong. An interpretation of distorsion in the similitude of certain soil-machine systems. Transactions of the ASAE, Vol. 12, No. 1, pp. 145-149 (1969).

58. Shichabalov, S.P. (Ed.) The method of polarized light for measurement of stresses (collection of papers presented in 1958 at the 1st Photoelastic Conf.). Pub. of the University of Leningrad, Section "Geological Problems", pp. 290-320 (1960) (in Russian).

59. Shipley, S.A., H.G. Leistner and R.E. Jones. Elastic wave propagation - A comparison between finite element prediction and exact solutions. Proceedings International Symposium on Wave Propagation and Dynamic Properties of Earth Materials, pp. 433-442, (1967).

60. Spinner, S. and W.E. Tefft. Method of determining mechanical resonance frequencies and for calculating elastic moduli from these frequencies. Proc. A.S.T.M., pp. 1221-1238 (1961).

61. Scott, R.F. Principles of soil mechanics. Addison-Wesley Publishing Company, Inc. (1963).

62. Tan, E. Stability of soil slopes. Proc. Am. Soc. Civil Engrs. (73) pp. 19-38 (1947).

63. Thomas, J.J. and C.J. Anderson. A method of showing soil movement. Journal of Agricultural Engineering Research 13 (2), pp. 196-200 (1968).

64. Toms, A.H. Soil mechanics in railway civil engineering. Engineering 180 (4677) pp. 384 (1955).

65, Vey E. and L.V. Strauss. Stress-strain relationships in clay due to propagation stress waves. Proceedings International Symposium on Wave Propagation and Dynamic Properties of Earth Materials, pp. 575-585 (1967).

66. Wilson, S.D. and R.J. Dietrich. Effect of consolidation pressure on elastic and strength properties of clay. Shear Strength Conference pp. 419-435 (1960).

67. Wu, T.H. Soil Mechanics. Allyn and Bacon Inc. pp. 212-220 (1966).

68. Yong, D.F. Similitude of soil-machine systems. Journal of Terramechanics, Vol. 3, No. 2, pp. 57-70 (1966).